Scholar Commons
USF University of South Florida

University of South Florida
Scholar Commons

Graduate Theses and Dissertations | Graduate School

2007

Barium Strontium Titanate films for tunable microwave and acoustic wave applications

Venkataramanan Gurumurthy
University of South Florida

Follow this and additional works at: http://scholarcommons.usf.edu/etd

 Part of the American Studies Commons

Scholar Commons Citation

Gurumurthy, Venkataramanan, "Barium Strontium Titanate films for tunable microwave and acoustic wave applications" (2007). *Graduate Theses and Dissertations.*
http://scholarcommons.usf.edu/etd/2196

This Thesis is brought to you for free and open access by the Graduate School at Scholar Commons. It has been accepted for inclusion in Graduate Theses and Dissertations by an authorized administrator of Scholar Commons. For more information, please contact scholarcommons@usf.edu.

Barium Strontium Titanate Films for Tunable Microwave and Acoustic Wave Applications

by

Venkataramanan Gurumurthy

A thesis submitted in partial fulfillment
of the requirements for the degree of
Master of Science in Electrical Engineering
Department of Electrical Engineering
College of Engineering
University of South Florida

Co-Major Professor: Ashok Kumar, Ph.D.
Co-Major Professor: Thomas Weller, Ph.D.
Jing Wang, Ph.D.
Priscila Delega Spagnol, Ph.D.

Date of Approval:
June 21, 2007

Keywords: bst, sputtering, nanocrystalline diamond, interdiffusion, dielectric permittivity, surface acoustic wave

© Copyright 2007, Venkataramanan Gurumurthy

ACKNOWLEDGEMENTS

I would like to foremost thank my co-major professor, Dr. Ashok Kumar, for his support, guidance and for providing me the opportunity to do research in a fascinating field. I would also like to express my sincere thanks to Dr. John Bumgarner and Mr. Larry Langebrake for their continued support during my research work at the Centre for Ocean Technology, College of Marine Science. I thank Dr. Thomas Weller, my co-major professor for his support and valuable suggestions. I would also like to thank my committee members, Dr. Jing Wang and Dr. Priscila Delega Spagnol for their time, guidance and valuable advice.

I wish to acknowledge all research scientists and staff members at the Centre for Ocean Technology, including Dr. Weidong Wang, Dr. Thomas Ketterl, Dr. David Edwards and Mr. Rajasekar Popuri for their help and support. My heartfelt thanks goes to Mr. Harish Jeedigunta, Mr. Praveen Kumar Shekhar and Mr. Sam Baylis who played a huge part in the success of this research work. A special thanks to Mr. Makoto Hirai for his help and suggestions. I enjoyed my two year stay at the Advanced Materials Research Laboratory where everybody shared a great camaraderie.

On the personal front I would like to thanks Mr. Sriram Chellappan, Mr. Bharath Natarajan and Mr. Balaji Rajan for being my friends, philosophers and guides. I dedicate this thesis to my parents, my teachers and God.

This work was supported by NSF ECS grant # 0601536 and NSF NIRT grant # ECS 0404137.

TABLE OF CONTENTS

LIST OF TABLES iii

LIST OF FIGURES iv

ABSTRACT viii

CHAPTER 1: INTRODUCTION 1
- 1.1 Overview 1
- 1.2 Thesis Outline 4

CHAPTER 2: THEORETICAL BACKGROUND 6
- 2.1 Piezoelectricity, Pyroelectricity and Ferroelectricity 6
- 2.2 General Properties of Ferroelectrics 7
  - 2.2.1 Crystal Structure 8
  - 2.2.2 Phase Transitions in Ferroelectric Materials 10
  - 2.2.3 Polarization and Dielectric Permittivity 15
  - 2.2.4 Mechanisms of Polarization 18
  - 2.2.5 Polarization and Frequency 21
- 2.3 Effect of Electric Fields on the Behavior of Ferroelectric Materials 23
- 2.4 Material Properties of Barium Strontium Titanate (BST) 28
  - 2.4.1 Crystal structure 29
  - 2.4.2 Phase transitions 30
  - 2.4.3 Polarization 35
  - 2.4.4 Microstructure and Point Defect Chemistry 37
- 2.5 BST Device Technology for Tunable Microwave Applications 39
- 2.6 Deposition Technologies for Barium Strontium Titanate Thin Films 41
- 2.7 Material Characterization in the High Frequency Regime 42

CHAPTER 3: VARACTOR PROCESSING 44
- 3.1 BST Based Metal Insulator Metal (MIM) Structure 44
- 3.2 RF Magnetron Sputtering 46
- 3.3 Deposition of BST Thin Films by RF Magnetron Sputtering 50
- 3.4 Deposition of Nanocrystalline Diamond (NCD) Films 55
- 3.5 Fabrication of BST Metal Insulator Metal Structures 59

CHAPTER 4: INTERDIFFUSION 63
4.1 Interdiffusion in Thin Films 63
4.2 Interdiffusion Effects in Pt/Ti/SiO_2/Si Structure 65
4.3 NCD/Pt/BST Structure 68

CHAPTER 5: VARACTOR MEASUREMENTS 73
5.1 Measurement Setup and Equivalent Circuit Model 73
5.2 Variation of Capacitance with Electric Field 75
5.3 Variation of Capacitance with Frequency 80
5.4 Varactor Breakdown and Tunability 85
5.5 Temperature Versus Capacitance Measurements 88

CHAPTER 6: SURFACE ACOUSTIC WAVE DEVICES 90
6.1 Surface Acoustic Wave (SAW) Devices 90
6.2 Types of SAW Devices 91
6.3 Basic SAW Device Performance Parameters 93
6.4 Challenges in Development of Layered SAW Devices 94
6.5 Design of SAW Bandpass Filters and Resonators 95
6.6 Deposition of BST on Chemical Vapor Deposited Diamond 98
6.7 Fabrication of Interdigital Structures 99
6.8 Curie Temperature Measurements on $Ba_{0.8}Sr_{0.2}TiO_3$ 101

CHAPTER 7: CONCLUSIONS AND FUTURE WORK 105
7.1 BST Deposition and Structural Characterization 105
7.2 Interdiffusion 106
7.3 BST Varactor Fabrication and Measurements 106
7.4 Diamond Based Layered SAW Devices 109

REFERENCES 110

LIST OF TABLES

Table 2.1: Types of perovskite oxides [24]. 9

Table 2.2: Different deposition methods and their advantages and disadvantages [53]. 41

Table 3.1: The deposition conditions used for sputtering BST thin films in [91]. 51

Table 3.2: The optimized deposition conditions used for sputtering BST thin films . 52

Table 3.3: Deposition parameters for NCD films. 56

Table 5.1: Performance summary of varactors fabricated on SiO_2. 87

Table 6.1: Comparison of acoustic velocities of prospective materials [28, 106, 107]. 93

Table 6.2: Variations of various parameters in SAW device geometry. 96

Table 6.3: Variation in thickness of BST layer with different deposition times. 103

LIST OF FIGURES

Figure 1.1: Interdiffusion issues in Pt/Ti/SiO_2/Si wafer at high temperatures in the presence of oxygen. 3

Figure 2.1: Perovskite ABO_3 structure with the A and B cations on the corner and body center positions, respectively [21]. 9

Figure 2.2: Phase transitions and corresponding changes in crystal structure of perovskite ferroelectric materials [32, 38]. 10

Figure 2.3: PFM images of epitaxial PZT film [40]. 12

Figure 2.4: The typical hysterisis loop for a ferroelectric material [32]. 13

Figure 2.5: Dipole behavior during the poling process [19]. 13

Figure 2.6: Polarization mechanisms [47]. 20

Figure 2.7: Variation of total polarizability of a dielectric material with frequency [41]. 22

Figure 2.8: Frequency dependence of real part of relative dielectric permittivity [40]. 22

Figure 2.9: Variation of permittivity with applied bias for a ferroelectric material in (a) Ferroelectric phase (b) Paraelectric phase [40]. 24

Figure 2.10: Variation of capacitance of $Ba_{0.5}Sr_{0.5}TiO_3$ thin films with frequency for 1V increments in bias [56]. 26

Figure 2.11: Bias-induced resonant dips observed in BST based MIM capacitor from 0-20V in 5V increments [56]. 27

Figure 2.12: Prospective areas of application of barium strontium titanate. 28

Figure 2.13: The perovskite crystal structure of BST in cubic phase with no externally applied electric field [53]. 29

Figure 2.14: Variation of Curie temperature and lattice parameters of BST with Barium percentage composition [64]. 30

Figure 2.15: Variation of dielectric constant of BST for different concentrations of barium and strontium [66]. 31

Figure 2.16: Phase transition behavior of $Ba_{0.7}Sr_{0.3}TiO_3$ [68]. 33

Figure 2.17: P-E hysterisis loops for $Ba_xSr_{1x}TiO_3$ thin films at room temperature[71]. 34

Figure 2.18: Thickness dependence of relaxation currents observed in metal organic chemical vapor deposited BST thin films [59]. 36

Figure 2.19: X-ray diffraction spectrum of sintered BST target. 37

Figure 2.20: Reduction in device packages using BST capacitors [15]. 39

Figure 2.21: Two different configurations of BST varactors [91]. 40

Figure 2.22: Coplanar waveguide configuration [92]. 43

Figure 3.1: Material issues to be considered in BST based MIM structure [15]. 44

Figure 3.2: Schematic of stacked BST Metal Insulator Metal structures. 45

Figure 3.3: Process initiated by bombardment of ions onto the sputtering target [94]. 47

Figure 3.4: Description of the sputtering process. 48

Figure 3.5: The CMS-18 sputtering system at the AMRL. 49

Figure 3.6: Characteristic X-ray diffraction pattern of BST thin films deposited on platinum thin film. 53

Figure 3.7: Charactersitic microstructure of BST films deposited on platinum thin film. 54

Figure 3.8: Dielectric strength versus dielectric constant for dielectrics [56]. 54

Figure 3.9: The *Cyrannus 1 I plas* system used for deposition of NCD films. 55

Figure 3.10: Comparison of X-ray diffraction paterns and surface roughness for BST films deposited on (a) platinized silicon and (b) platinized NCD. 57

Figure 3.11: Comparison of microstructure and surface roughness for BST films deposited on (a) platinized silicon and (b) platinized NCD. 58

Figure 3.12: Mask pattern and active device areas used for fabrication of BST MIM structures. 61

Figure 3.13: (a) Fabrication process flow of BST MIM structure. (b) Schematic of the top view of the device and photograph of a fabricated device. 61

Figure 3.14: Cross-sectional vie of the SiO_2 and NCD based MIM structures in CPW configuration (not to scale). 62

Figure 4.1: Model showing electromigration related mass-transport arising due to non-uniform grain structure and temperature gradients [27]. 64

Figure 4.2: Silicon dioxide, tianium and platinum layers on Si(100) wafer. 65

Figure 4.3: Interdiffusion between the platinum and titanium layers after BST deposition. 67

Figure 4.4: Nanocrystalline diamond, platinum and BST layers on Si(100) wafer. 69

Figure 4.5: Area of the sample used for X-ray mapping. 69

Figure 4.6: Silicon X-ray map. 70

Figure 4.7: NCD X-ray map. 70

Figure 4.8: Platinum X-ray map. 71

Figure 4.9: Titanium X-ray map. 71

Figure 4.10: Variation of resistance with frequency for platinum film on NCD and SiO_2 diffusion barrier layers. 72

Figure 5.1: Equivalent circuit model used to characterize varactor performance [23]. 73

Figure 5.2: Capacitance-voltage behavior of varactor fabricated on SiO_2. 75

Figure 5.3: Dielectric relaxation behavior of BST films. 76

Figure 5.4: Variation of permittivity with applied bias for varactors fabricated on SiO_2 and NCD films. 77

Figure 5.5: Response of NCD varactor (a) before and (b) after drive-in voltage. 78

Figure 5.6: Variation of quality factors with applied bias for varactors fabricated on SiO_2 and NCD films. 78

Figure 5.7: Variation of R_s with applied bias for varactors fabricated on SiO_2 and NCD films. 79

Figure 5.8: Variation of capacitance with frequency for (a) SiO_2 varactor and (b) NCD varactor at different bias voltages. 80

Figure 5.9: Variation of quality factor, loss tangent and R_s with fequency. 82

Figure 5.10: The increase in the depth of resonant curves with applied bias for SiO_2 and NCD varactors. 83

Figure 5.11: The variation of depths of resonant curves with device active area for SiO_2 and NCD varactors. 84

Figure 5.12: Photograph of Device#4 after breakdown. 86

Figure 5.13: Forward bias CV curve of varactor fabricated on SiO_2 with a BST thickness of 150 nm. 86

Figure 5.14: Variation of capacitance with temperature for measured varactor at 100 MHz. 89

Figure 6.1: Schematic of (a) surface acoustic wave propagation on a piezoelectric surface, (b) a basic SAW device [105]. 90

Figure 6.2: Typical SAW bandpass filter response [105]. 92

Figure 6.3: General schematic of SAW bandpass filter and resonator [108]. 92

Figure 6.4: Relation between SAW wavelength and period of interdigital transducer. 95

Figure 6.5: Layout of different device structures. 97

Figure 6.6: Cross-sectional image of BST on CVD diamond. 98

Figure 6.7: Photograph of fabricated IDT's with 2 μm and 3 μm finger widths . 99

Figure 6.8: Fabrication process flow of Interdigital structures. 100

Figure 6.9: Schematic of Interdigital capacitor structure used for Curie temperature measurements. 102

Figure 6.10: Schematic of appearance of the 4-inch sample after deposition of BST for 12 hours with different colors representing different thicknesses. 102

Figure 6.11: Equivalent circuit diagram used for characterizing IDC performance. 103

Figure 6.12: Temperature versus capacitance measurements obtained from the measured Interdigital capacitor. 104

Figure 7.1: FIB milled BST series gap capacitor configuration. 108

BARIUM STRONTIUM TITANATE FILMS FOR TUNABLE MICROWAVE AND ACOUSTIC WAVE APPLICATIONS

Venkataramanan Gurumurthy

ABSTRACT

The composition-dependent Curie temperature and bias-dependant dielectric permittivity of Barium Strontium Titanate (BST) makes it very attractive for tunable application in the RF/Microwave regime . In this research work, the performance of BST varactors fabricated on the conventional Pt/Ti/SiO_2/Si bottom electrode stack were compared with those fabricated using chemical vapor deposited Nanocrystalline Diamond (NCD) as the diffusion barrier layer instead of SiO_2. The varactors fabricated on NCD films displayed much better symmetry in capacitance-voltage behavior and better overall quality factors than varactors fabricated on SiO_2. The improvement in performance can be attributed to existence of stable interfaces in the devices fabricated on NCD which reduced the bottom electrode losses at high frequencies. The SiO_2 based BST varactors on the other hand displayed better reliability and breakdown fields. The main purpose of this research work is to develop a robust Metal Insulator Metal (MIM) structure to achieve better all round performance of BST varactors.

In the second part of this research work, the prospect of developing diamond based layered Surface Acoustic Wave (SAW) devices using $Ba_{0.8}Sr_{0.2}TiO_3$ as the piezoelectric layer is investigated.

Structural characterization of BST thin films deposited on Si/NCD/Pt and $Si/SiO_2/Ti/Pt$ stack were performed using X-Ray Diffraction (XRD) and Atomic Force Microscopy (AFM). Cross-sectional studies on the two stacks were performed using Scanning Electron Microscopy (SEM). X-Ray Mapping (XRM) was then done to ascertain the quality of the interfaces and to check for interdiffusion between layers.

MIM structures in the Coplanar Waveguide (CPW) configuration were fabricated using conventional lithography and etching techniques for high frequency measurements. The performance of the fabricated varactors was characterized from 100 MHz to 1 GHz.

For the SAW application, structural characterization of $Ba_{0.8}Sr_{0.2}TiO_3$ on Chemical Vapor Deposited (CVD) diamond was done and the deposition procedure was optimized to obtain thick BST films. SAW bandpass filters and resonators were designed wherein the device geometry was varied over a wide range in order to characterize the variation in device performance with geometry. Finally interdigital capacitor structures were fabricated and used for conducting Curie temperature measurements on the deposited BST films in order to determine the operation range of the deposited BST films.

CHAPTER 1:

INTRODUCTION

1.1 Overview

Modern communication systems require tunable circuits like filters, matching networks and phase shifters in analog RF front ends for gaining adaptability to changes in operating conditions like frequency, impedance and RF drive level. Tunable circuits also offer a tool to counter the stringent frequency and power requirements of the wireless communication industry. In order to realize the tuning circuits for the current and next generation communication systems, components which offer high performance and generate low losses are required; this underlines the necessity for exploring new materials, designs and technologies for meeting these requirements. A special class of high-permittivity ferroelectric materials, whose permittivity is field-dependent, offers a great promise for applications in the tunable RF/Microwave regime. The main driving force for an increased interest in these materials is the potential for substantial miniaturization and the possibility of integration with conventional microelectronic circuits [1-4].

The properties of ferroelectric materials are thickness-dependant and generally ferroelectric thin films are used for microwave applications because they display negligible temperature dependence or phase transition effects. Additionally, thin films display better tunability as higher fields can be better sustained in comparison to bulk films [5-7].

Barium Strontium Titanate (BST) is one of the most researched ferroelectric materials for tunable applications at high frequencies as it demonstrates a superior tradeoff between loss and tunability. BST based varactors have also been shown to display high power-handling capability and very high breakdown fields (>2 MV/cm) [8-14].

BST thin films generally attain crystalline phase when deposited at temperatures around 450ºC-700 ºC in an oxygen environment. Therefore, for Metal-Insulator-Metal (MIM) capacitor applications, the bottom electrode layer should have good thermal stability and oxidation resistance [15].

Platinum (Pt) is primarily chosen as the standard electrode material mainly because of its chemical inertness in a high temperature oxidizing ambient. It has been reported that better quality of platinum bottom electrode translates into better overall device performance. Typically, a silicon dioxide (SiO_2) diffusion barrier layer is grown on silicon substrate before depositing Pt to prevent diffusion of platinum through the substrate[15, 16].

The SiO_2 layer gets decomposed due to diffusion of Pt into the Si/SiO_2 interface which leads to the formation of volatile SiO [17]. Titanium (Ti) layer is sputtered to act as an adhesion layer between platinum and SiO_2 and to prevent the decomposition of the SiO_2 layer. However when depositions are done in an oxygen ambient at high temperatures it was observed that there was inter-diffusion between the elemental titanium and platinum. This inter-diffusion phenomenon leads to defect formation in the platinum layer which results in degradation of device performance, depending upon the thickness of the adhesion layer [18-22]. Ali Tombak et al. have reported that above 300 MHz electrode losses play a principal role in degrading the quality factor of BST thin film capacitors [23].

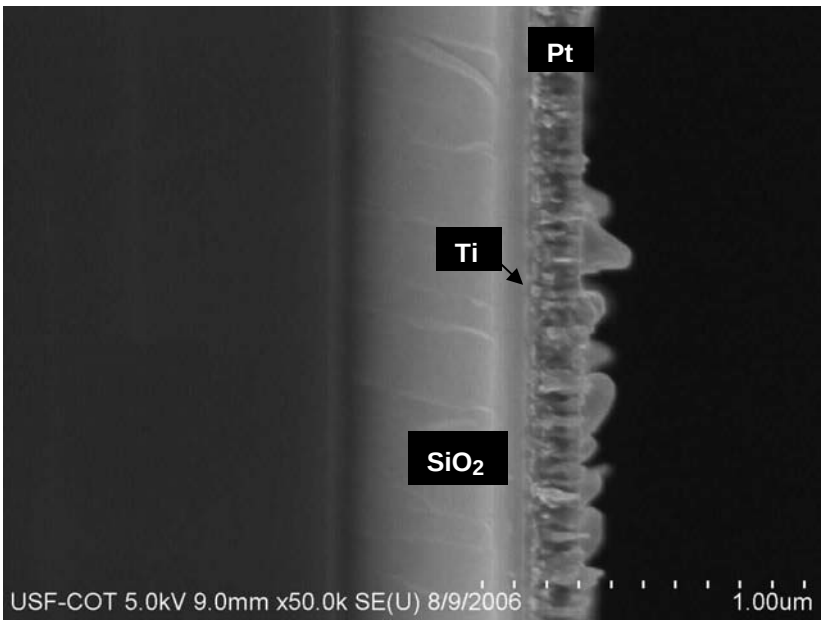

Figure 1.1: Interdiffusion issues in Pt/Ti/SiO_2/Si wafer at high temperatures in the presence of oxygen.

Therefore it is very important to obtain a stable defect free bottom electrode stack to achieve superior device performance. Figure 1.1 is an Scanning Electron Microscope (SEM) image depicting the interdiffusion between the Ti and Pt layers and the hillocking in the Pt layer after the Pt/Ti/SiO_2/Si wafer was heated at 600ºC in the presence of oxygen for four hours (BST's deposition condition).

Nanocrystalline Diamond (NCD) deposited by Microwave Plasma Enhanced Chemical Vapor Deposition (MPECVD) method would make an excellent material for high frequency applications [24] . Prior research work has shown that diamond films deposited on high-resistive silicon substrate displayed very low RF losses comparable with the performance of thermally grown SiO_2 on high-resistive silicon substrate from DC-65GHz [25].Very stable electrodes can be obtained by depositing metals on diamond films as they are chemically inert and highly corrosion resistant [26]. Diamond also has the highest thermal conductivity among all materials which means that it can act as an effective heat sink that can reduce the

detrimental effects that the electromigration phenomenon has on the metal layers [27]. Thus CVD diamond exhibits excellent properties for application as a stable diffusion barrier layer for ferroelectric thin film-based MIM devices for high frequency applications.

In this research work we have shown that varactors with better performance can be obtained by using nanocrystalline diamond films as the diffusion barrier layer. The processing steps are kept the same as those for devices on silicon and the improved performance of the varactors rely solely on the NCD films. Thus the process steps remain standardized and reliable.

Application of diamond to surface acoustic wave (SAW) devices is attractive because it has the highest acoustic velocity among all materials, and thus, when combined with a piezoelectric layer, it will be ideal for high frequency SAW devices providing great advantages in device fabrication. For instance, a 2.5 GHz SAW filter can be fabricated with 1 μm line-and-space electrodes with the piezoelectric material on diamond structure, whereas sub half micron electrodes are necessary for conventional SAW materials [28].

The second part of the research work involves investigating the performance of layered Surface Acoustic Wave (SAW) structures based on CVD diamond. In this research work $Ba_{0.8}Sr_{0.2}TiO_3$ is investigated as the piezoelectric layer for the proposed layered SAW devices.

1.2 Thesis Outline

In chapter 2 the general properties of ferroelectric ceramics like crystal structure, phase transitions and polarization mechanisms are discussed. Then the material properties of BST and the factors that affect the properties of BST thin films are discussed. Finally the common device technologies adopted for BST varactors are discussed.

Chapter 3 summarizes the previous work done in structural and dielectric characterization of BST thin films using RF magnetron sputtering. Further deposition optimization details are given along with the structural characterization information. The structural properties and the surface morphology of BST thin films deposited on Pt/Ti/SiO_2/Si and Pt/NCD/Si are compared next. Finally the processing details are provided for the fabrication of varactors in Coplanar Waveguide (CPW) configuration.

In chapter 4 a basic introduction to the various mass transport and interdiffusion mechanisms operating in thin films are given. Cross-sectional SEM analysis of the Pt/Ti/SiO_2/Si and Pt/NCD/Si stacks is done to study the quality of the interfaces after BST deposition. Additionally X-Ray Mapping (XRM) is performed to check for interdiffusion between different layers in the BST/Pt/NCD/Si stack.

In chapter 5 the electrical performance of the varactors fabricated on NCD and SiO_2 is compared. S-parameter measurements are conducted and equivalent circuit modeling of varactor behavior is done using ADS2004A. Based on the analysis the quality factor, tanδ, tunability and breakdown strengths of the varactors are compared and a final analysis of how a stable bottom electrode and well-defined interfaces affect the performance range of the varactor is discussed. Variation of capacitance with temperature for the deposited BST films is also plotted to check for ferroelectric domains in the film.

In Chapter 6 a brief discussion on Surface Acoustic Wave (SAW) propagation, properties and performance parameters is provided. Then development details of a mask for layered SAW devices based on diamond are provided. Later the deposition of $Ba_{0.8}Sr_{0.2}TiO_3$ on CVD diamond is by RF magnetron sputtering is discussed. Details about Curie temperature measurements done on deposited BST films are then provided.

CHAPTER 2:

THEORETICAL BACKGROUND

2.1 Piezoelectricity, Pyroelectricity and Ferroelectricity

In certain crystalline minerals, the crystals become electrically polarized when subjected to mechanical forces. Tension and compression generate voltages of opposite polarity, which is proportional to the applied force. Conversely, if the crystals were exposed to an electric field, it lengthens and shortens according to the polarity of the field, and is proportional to the strength of the field. These behaviors are labeled the piezoelectric and inverse piezoelectric effect respectively. For the piezoelectric effect to occur, the absence of centre of symmetry or inversion point is necessary. All crystalline materials are conventionally classified into 32 crystal classes of which 21 lack centre of symmetry of which 20 can show piezoelectricity. This group of twenty comprises of a subgroup of 10 crystal classes which contain a unique polar axis. As a result, the crystals of this subgroup when uniformly heated generate an additional electric charge, due to spontaneous polarization parallel to the polar axis-in addition to piezoelectric effect related charge creation. This effect is known as pyroelectricity. In some pyroelectric crystals, an additional property is observed wherein, an external electric field can reverse the spontaneous polarization of the crystals over some temperature range. The response of polarization to an external electric field manifests itself as a hysterisis loop. The materials which exhibit this property are called ferroelectrics. All ferroelectrics are pyrolectric and piezoelectric [29-31].

2.2 General Properties of Ferroelectrics

Ferroelectricity is a phenomenon which was discovered in 1921. Rochelle salt was the first material found to show ferroelectric properties. A huge leap in the research on ferroelectric materials came in the 1950's, with the introduction of metal oxide-based piezoelectric ceramics and other man-made materials. These materials generally are physically strong and chemically inert. The composition, shape and dimensions of a ceramic material can be tailored to meet the requirements of a specific application [32]. The widespread use of ferroelectric ceramics started with the use of barium titanate ($BaTiO_3$) based ceramics in capacitor applications and piezoelectric transducer devices. Since then, many other ferroelectric ceramics including lead titanate ($PbTiO_3$), lead zirconate titanate (PZT), lead lanthanum zirconium titanate (PLZT), and relaxor ferroelectrics like lead magnesium niobate (PMN) have been developed and utilized for a variety of applications. In the past 20 years, due to the development of ceramic processing and thin film technology, many new applications have emerged. The biggest use of ferroelectric ceramics have been in the areas such as dielectric ceramics for capacitor applications, ferroelectric thin films for non volatile memories, piezoelectric materials for medical ultrasound imaging and actuators, and electro-optic materials for data storage and displays [33].

In this section, the crystal structure, phase transition behavior and polarization phenomenon of ferroelectric ceramics will be discussed as they play a very important part in determining the properties of ferroelectric ceramics irrespective of area of application, chemical composition or thickness of films used.

2.2.1 Crystal Structure

A ferroelectric ceramic is an arrangement of perovskite (oxide having the same crystalline structure as the mineral, $CaTiO_3$) crystals, each consisting of tetravalent metal ions (usually titanium or zirconium), in a lattice of large divalent metal ions (usually lead or barium), and usually O^{2-} ions. The resulting crystal structure is in general called the perovskite ABO_3 structure is shown in Figure 2.1, where A represents the large cations located at the corners of the unit cell, B represents the smaller cations located at the body center and O is usually the oxygen atoms positioned at the face centers though halides like fluorine and chlorine can also take its place. An ideal cubic perovskite structure is not very common and symmetry is reduced in most perovskite materials due to distortions. A deformed perovskite structure where the positively charged metal ions are displaced with respect to the negatively charged oxygen (or halide) ions leads to the formation of a polar axis in the direction of the deformation. The formation of this polar axis gives rise to spontaneous polarization- one of the defining aspects of a ferroelectric material.

The perovskite structures are chemically very flexible i.e. many different cations can be substituted with transition metal ions on both the A and B sites without drastically changing the overall structure. Complete solid solutions are easily formed between many cations, often across the entire range of composition. Even though two cations are compatible in solution, their behavior can be radically different when apart from each other. The interactions of the transition metal ions with the oxygen or halide ions are complex. Therefore, the properties of the final structures are completely different from one another depending upon the metal ion that has been used for substitution.

Thus the composition, shape and dimensions of perovskite structures and hence their electronic properties can be tailored over a wide range. This is a major reason of application of perovskite ferroelectric ceramics over a broad spectrum of applications [32]. Table 2.1 summarizes the different types of perovskite oxide structures [34].

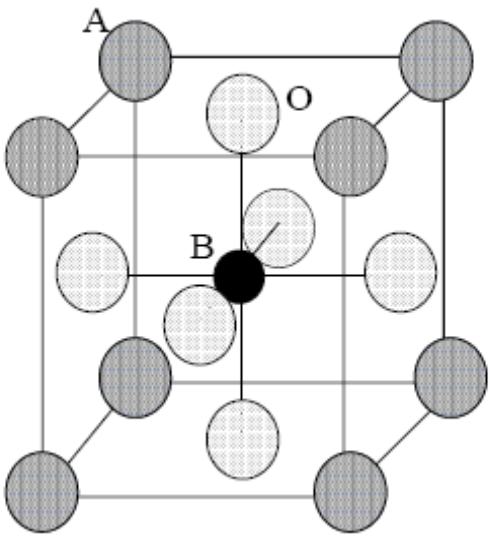

Figure 2.1: Perovskite ABO_3 structure with the A and B cations on the corner and body center positions, respectively. Three oxygen anions per unit cell occupy the faces and form octahedra surrounding the B-site [21].

Table 2.1: Types of perovskite oxides [24].

Group	Oxide Type	Examples
I	$A^{1+}B^{5+}O_3$	$NaNbO_3$, $KTaO_3$, $NaTaO_3$
II	$A^{2+}B^{4+}O_3$	$BaTiO_3$, $PbTiO_3$, $SrTiO_3$,
III	$A^{3+}B^{3+}O_3$	$YCrO_3$, $LaAlO_3$, $YAlO_3$

2.2.2 Phase Transitions in Ferroelectric Materials

In general, ferroelectric materials undergo a transformation from a paraelectric phase to a ferroelectric phase when cooled down to a certain temperature known as the Curie temperature (*Tc*). The phase transition behavior of ferroelectrics is theoretically modeled using the Landau-Ginzburg-Devonshire (LGD) theory [35-37]. The schematic of ferroelectric phase transition and the change in crystal structure below and above Curie temperature is represented in Figure 2.2[32, 38].

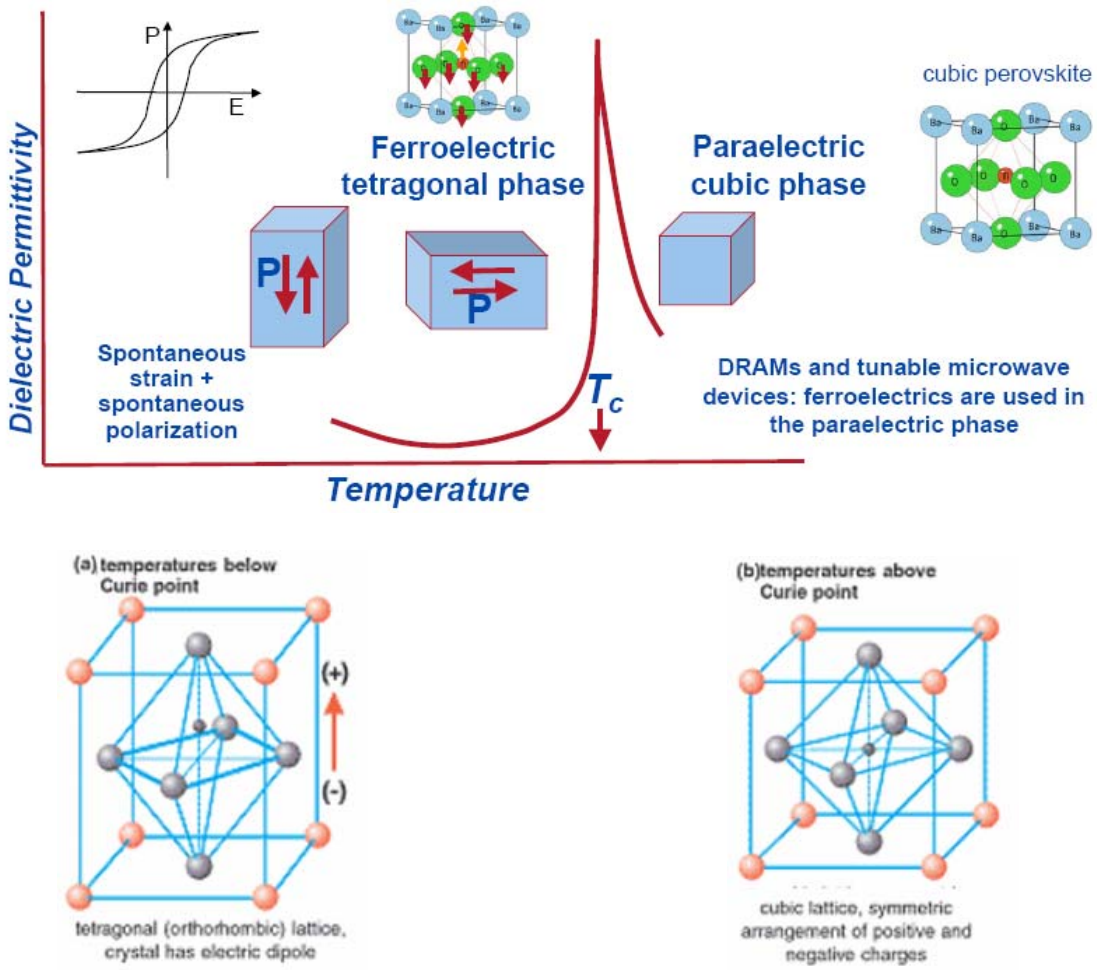

Figure 2.2: Phase transitions and corresponding changes in crystal structure of perovskite ferroelectric materials [32, 38].

As depicted in Figure 2.2, in the ferroelectric phase, the dielectric constant increases as the temperature increases. While in the paraelectric phase, the dielectric constant decreases with increase in temperature obeying the Curie-Weiss law [39]. The Curie-Weiss law is given as follows:

$$\varepsilon_r = \frac{C}{(T - To)} \tag{2.1}$$

, where ε_r is the dielectric permittivity, T_o is the Curie-Weiss temperature ($To \leq Tc$), T is temperature at which ε_r is being measured and C is the Curie constant.

Phase transitions in perovskite ferroelectric crystals is associated with a change in crystal structure from a centro-symmetric non-polar lattice (paraelectric phase) to non centro-symmetric polar lattice (ferroelectric phase). Below the Curie temperature, the position of smaller tetravalent metal ion and the octahedral structure changes from cubic to tetragonal symmetry, with the smaller tetravalent metal ion in an off-center position corresponding to a permanent dipole. In the ferroelectric phase, adjoining dipoles align themselves in a particular direction forming regions of local alignment called domains. The alignment gives a net dipole moment to the domain and thus a net polarization called as spontaneous polarization (P_s). Domains are formed due to stray electric fields which are created by non-compensated polarization charges. However the direction of polarization in the neighboring domains is not the same; hence the ferroelectric material displays no overall polarization unless an electric field is applied to it. The domains are separated by domain walls and a particular domain pattern is a result of stresses created at the Curie point, uncompensated surface charges and physical imperfections (vacancies, dislocations and dopants). 3-D Piezoresponse Force Microscope (PFM) is used to visualize domains in thin films.

Piezoresponse images of epitaxial Lead Zirconium Titanate (PZT) film is shown in Figure: 2.3 [40].

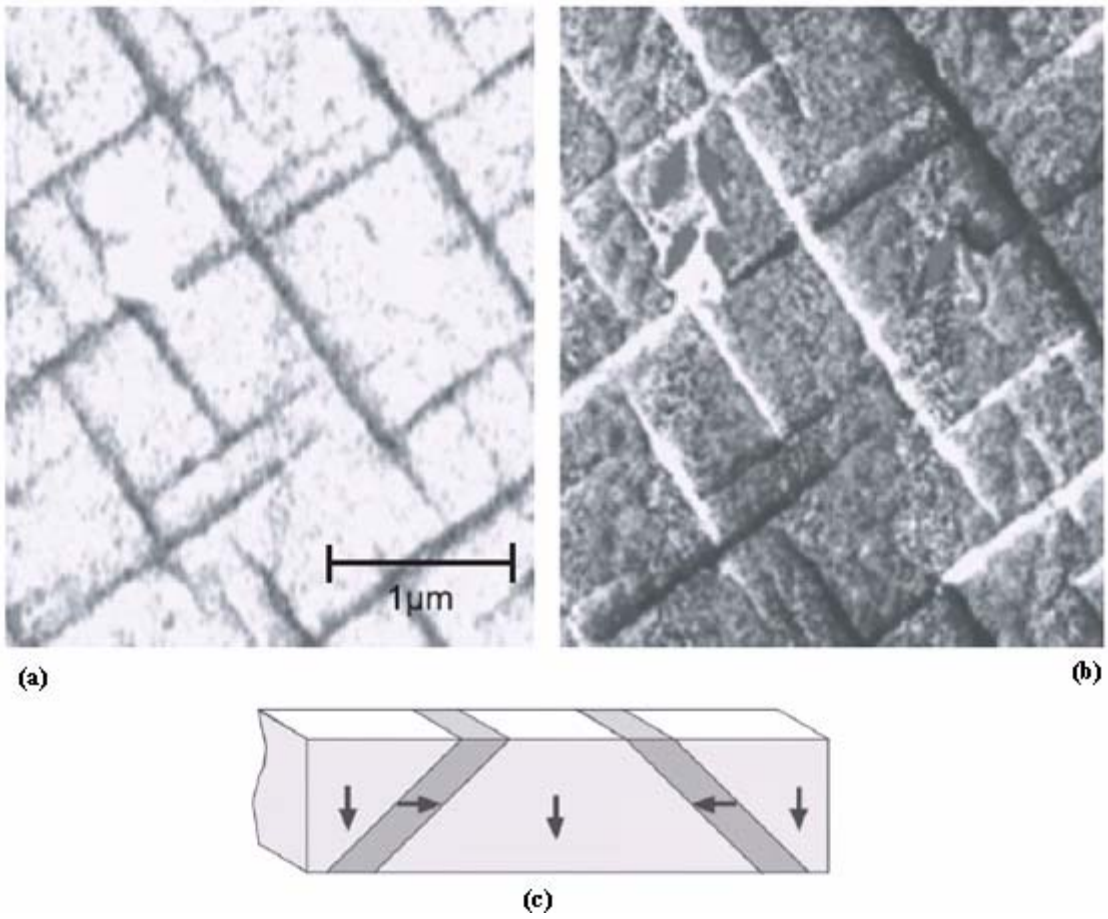

Figure 2.3: PFM images of epitaxial PZT film. (a) Shows domains with vertical (out-of-plane) polarization, (b) shows domains with horizontal (in-plane) polarization and (c) is a schematic showing the different directions of orientation of dipoles in different domains [40].

Ferroelectric materials display hysterisis below Curie temperature with an applied field. The process of applying an electric field to a ferroelectric material in order to polarize it is called poling. When the electric field is increased from zero, the polarization also increases due to alignment of more and more dipoles in the same direction. When all the dipoles are aligned in the same direction, maximum polarization value is reached and the material attains saturated state. If the applied electric field is decreased from saturation point, the

polarization also decreases but it does become zero when electric field is zero due to remnant polarization (P_r). When the electric field is reversed, the polarization value becomes zero when the field reaches a certain value called the coercive field. When the field is decreased further, the material reaches a reverse saturation point and from there onwards the sequence repeats itself. The typical hysterisis loop for a ferroelectric material is shown in Figure 2.4 [32]. A theoretical representation of polarization mechanism of the dipoles in a ferroelectric material is depicted in Figure 2.5 [32].

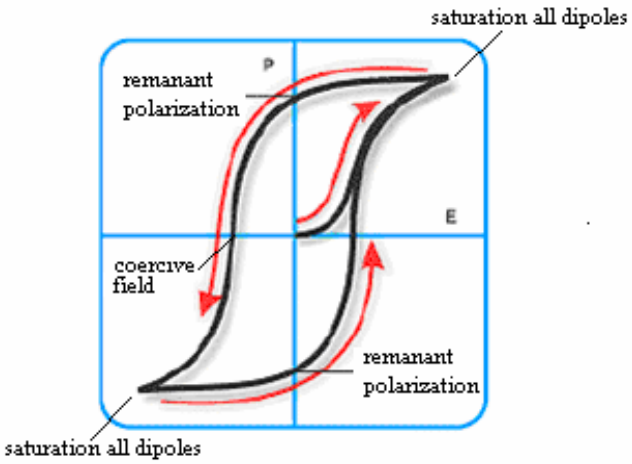

Figure 2.4: The typical hysterisis loop for a ferroelectric material [32].

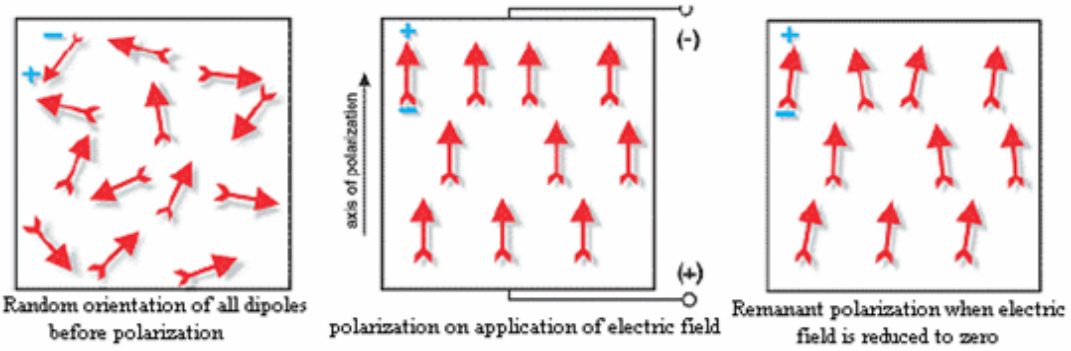

Figure 2.5: Dipole behavior during the poling process [19].

The hysterisis behavior of ferroelectrics is believed to originate from irreversible polarization processes occurring in a ferroelectric lattice. The exact relationship between

these processes and the domain walls and defects is not known. Hence it has not been possible to explain the overall appearance of the hysterisis curves for different ferroelectric materials [40].

The transition from ferroelectric phase to paraelectric phase is classified into first- order phase transition and second-order phase transition where the order parameter is polarization. In a first-order phase transition the polarization is discontinuous with temperature. First-order phase transition occurs in Barium Titanate ($BaTiO_3$). In second-order phase transition the polarization is continuous with temperature (e.g. Lithium Tantalate)[41].

It is also important to note that in most ABO_3 perovskites have different stable phases at different temperatures. Barium titanate has 4 stable phases which in the order of transformation are tetragonal, orthorhombic, rhombhoehedral and cubic phases respectively. On the other hand, lead titanate has only two phases-tetragonal and cubic[42, 43].

Above the Curie temperature, thermal energy or an electric field is sufficient to induce movement of the metal atoms randomly from one position to another and so there is no fixed asymmetry. The open octahedral site allows the tetravalent metal atom to develop a large induced dipole moment when an electric field is applied; which is the main reason why perovskite ferroelectric materials have high permittivity in the paraelectric phase.

In the ferroelectric phase, the strong hysterisis behavior observed makes the ferroelectric material suitable for non-volatile memory applications and piezoelectric applications. Above the Curie temperature (in the paraelectric phase); the material no longer has spontaneous polarization. However the dielectric permittivity still remains high and hence the ferroelectric material is highly suitable for DRAM and tunable microwave applications.

2.2.3 Polarization and Dielectric Permittivity

Polarization is the central quantity that is used to explain the physics and behavior of dielectric material (a ferroelectric material both in the paraelectric and ferroelectric phase in considered to be a dielectric). The following discussion adapted from [40, 41] provides both the macroscopic and microscopic view of the origin of polarization.

A dipole is a system consisting of a positive and negative charge separated by a distance *'a'*. If 'r_i' is the position vector of charge *'q_i'* then the dipole moment *'p'* is

$$p = q \cdot a \tag{2.2}$$

The dipole moment for a system of charges is given by

$$p = \sum_i q_i r_i \tag{2.3}$$

Polarization *'P'* is defined as dipole moment per unit volume.

The polarization of a dielectric is due to the redistribution of charges inside the dielectric when an electric field is applied to it. From a macroscopic point of view the dielectric has no net charges if no electric field is applied to it. This is because the dielectric has as such equal number of positive and negative charges in a macroscopic volume and hence the net charge is zero.

If one considers a boundary perpendicular to the direction of polarization, there is a net positive or negative charge on the surface which is not compensated by the charges inherent to the dielectric. Therefore the polarization appears on the surface of the dielectric. Thus polarization of a dielectric produces a macroscopic electric field which is determined by these surface charges.

If ‘E’ is the total electric field across the dielectric and E_0 is the applied field and E_1 is the field due to polarization of the solid, then

$$E = E_0 + E_1 \tag{2.4}$$

The field E_1 opposes the applied field E_0 and it is called the depolarizing field. The depolarizing field tries to break down the ferroelectric particles into domains. Electric fields whose values range from 200V/mm -500V/mm or greater have a significant depolarizing effect but the degree of depolarization also depends on the grade of the material, the exposure time, temperature etc. [32, 44].

The relationship between polarization and the total electric field on the dielectric can be expressed in terms of dielectric susceptibility (χ) which is a tensor and depends on the electric field.

$$P = \chi \cdot E \tag{2.5}$$

Assuming that the volume that is being considered is a thin slab, it can be shown that uniform polarization produces uniform depolarization field inside the dielectric. The depolarization factor ‘N’ is determined by the axes of the thin slab of dielectric. The field due to polarization can be expressed as,

$$E_1 = N \cdot P \tag{2.6}$$

Combining equations (2.5) and (2.6), polarization can be expressed in terms of ‘N’ as,

$$P = \left(\frac{\chi}{1 + N\chi} \right) \cdot E_0 \tag{2.7}$$

Looking at polarization from a microscopic point of view, E_{loc} is the local electric field acting on a particular atom and therefore can be affected by the nearest surrounding atoms. Therefore E_{loc} would provide an insight into the microscopic properties of the material.

Since the polarization of the medium is produced by the field, the polarizability 'α' of the atom can be defined in terms of the local electric field at the atom.

$$p = \alpha \cdot E_{loc} \tag{2.8}$$

In condensed matter, the density and interaction between the dipoles will be quite high. Hence E_{loc} at the position of a particular dipole is given by the superposition of the applied macroscopic field 'E' and sum of all other dipole fields. For cubic structures (perovskite crystal structure in paraelectric phase), a relation is obtained between 'α' and the macroscopic permittivity ε (=ε_0. ε_r),

$$\varepsilon = \frac{\varepsilon_0 + 2q_i \cdot \alpha_j}{\varepsilon_0 - q_i \cdot \alpha_j} \tag{2.9}$$

Equation (2.9) is called the Clausius-Mosotti equation [45]. The equation can be applied only for crystal structures.

The total dielectric displacement 'D' on application of an electric field 'E' is the sum of the displacement due to the electric field in vacuum and due to the net polarization 'P' experienced in the material.

$$D = \varepsilon_0 E + P \tag{2.10}$$

The net polarization can be written in terms of susceptibility 'χ' as,

$$P = \varepsilon_0 \cdot \chi \cdot E \tag{2.11}$$

Combining equations (2.10) and (2.11) and using the relation $\varepsilon_r = 1+\chi$ which is a direct relation between relative permittivity 'ε_r' and 'D' is obtained.

$$D = \varepsilon_0 \cdot \varepsilon_r \cdot E \tag{2.12}$$

Thus, relative permittivity (ε_r) is a direct measure of the polarizability of the material and governs both phase variations and attenuation of the imposed field in the material [46].

2.2.4 Mechanisms of Polarization

Molecules, the basic building blocks of matter are composed of both positive (nuclei) and negative (electrons) charges. When an external electric field is applied the positive and negative charges are pulled apart i.e. the molecule gets polarized. Thus polarizability as a physical process can be attributed to the general structure of a molecule. There are different types of polarization contributing to dielectric response depending upon the structure of molecules constituting a particular material [40, 41, 46, 47]

- Electronic Polarization

It exists in all dielectrics and is caused by the displacement of the negatively charged electrons from the positively charged nucleus due to externally applied electric field.

- Ionic Polarization

It is due to the stretching of ionic bonds in molecules of ionic crystals caused by the displacement of ions. The change in the length of the ionic bonds induces a dipole moment.

- Dipolar or Molecular Polarization

Dipolar materials have a permanent moment i.e. moment even in the absence of an external electric field. However the net polarization of a dipolar material in the absence of an electric field is zero because the molecular moments are randomly oriented, resulting in a complete cancellation of the polarization. Piezoelectric materials exhibit dipolar polarization.

- Space Charge or Interfacial or Maxwell-Wagner Polarization

Exists in heterogeneous dielectric materials like BST where the charge carriers are accelerated by an applied field until they are impeded by and pile up at physical barriers. This build up of charge dictates the polarization of the material. Electrically conducting grains, insulating grain boundaries and interfaces are common barriers.

- Orientation Polarization

It describes the alignment of permanent dipoles in a material. "At ambient temperatures, usually all dipole moments have statistical distribution of their directions. An electric field generates a preferred direction for the dipoles, while the thermal movement of the atoms perturbs the alignment" [30].

- Domain Wall Polarization

It plays a decisive role in contributing to the dielectric response of ferroelectric materials. This type of polarization occurs due to motion of domain walls that separates regions of differently oriented dipoles. The polarization takes place by the growth of domains which have favorably oriented dipoles with respect to the applied field.

Some of the polarization mechanisms that were discussed above are schematically shown in Figure 2.6 [47] with and without external electric fields. For a given dielectric material the total polarization 'P' is the sum of all the individual polarization mechanisms. Electronic, ionic and dipolar polarization are called extrinsic polarization mechanisms as they are all non-lattice mechanisms. Space charge, orientation and domain wall polarization are called intrinsic polarization mechanisms as they originate from the crystal lattice of a given material [40, 41].

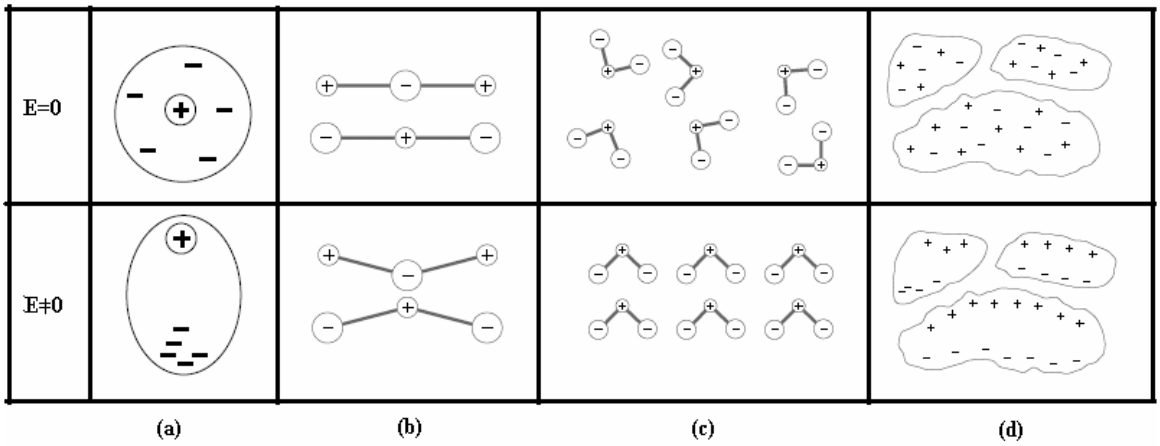

Figure 2.6: Polarization mechanisms. (a) electronic polarization (b) ionic polarization (c) dipolar polarization (d) space charge polarization [47].

Since polarization and dielectric permittivity (and hence relative permittivity ε_r) are directly related, the dispersion of dielectric response due to contributions from each polarization mechanism can be expressed by a complex relative permittivity ε_r^* [40, 46, 48].

$$\varepsilon_r^* = \varepsilon' - j\varepsilon'' \tag{2.13}$$

The real part of the permittivity, ε', is termed the dielectric constant and depends on the magnitude of polarization. It determines the amount of electrostatic energy stored per unit volume in a material for a given applied field, i.e. the amount of charge stored in a capacitor. The imaginary component of the permittivity, ε'', is called the loss factor and it is the mathematical representation of all the losses due to lag in polarization upon application of the field , energy dissipation associated with charge polarization and energy loss in a material due to heat.

Dielectric losses are usually described by the loss tangent tanδ.

$$\varepsilon_r^* = \varepsilon'(1 - j\ tan\delta) \tag{2.14}$$

Where,

$$tan\delta = \frac{\varepsilon''}{\varepsilon'} \tag{2.15}$$

2.2.5 Polarization and Frequency

When an alternating field is introduced, the polarizability of the dielectric material is selectively excited by different polarization mechanisms at different frequencies. The contribution of different polarization mechanisms emerges when the dielectric response of a material is studied across a wide frequency range. As was described in the previous section, these contributions stem from minute movements of particles that respond to an electric field. The contribution of a particular polarization mechanism(s) at a particular frequency range depends upon the mass of the particle that initiates it. For example at radio frequencies a point is reached where the molecules of the material (molecular polarization) can no longer rotate fast enough to contribute to the net polarization. As a result the polarizability of the material reduces in magnitude as frequency increases. At a frequency range above the infrared region, only the electronic polarization remains effective because it is due to electrons which are still able to follow the field at high frequencies. At still higher frequencies, even the electronic contribution to polarizability vanishes. The variation of polarizability due to extrinsic contributions with frequency is shown in Figure 2.7 [41] where α_e, α_i, α_d stand for electronic, ionic and dipolar polarizations which occur up till frequencies ω_e, ω_i, ω_d respectively. The frequencies ω_i and ω_d depend on the material under study but their orders of magnitude remain in the regions indicated in the figure [41].

In Figure 2.7, relaxation behavior is observed in a frequency range extending from ω=0 to ω= ω_d which is due to dipolar (molecular) polarization and internal mechanisms namely orientation, domain wall and space charge polarization. A resonance behavior is observed from the end of the microwave band which is due to ionic and electronic polarization. The resonance behavior leads to an increase in both the real part of permittivity and the loss tangent [46]. Again, since relative permittivity is directly related to polarizability, the variation of dielectric constant (ε') with frequency follows a similar pattern as shown in Figure 2.8 [40].

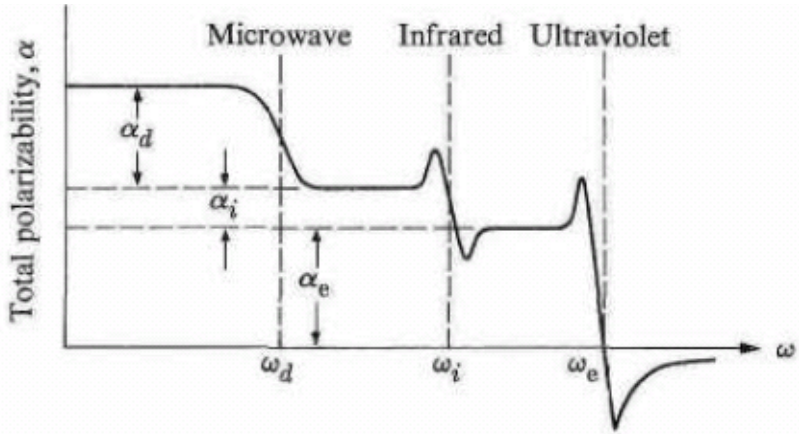

Figure 2.7: Variation of total polarizability of a dielectric material with frequency [41].

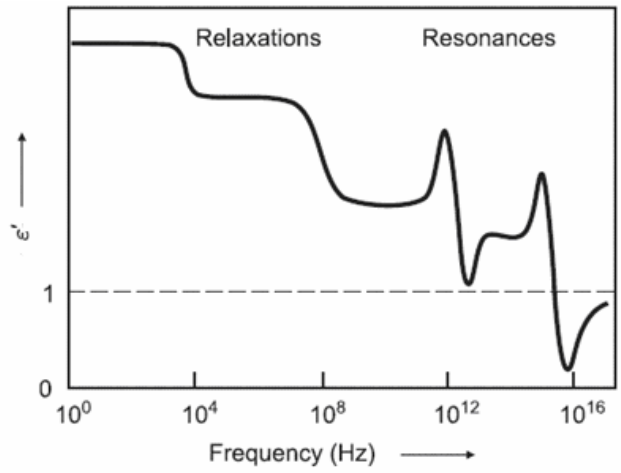

Figure 2.8: Frequency dependence of real part of relative dielectric permittivity [40].

2.3 Effect of Electric Field on the Behavior of Ferroelectric Materials

Large amplitudes of externally applied field lead to strong non-linearity in ferroelectric materials. These significant non-linearity's and electric field tunable permittivity's open up a broad field of applications for ferroelectric materials especially for developing passive tunable components (like capacitors) for phase shifters, filters and matching networks. Therefore it is important to understand the effects of large amplitudes of externally applied fields on ferroelectric films.

When Capacitance-Voltage (CV) measurements are done on ferroelectric films at frequencies of interest a small A.C. ripple propagates through the film along with the applied D.C. bias. The small increase in permittivity when bias is initially applied is due to the movement of domain walls whose motion was inhibited by defects in the ferroelectric film (a phenomenon called domain wall pinning). But with further application of bias the domain walls become immobile and extrinsic contributions to particle movements are nullified due to elastic constraints [49-53]. Therefore at high applied fields the A.C signal is mainly probing the intrinsic contributions to dielectric response.

As the D.C bias is decreased the extrinsic contributions again start influencing the dielectric behavior again and the contributions reach a maximum point at zero bias. These particle movements result in dielectric losses as described in previous sections, therefore maximum permittivity accompanied by maximum losses are observed at zero bias. Conversely, minimum permittivity and losses are observed at maximum bias value. Thus the variation of capacitance (or dielectric permittivity) of a ferroelectric film with positive and negative bias voltages assumes a characteristic bell-shaped curve [50].

A clear distinction is observed in the CV characteristics of ferroelectric films in the ferroelectric phase and paraelectric phase. In the ferroelectric phase, a "butterfly loop" is obtained theoretically with two distinct peaks in capacitance values. These peaks correspond to different domain orientations formed on a film in the ferroelectric phase [50, 51]. In the paraelectric phase no "butterfly loop" is observed due to absence of hysterisis behavior. The CV characteristics of a ferroelectric film in ferroelectric and paraelectric phases respectively are depicted in Figure 2.9 [40].

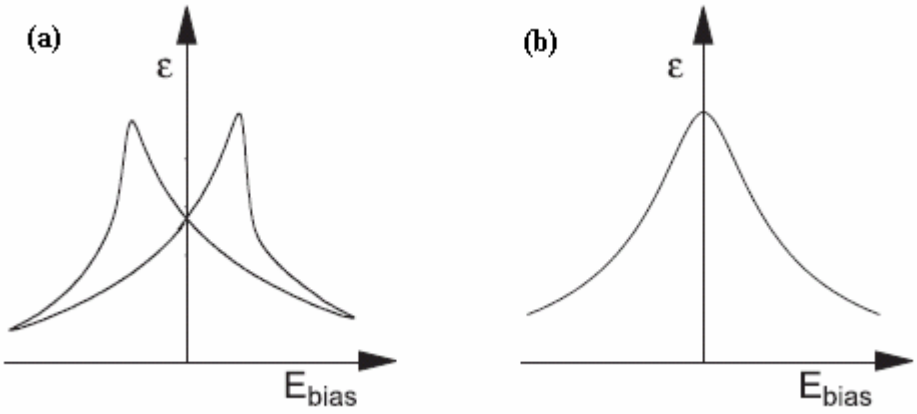

Figure 2.9: Variation of permittivity with applied bias for a ferroelectric material in (a) Ferroelectric phase (b) Paraelectric phase [40].

For high frequency applications the variation of dielectric permittivity of a ferroelectric material with applied bias is an important property. This characteristic is commonly called tunability (n) which is expressed in terms of relative dielectric permittivity (ε_r) as

$$n = \frac{\varepsilon_{r(\max)}}{\varepsilon_{r(\min)}} \tag{2.16}$$

In (2.16) tunability is expressed as a ratio of maximum and minimum relative permittivities, ε_r. Tunability can also be expressed as a percentage as shown below

$$n\ (\%) = 100 * \frac{(\varepsilon_{r(\max)} - \varepsilon_{r(\min)})}{\varepsilon_{r(\min)}} \tag{2.17}$$

Usually there is a trade-off between tunability and loss tangent and a microwave has engineer has to judiciously choose a material wherein there is optimal trade-off between these two parameters for a better device performance. A ferroelectric material for microwave applications is usually operated in the paraelectric stage, close to Curie temperature to ensure high tunability and low loss tangent [53]. It is inevitable that a large electric field has to be applied to obtain large tunability in ferroelectric thin films. For example a Metal- Insulator-Metal (MIM) type capacitor with a ferroelectric material as a dielectric requires electric fields in the range of 1000KV/cm to obtain a high tunability [54, 55]. The quality factor (Q-factor) is used to characterize the losses in lumped circuit elements. Quality factor can be defined as the ratio of stored energy to the average energy dissipated in the system per cycle.

At low frequencies, the capacitances of a ferroelectric material like BST in the paraelectric phase decreases monotonically with applied bias. The reason for decrease in permittivity's with increase in frequency has been explained in the Section 2.2.5. The increase in magnitude of externally applied bias further restricts the extrinsic polarization mechanisms in the material, hence the steadily decreasing permittivities (or capacitances) with increasing frequencies and electric fields. Typical capacitance-frequency curves for 1V increments in applied bias voltages for $Ba_{0.5}Sr_{0.5}TiO_3$ thin films is shown in Figure 2.10 [56].

At high frequencies a resonant dips appear in the reflection coefficient data under bias which is not observed at low frequencies. The depth of these resonant dips varies with bias and the frequencies at which these dips occur depend on the device layer structure. This is now understood to be a consequence of the electrostrictive property also called the "field-induced piezoelectricity" of the material [56].

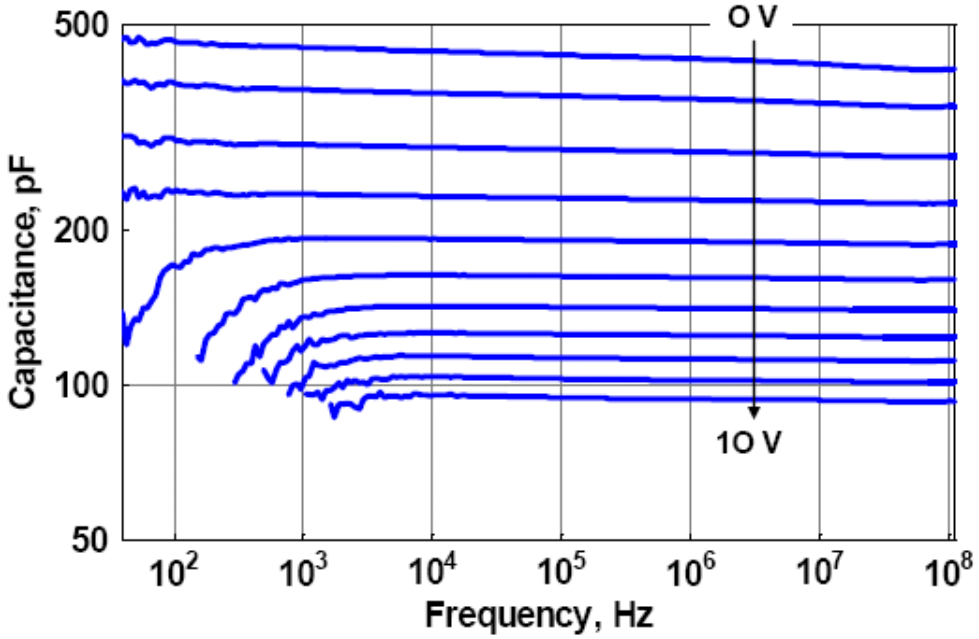

Figure 2.10: Variation of capacitance of $Ba_{0.5}Sr_{0.5}TiO_3$ thin films with frequency for 1V increments in bias [56].

Electrostriction is a non-linear electromechanical coupling mechanism in centro-symmetric crystals as opposed to piezoelectricity which occurs in non-centrosymmetric crystals. Electrostriction is defined as the coupling that exists between the strain developed in a material and the electric field applied. Electrostriction is tunable, reproducible and non-hysteretic. This phenomenon exists in all insulating materials. Though electrostrictive effects are feeble compared to piezoelectric effect in most crystalline materials, they may be quite large in ferroelectric materials [57, 58].

This bias-induced resonance at high frequencies observed in Barium Strontium Titanate and Strontium Titanate has an adverse residual effect on the loss properties of the device. It is extremely important to understand and characterize these resonances in order to obtain reliable capacitors for tunable microwave applications [54, 56]. Figure 2.11 shows the bias-induced resonant dips observed in BST-based MIM capacitor with increasing bias values [56].

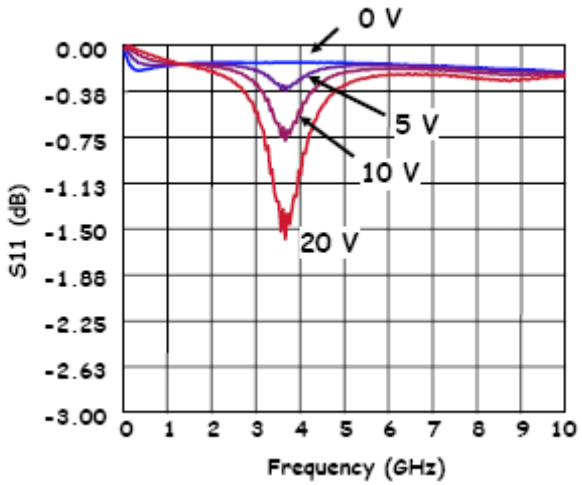

Figure 2.11: Bias-induced resonant dips observed in BST-based MIM capacitor from 0-20V in 5V increments [56].

A time-dependent decrease in resistance under applied DC bias is observed in both bulk and thin film titanate dielectrics [59-61]. Waser at al [62] have suggested that resistance degradation occurs due to migration of charged oxygen vacancies. Resistance degradation is quantified by measurement of the characteristic time required for the leakage current density to increase by an order of magnitude from its steady state value. Resistance degradation is reported to a big factor in BST thin films[60, 61, 63].

2.4 Material Properties of Barium Strontium Titanate (BST)

$Ba_{1-x}Sr_xTiO_3$ is a continuous solid solution between two traditional ferroelectrics- Barium Titanate ($BaTiO_3$) and Strontium Titanate ($SrTiO_3$). The Curie temperature of BST decreases linearly with increasing Sr concentration at a rate of 3.4º C per mole % Sr. Therefore BST's Curie temperature and hence its properties can be tailored over a wide range to meet the requirements of different applications [15]. This kind of flexibility in properties and hence the prospective application range is absent in conventional ferroelectric ceramics. The various applications for which BST is being currently researched for are shown in Figure 2.12.

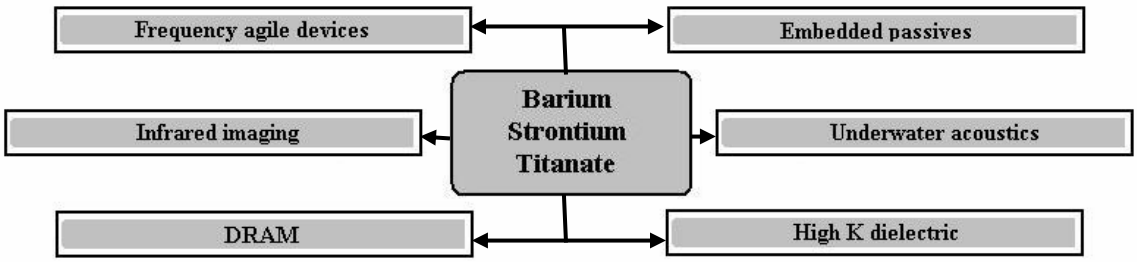

Figure 2.12: Prospective areas of application of barium strontium titanate.

In this section the crystal structure, phase transition behavior, polarization behavior and microstructure of Barium Strontium Titanate and the influence these properties have on its electric performance are discussed.

2.4.1 Crystal Structure

BST crystals exist in both cubic and tetragonal symmetry depending upon the (Ba/Sr) ratio and the corresponding Curie temperature of the chemical composition. BST belongs to the family of ABO_3 perovskites. In BST, Ba^{2+} and Sr^{2+} occupy the corners of the cube and they are shared between 8 adjacent cells. This gives a total of 0.5 Barium atoms and 0.5 Strontium atoms per cell. Six oxygen atoms occupy the face-centered position on the six sides and since each is shared between two adjacent cells, which makes it three oxygen atoms per cell. Ti^{4+}, which is the smallest of the atoms in the crystal, is located in the center of the cubic cell. It is relatively free to move and the spontaneous polarization of BST is mainly attributed to the movement of the Ti atom [53, 58]. The crystal structure of BST in its cubic phase is shown in Figure 2.13.

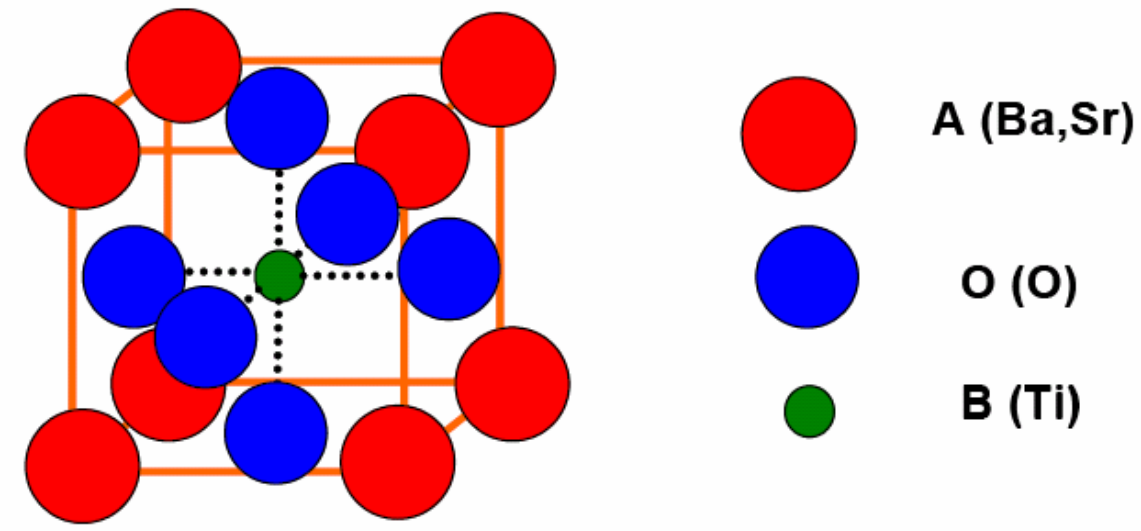

Figure 2.13: The perovskite crystal structure of BST in cubic phase with no externally applied electric field [53].

2.4.2 Phase Transitions

Due to the different behavior of its parent ferroelectric materials $BaTiO_3$ and $SrTiO_3$ the phase transition behavior of BST evolves with composition. The variation of Curie temperature and lattice parameters (defined as the spacing between unit cells) of BST with Barium composition is shown in Figure 2.14 [64].

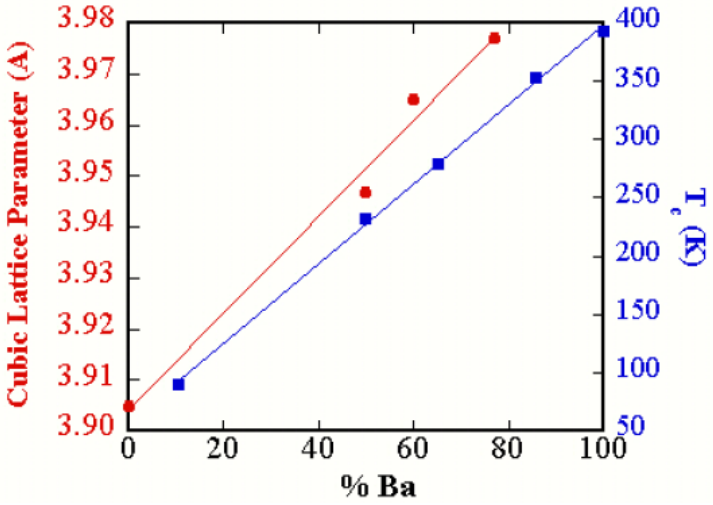

Figure 2.14: Variation of Curie temperature and lattice parameters of BST with change in Barium percentage composition [64].

$BaTiO_3$ (T_c=393K) is a prototype ferroelectric which undergoes a sequence of crystal structure transitions as it switches from ferroelectric to paraelectric phase [41]. $SrTiO_3$ is an incipient ferroelectric i.e. it exhibits quantum ferroelectricity which means that though it undergoes phase transition at very low temperatures (T_c=105K), the quantum effect prevents complete transition to paraelectric phase. Therefore $SrTiO_3$ exhibits ferroelectric behavior well above its Curie temperature or paraelectric effect well below Curie temperature [54, 65]. BST undergoes structural changes as it undergoes phase transitions like $BaTiO_3$ for Ba concentrations varying from 20 to 100%. As the composition of BST comes close to pure

$SrTiO_3$, its behavior is complicated by the competition between prototype ferroelectric transitions and quantum ferroelectric transition related instabilities.

The variation of dielectric constant of BST with temperature for different concentrations of barium and strontium are given in Figure 2.15 [66]. It suggests that BST with x=0.5 is ideal for room temperature tunable microwave applications. This is because for this composition the relative dielectric permittivity is high and phase transitions occur at temperatures well below room temperature. Hence a good trade-off is obtained between dielectric permittivity and losses [16].

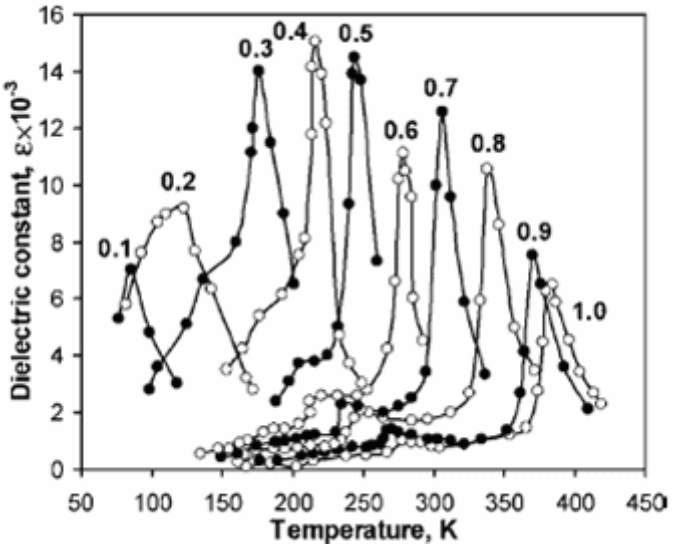

Figure 2.15: Variation of dielectric constant of BST for different concentrations of barium and strontium [66].

The phase transition behavior of BST also varies with thickness. The important occurrences that have been observed in the phase transition properties of BST with variation in thicknesses are-

The variation of dielectric constant with temperature becomes less and less pronounced with decrease in thickness. At thicknesses in the range of 100 nm, the dielectric constant shows almost no variation with temperature. Thus it would advantageous to use thin BST

films for applications that require stability in device performance with variations in temperature [15, 67]. The comparison of variation of dielectric constant with temperature for ceramic and thin film $Ba_{0.7}Sr_{0.3}TiO_3$ is shown in Figure 2.16(a) [15].

The sharp peak in permittivity that is observed in the phase transition region for thick films is suppressed more and more as the film thickness becomes lesser and lesser. The phase transition region gets spread over a wider range of temperature (diffuse phase transitions). Hence characterization of BST thin films becomes more complicated as ferroelectric behavior might be observed in paraelectric region and vice versa [68]. The origin of this variation in properties of ferroelectrics with decrease in thickness has still not been well understood. In one of the theories it has been suggested that though the "apparent" Curie temperature obtained from Curie-Weiss plots from as-measured data suggests a diffuseness in phase transitions accompanied by shift in Curie temperatures, the "inherent" Curie temperature does not change with thickness [69]. The variation of permittivity with temperature for six different film thicknesses of $Ba_{0.7}Sr_{0.3}TiO_3$ is shown in Figure 2.16(b).

It has also been reported that the Curie temperature of BST thin films fabricated on various substrates increases due to the internal stress of the films arising from the difference in Thermal Coefficient of Expansion (TEC) and/or difference in the lattice parameter between the film and the substrate [54, 70].

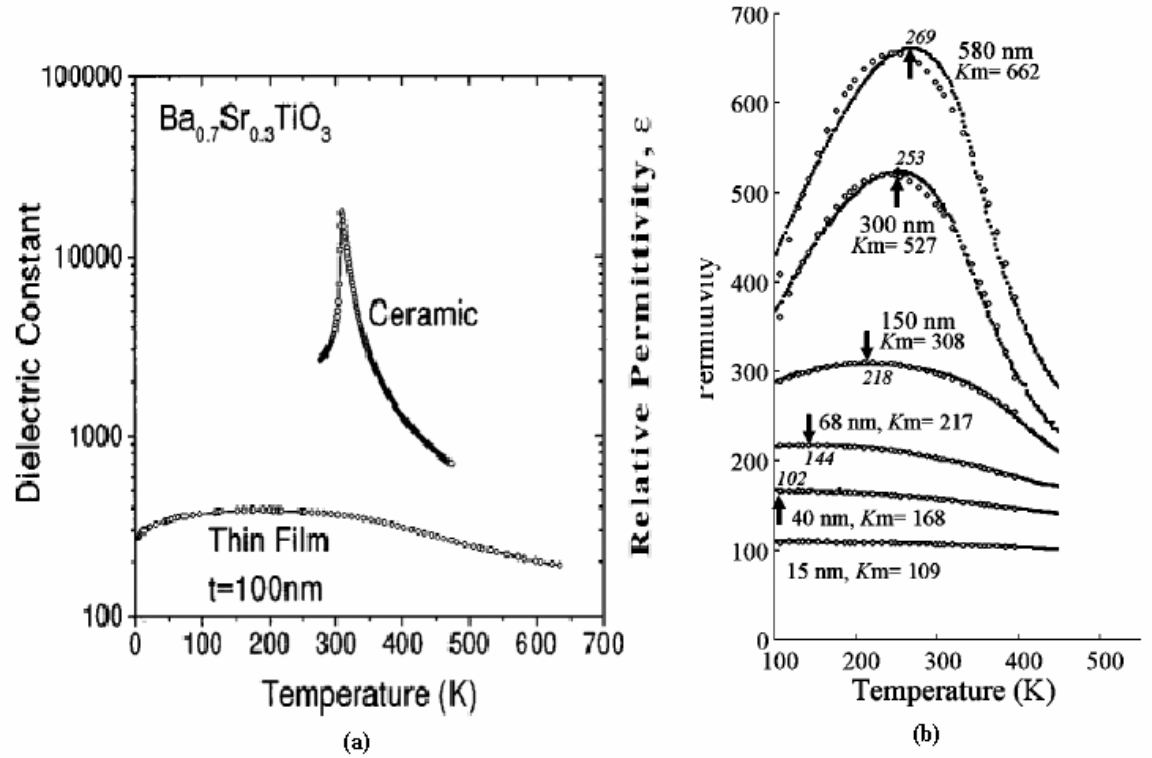

Figure 2.16: Phase transition behavior of $Ba_{0.7}Sr_{0.3}TiO_3$. (a) Comparison of variation of dielectric constant with temperature between ceramic and thin film $Ba_{0.7}Sr_{0.3}TiO_3$[15], (b) Difference in phase transition behavior with decrease in film thickness (K_m is the maximum permittivity value) [68].

$Ba_{1-x}Sr_xTiO_3$ films with $x<0.7$ show little hysterisis behavior at room temperature and above. A very weak hysterisis behavior is observed for films with x value ranging from 0.7 and 0.9 as seen from Figure 2.17 [71] which shows the results of Polarization-Electric field (P-E) measurements done on $Ba_{1-x}Sr_xTiO_3$ thin films at room temperature.

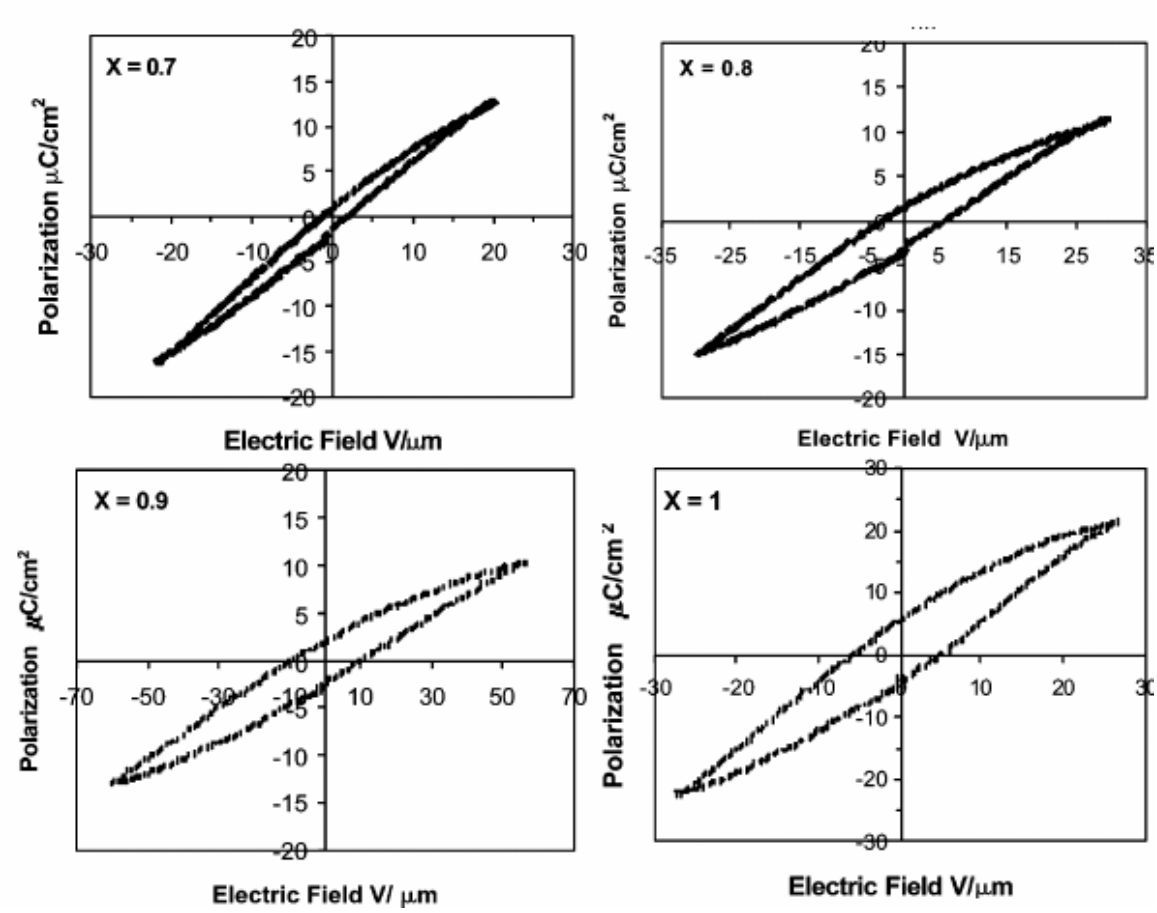

Figure 2.17: *P–E* hysterisis loops for $Ba_xSr_{1-x}TiO_3$ thin films at room temperature [71].

2.4.3 Polarization

The general prediction of mean-field models is that near the surface of a ferroelectric thin film, the polarization normal to the surface should continuously decrease from the bulk value [72]. It has been theoretically concluded that there exists a surface modified layer in a thin film when the ferroelectric material in paraelectric phase. The polarizability of material near the surface is reduced relative to a bulk ferroelectric. The effect of the reduced polarizability is the reduced overall capacitance of the film. The films behavior suggests a total suppression of the ionic contributions to the polarization due to this "dead layer" in the surface[73].

The domain structure of thin films is also affected by growth stresses, lattice mismatches and thermal expansion mismatch stresses imposed by the substrate[59]. In the case of perovskite materials like BST, tensile stress at the transformation temperature pulls the polarization into the plane of the film, while compressive stress leads to polarization being directed normal to the surface. Tensile stress leads to high dielectric constants and low remnant polarizations and compressive stresses lead to the opposite [74-76]. Tensile stresses are advantageous for acoustic applications as the hysterisis losses decrease. Since varactors are operated in the paraelectric phase and thin films are generally used, the polarization and hence the effects of stresses are negligible.

Many ferroelectric films undergo a slow polarization when a voltage is applied to the capacitor and the current resulting from the polarization follows an inverse power law over many decades in time [77-79]. This is known as Curie von Schweidler law and it has an exponent of close to unity. Discharging also follows the same pattern but with a current of opposite polarity. The polarization on charging and discharging is directly related to

capacitance and dielectric losses. In BST thin films dielectric relaxation is a dominant cause of dielectric loss. The origin of the relaxation currents is poorly understood and several mechanisms to explain these currents have been put forward in literature [59, 80-83]. Figure 2.18 [59] shows the thickness dependence of relaxation currents observed in BST thin films for thicknesses varying from 8 nm to 100 nm keeping the electric field constant at 167 KV/cm.

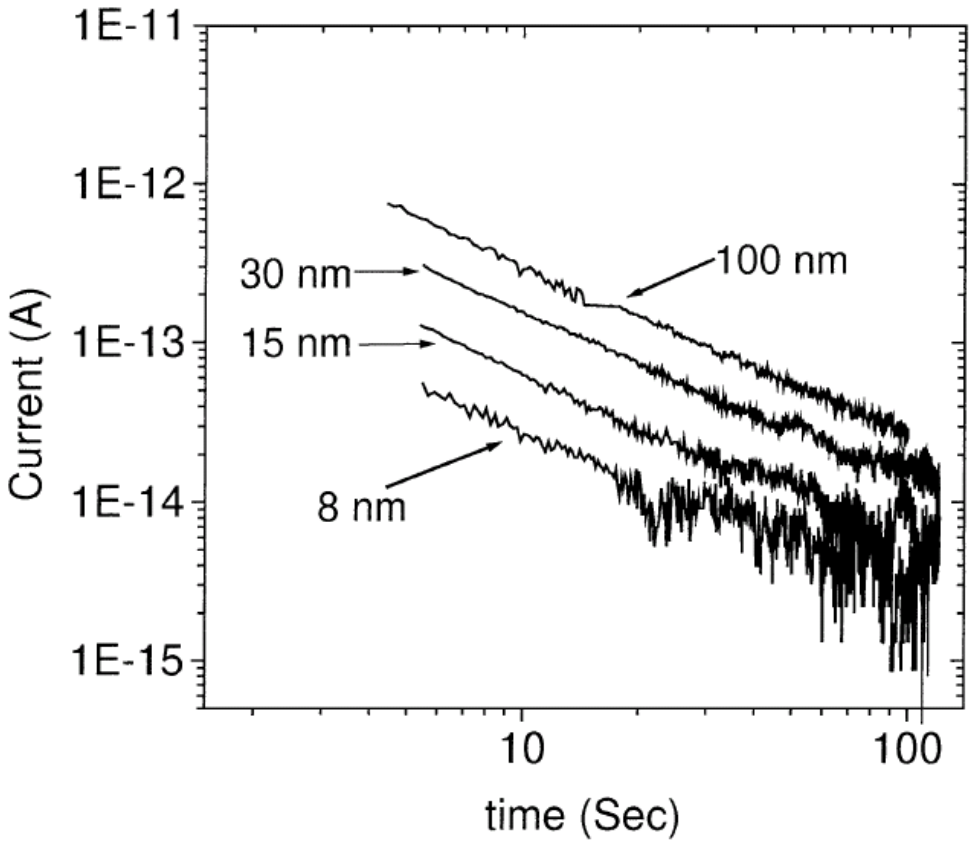

Figure 2.18: Thickness dependence of relaxation currents observed in metal organic chemical vapor deposited BST thin films [59].

2.4.4 Microstructure and Point Defect Chemistry

The microstructure of the thin film influences many properties of thin films. It is extremely important to keep the microstructure of the film constant while studying the properties of a thin film. For ferroelectric thin films it becomes even more important because of the "size effects" (huge variation in properties from bulk to thin films) whose origins and effects are yet not completely understood [59, 69].

The crystallinity of BST thin films affects its dielectric properties. The XRD spectrum of a sintered BST target is shown in Figure 2.19 [84]. York et al. [85] have reported (100) orientation is more preferable and leads to smoother films. The substrate and the deposition parameters play a major role in deciding the crystallinity of thin films. Usually polycrystalline films are obtained on silicon. Magnesium Oxide (MgO) and Lanthanum Aluminate ($LaAlO_3$) are preferred substrates for obtaining single crystalline and epitaxial BST films [86].

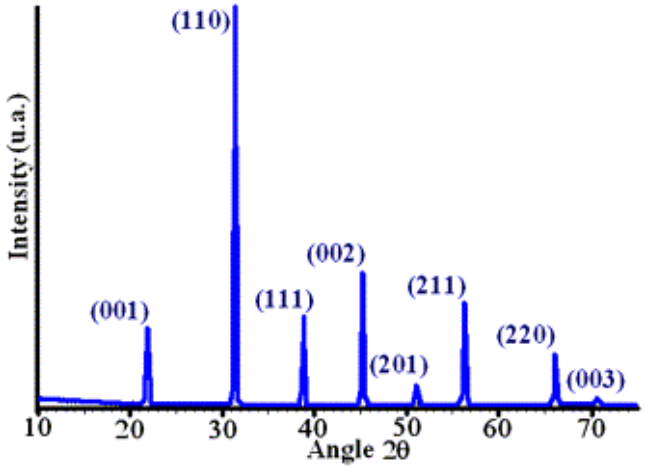

Figure 2.19: X-ray diffraction spectrum of sintered BST target [84].

A film with good texture reduces the variability in the performance of devices fabricated in the same wafer. Finally it is important to note that crystallinity does not contribute to the

"size effects" in ferroelectric thin films and that films with low crystallinity display subdued dielectric properties irrespective of the deposition method used [59].

The grain size of thin films strongly depends on the deposition method and in general ferroelectric thin films with grain sizes below 1 μm show a steady decrease in dielectric permittivity due to existence of a low permittivity layer in the grain boundaries. The grain size decreases with increase in strontium content and the dielectric permittivity decreases with decrease in grain size [59, 71]. The existence of a low permittivity layer at the grain boundaries is the main reason for the decrease in dielectric permittivity[59]. In polycrystalline BST thin films, the grain boundaries play a major role in decreasing dielectric permittivity. The [(Ba+Sr)/Ti] ratio has a strong effect on the dielectric behavior of BST thin films. Maximum value of dielectric constant is found when [(Ba+Sr)/Ti] ratio is equal to unity. When the amount of excess Ti in the film increases the relative permittivity monotonically decreases [87]. In films with a columnar structure, grain boundaries have a negligible effect on the overall permittivity as they lie perpendicular to the electrode. In fine grain films they have a marked effect (depending on the grain size) as they lie parallel to the electrode layer [59].

The behavior of BST based capacitors under high electric fields depends on the migration of ionic defects. Hence a greater knowledge of the concentration and behavior of mobile point defects is necessary for accurate modeling. The point defect chemistry of thin films is strongly influenced by the presence of nearby interfaces and interdiffusion of ions across the interfaces [59]. Analysis of nature, volume and behavior of various ionic defects is complicated and many direct and indirect methods have been put forward [88, 89].

2.5 BST Device Technology for Tunable Microwave Applications

BST thin films offer a low cost scalable varactor technology and it is the most widely researched material for the current generation of tunable RF and Microwave components and systems. As illustrated in Figure 2.20, the high dielectric constant of BST makes it suitable for small area capacitors which in turn make smaller device packages possible [15].

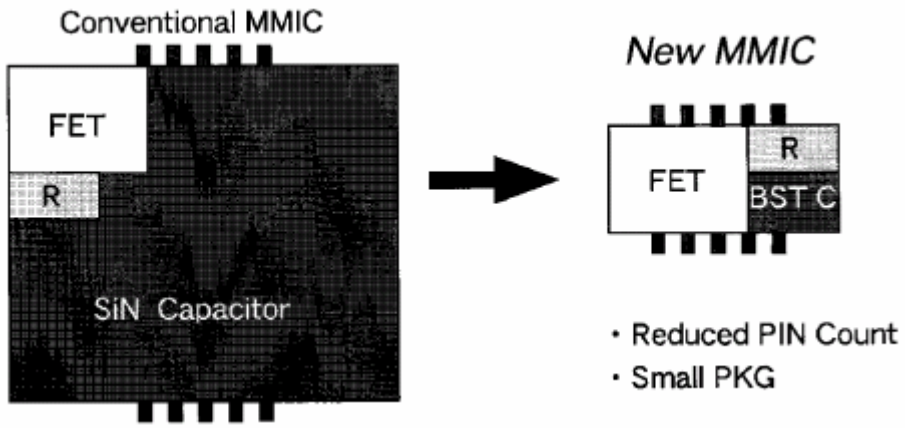

Figure 2.20: Reduction in device packages using BST capacitors [15].

BST and Micro-Electro-Mechanical-Systems (MEMS) technologies are the current competing technologies for low-cost tunable circuits. The cost reduction is achieved by using inexpensive substrates and employing high-volume deposition technologies. While the BST varactors are cheaper to fabricate and to process, the MEMS counterparts offer excellent power-handling capabilities. The applications that favor thin-film BST technologies are-

- Phase-shifters or delay lines which require rapid and continuous tuning at low voltages.
- Frequency-agile components like tunable matching networks, splitters, mixers, multipliers etc. that exploit the non-linear dielectric properties [90].

The two most widely reported device geometries for BST varactors are the Interdigital (IDT) structure and the Metal-Insulator-Metal (MIM) structure which are shown in Figure 2.21(a) and 2.21(b) [91].

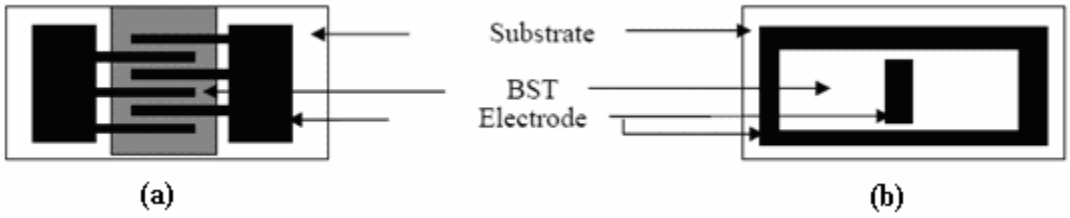

Figure 2.21: Two different configurations of BST varactors. (a) Parallel Plate Capacitor (b) Interdigital Capacitor [91].

The IDT structures are easier to fabricate as they require only a single step metallization while the fabrication of MIM structures require at least a three step process. The IDT structures can be processed at high temperatures as they are fabricated directly on the substrate while in MIM structures the chemical stability of the bottom electrode decides the processing temperature. IDT structures suffer from reduced tunability due to large fringing electric field in the air while MIM structures offer higher tunabilities as the fields are better confined between the top and bottom electrodes. Typical operating voltages of MIM structures are <30V while IDT structure operating voltages are in the range of 100V's.

The MIM structures are ideal for evaluating the dielectric properties of BST thin films due to the direct relation between the measured capacitance and the relative dielectric permittivity. Hence this research is mainly focused on evaluating the dielectric properties of BST thin films at high frequencies using MIM structures. The various material issues in MIM structures are further discussed in Chapter 3.

2.6 Deposition Technologies for BST Thin Films

The deposition process used to prepare the film is one of the major parameters that decide the material properties of BST thin films. A careful study of the influence of growth parameters on material properties and correlation with electrical properties is imperative. There are four main deposition methods that are used for obtaining BST thin films for device applications. They are-

- Chemical Solution Deposition or Sol-gel Deposition (CSD)
- Pulsed Laser Deposition (PLD)
- RF Magnetron Sputtering
- Metal Organic Chemical Vapor Deposition (MOCVD)

The advantages and disadvantages of the deposition methods are listed in Table 2.2 [53].

Table 2.2: Different deposition methods and their advantages and disadvantages[53].

Method	Advantages	Disadvantages
Chemical Solution Deposition	Simple and rapid Low capital investment Film stoichiometry	Repeatability Scalability Morphology
Pulsed Laser Deposition	Good film quality Film stoichiometry	Formation of particulates Scalability Low volume deposition
RF Magnetron Sputtering	Uniformity Scalability High volume deposition	Film stoichiometry Defect concentration Residual stresses
Metal Organic Chemical Vapor Deposition	Flexibility Scalability High volume deposition	Lack of suitable precursors Control Complexity

Sputtering is compatible with high production requirements and promising for development of low-cost microwave circuits. Sputtering is the most widely used deposition technique for a variety of metals and dielectrics. In this research work RF Magnetron sputtering has been employed to obtain good quality BST thin films. The basic principles of sputtering and a description of the deposition parameters and their effect on the material properties of the BST thin films are provided in Chapter 3.

2.7 Material Characterization in the High Frequency Regime

Important applications of microwaves result from their interaction with various types of materials. Microwaves penetrate partially in a metal and flow in a narrow band near the outside surface. The current density falls off exponentially from the surface of the conductor to the center. At a certain depth called the "Skin depth" (δ) the signal amplitude is 36.8% of its surface amplitude where,

$$\delta = \sqrt{\frac{2}{\omega\sigma\mu}} \tag{2.18}$$

σ is the electrical conductivity and μ is the permeability of the metal. Thus 95% of the current flows through a depth of 3δ. Therefore only thin metal plating is required for microwave components.

However microwaves freely flow through dielectric materials inducing a net polarization. The combination of these two interactions of microwaves enables the development of a reflection method which permits the measurement of a materials dielectric properties in the high frequency regime [46].

Planar transmission lines are ideal for material characterization related microwave measurements as they can be easily fabricated using conventional lithography techniques and

are easily integrated. Planar transmission lines are available in various geometries. Three geometries are widely used in material characterization: stripline, microstrip and coplanar waveguide. In this research work the capacitors are fabricated in Coplanar Waveguide (CPW) transmission line configuration as they offer simple bias schemes by obviating the necessity for via holes. The classic CPW configuration is shown in Figure 2.22 [92].

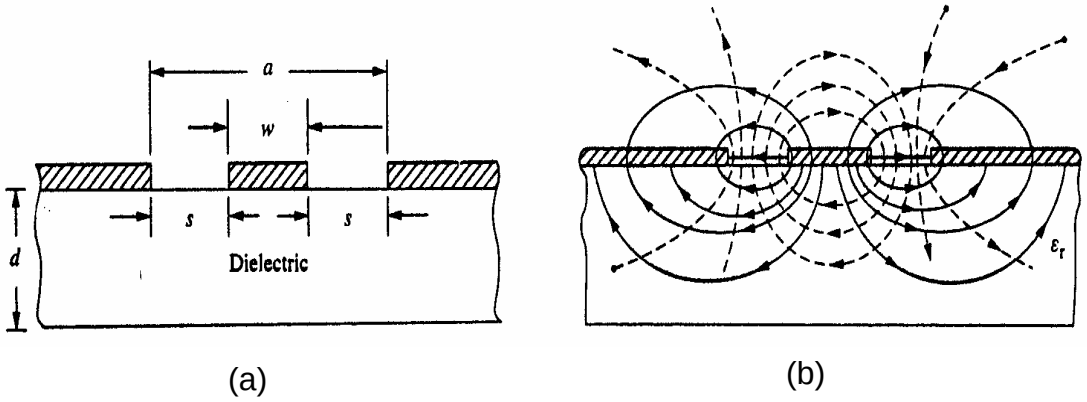

Figure 2.22: Coplanar waveguide configuration. (a) structural dimensions (b) field distributions with solid lines describing electrical fields and dashed lines representing magnetic fields [92].

Microwaves travel in different modes in different transmission lines. In the CPW line they travel in the quasi-Transverse Electromagnetic mode or quasi-TEM mode. The RF electric field between the center conducting strip and the ground electrodes tangential to the air-dielectric boundary produces a discontinuity in displacement current density at the interface, giving rise to an axial, as well as transverse, component of RF magnetic field [92, 93]. In this research work high frequency measurements are done on varactors fabricated in CPW configuration.

CHAPTER 3:

VARACTOR PROCESSING

3.1 BST Based Metal Insulator Metal Structure

Commercial electronic circuits are stringent with respect to voltage requirements and BST based parallel plate structures require low bias voltages to provide the desired tunability which makes them more flexible and compatible for many circuit applications. The important material issues to be considered in BST based MIM structures are summarized in Figure 3.1 [15].

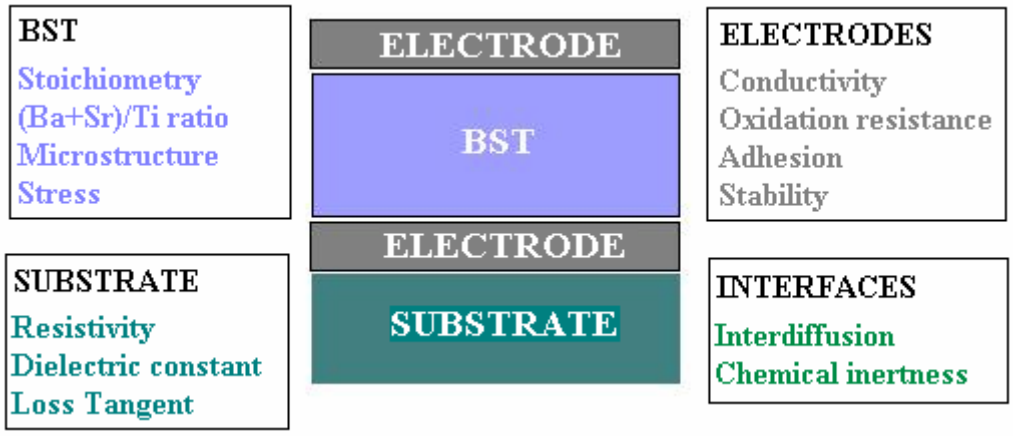

Figure 3.1: Material issues to be considered in BST based MIM structure [15].

High-resistivity silicon (3-4 KΩ-cm) has been used as the substrate for this research work due to its low loss tangent and low cost compared to other substrates like sapphire. Since BST deposition is done at relatively high temperatures ranging from 450ºC to 700ºC in the presence of oxygen gas it become important to use a very stable and oxidation-resistant metal as the bottom electrode. Hence noble earth metals like Platinum (Pt), Ruthenium (Ru)

and Iridium (Ir) or their conducting oxides are preferred for use as bottom electrodes. In this research work Pt has been used as the bottom electrode due to its oxidation resistance and high conductivity compared to metal oxides.

Typically, a Silicon dioxide (SiO_2) diffusion barrier layer is grown on silicon substrate before depositing Pt to prevent diffusion of platinum through the substrate during BST deposition. Additionally an adhesion layer is required for platinum and development of a stable adhesion layer is a major challenge as interdiffusion between layers is a major issue with BST based MIM structures as BST deposition happens at high temperatures in oxidizing conditions. A very thin Titanium (Ti) or Titanium dioxide (TiO_2) adhesion layer is usually deposited before depositing platinum. The interface issues as a result using elemental Ti as the adhesion layer and SiO_2 is further discussed in Chapter 4.

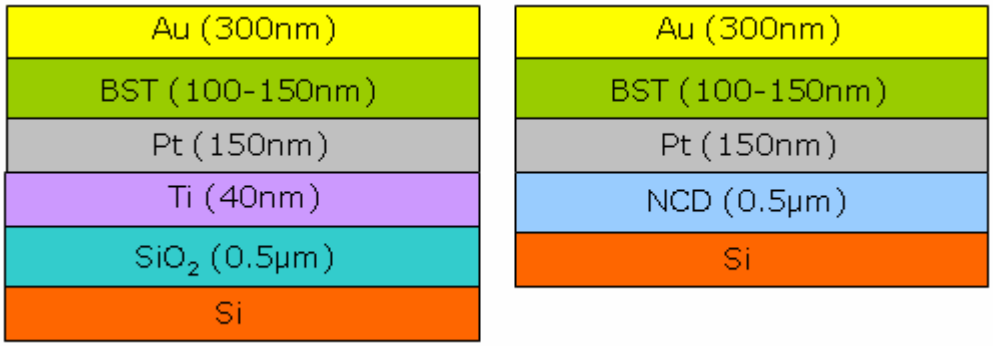

Figure 3.2: Schematic of stacked BST Metal Insulator Metal structures.

As mentioned earlier, in this research work MIM structures using Nanocrystalline Diamond (NCD) films as the diffusion barrier layer are also investigated. The NCD films were deposited using Microwave Plasma Enhanced Chemical Vapor Deposition (MPECVD) technique. The cross-section of the two bottom electrode stacks used for BST varactor fabrication along with the thickness of each layer is shown in Figure 3.2.

Further discussions on the interface quality and electrical performance obtained with the SiO_2 based and NCD based MIM structures are in Chapters 4 and 5. Gold (Au) is used as the top electrode in both MIM structures (Figure 3.2).

3.2 RF Magnetron Sputtering

Sputtering is a physical process whereby atoms and ions in a solid target material are ejected into the gas phase due to bombardment of the material by energetic ions. The sputter gas is inert, and in most sputtering systems argon is used as the sputtering gas. Sputtering is done at pressures in the order of 10^{-6} Torr or more inside specially designed chambers. Inside the chamber, the target material to be sputtered is bonded on to a one circular electrode which acts as cathode and is placed in front of the substrate to be coated. Gas is introduced and maintained at a suitable pressure in the chamber which is ionized by a suitable voltage applied between the two electrodes.

As the target is subjected to a negative electrical potential compared to the plasma body, the positively charged ions in the plasma will be accelerated towards the object. At the target surface a number of processes and combinations of them can occur. As shown in Figure 3.3 [94], in (a) the arriving ion is adsorbed onto the surface, and a chemical or physical bonding is created. The incoming species may also transfer some of its momentum to one of the surface atoms (b), and cause it to move around on the surface (displacement). If the energy of the incoming ion is sufficiently high it may start to remove some of the surface atoms (sputtering, shown in (c)), and if the energy is increased even further, the incoming ion can be implanted (d). In addition, there can also be a number of combinations of these processes. Sputtering is initiated when the energy of the incoming atom or ion is of the order of 100 eV, while implantation occurs at ~ 1 keV. Naturally, there are no distinct borderlines between the

different processes, but in reality they overlap each other. Also, these processes are strongly dependent on the chemical and physical properties of the involved atoms and ions. These processes are important in many plasma assisted thin film growth techniques and found the basis for most plasma-based applications in the field of thin film growth. The schematic of these processes is shown in Figure 3.3 [94].

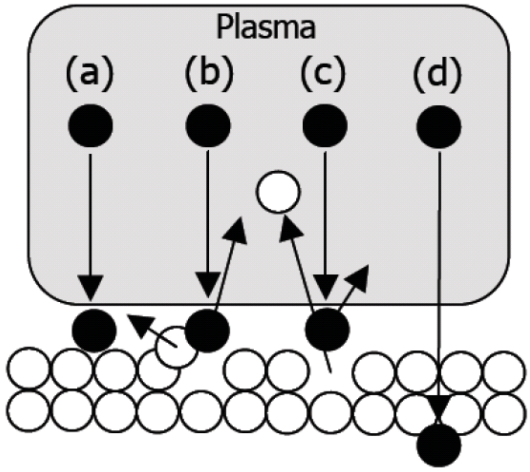

Figure 3.3: Processes initiated by bombardment of ions onto the sputtering target. (a) Adsorption, (b) displacement (momentum transfer), (c) removal of surface atom (sputtering or etching), (d) ion implantation [94].

The sputtered atoms then become part of the plasma, as neutral atoms or ions (if they are ionized). The sputtered atoms are then available for deposition. Sputtering is typically a high voltage, low current discharge (hundreds of volts and tens of $mAcm^{-2}$). The basic schematic of the sputtering process is shown in Figure 3.4.

Magnetron sputtering is done by introduction of static magnetic field. Among the various configurations available, the most commonly used is magnetron sputtering with circular target. Magnetron sputtering works on the principle of magnetic confinement of charged particles thereby increasing ionization within regions close to the target. In such a situation, the electrons are trapped within the magnetic field flux lines and ions are accelerated towards

the target. The application of high voltage initiates plasma between the cathode and the anode at pressures in the mTorr range. The ion bombardment of the cathode causes secondary electrons to be emitted and sustains the plasma. The magnetic field is positioned parallel to the cathode surface and with proper orientation of the magnetic field polarity; the secondary electrons are confined within the drift loop. The increased confinement forms a region of high plasma density near the cathode which in turn causes a high current low voltage discharge. The high plasma density permits use of low pressures for material deposition and results in less gas scattering. The reduced gas scattering increases the kinetic energy of the sputtered atom increasing the atom transport from the cathode to the substrate. The cathode can be sputtered at a high rate owing to the high discharge current and thus high deposition rates can be achieved.

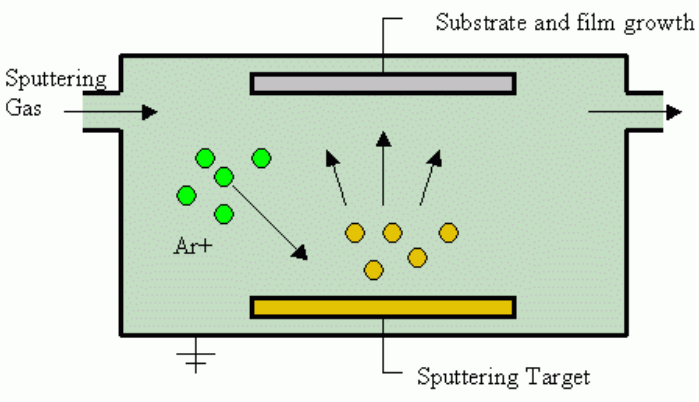

Figure 3.4: Description of the sputtering process.

Dielectric or insulating materials like BST are sputtered by using RF power instead of DC biasing to prevent charge accumulation at the surface of the target and results in electrical discharging or arcing wherein macro-molecules of target species are transported to the substrate and form poor quality films. Ionization of the gas in RF sputtering is caused by the electrons which are more mobile than ions and hence respond and oscillate with the

applied frequency. The deposition rate however, is reduced in RF sputtering due to reduced work done per cycle.

Figure 3.5: The CMS-18 sputtering system at the AMRL.

The Advanced Material Research Laboratory (AMRL) at the University of South Florida (USF) is equipped with the CMS-18 sputtering system which is used for depositing a variety of oxides and metals. The CMS 18 sputtering system at the lab in USF is shown in Figure 3.5.

BST depositions are generally done at temperatures in the range of 450ºC-700ºC to obtain crystalline films. To account for the loss of oxygen atoms at high temperatures oxygen gas is introduced in the chamber along with argon. The argon-oxygen ratio is one of the important deposition parameters that decide the quality of the deposited films. The other important parameters are RF power, substrate temperature, deposition pressure and distance between target and substrate.

In this research work $Ba_{0.5}Sr_{0.5}TiO_3$ thin films were deposited using RF magnetron sputtering and the deposition conditions were optimized to obtain BST thin films that display a good overall electrical performance.

3.3 Deposition of BST Thin Films by RF Magnetron Sputtering

Prior to this research work, the structural and electrical properties of $Ba_{0.5}Sr_{0.5}TiO_3$ deposited using Pulsed Laser Deposition (PLD) and RF magnetron sputtering were investigated [91, 95]. The sputtered BST films were found to be highly uniform over surface area and smooth compared to pulsed laser deposited films. The sputtered BST thin films displayed an average surface roughness of 3-5 nm while the pulsed laser deposited BST films showed high surface roughness values >15 nm due to particulate formation. No particulate formation was observed in the sputtered BST films. The electrical properties of the deposited BST films were investigated by fabricating MIM structures using BST as the dielectric. The top and bottom electrodes used were gold and platinum respectively. A loss tangent of 0.01 was obtained for the sputtered BST films which were much better than the pulsed laser deposited BST films and hence displayed much better quality factors. Breakdown voltage of sputtered BST thin films was 2 MV/cm, whereas PLD BST thin films was 1.02 MV/cm and this indicates that the sputtered BST thin films had good dielectric strength. The effect of Ar/O_2 (argon-oxygen) ratio on tunability was studied on sputtered BST films and an Ar/O_2 ratio of 90/10 produced the highest tunability. The deposition conditions were tailored to achieve a tunability and loss tangent of 2.8:1 and of 0.01 respectively in a frequency range of 10–200 MHz. The deposition conditions are summarized in Table 3.1 [95]. Owing to these conclusions, RF magnetron sputtering was the deposition method of choice in this research work. It was recommended that further

optimization of the deposition process was required to improve the dielectric strength and reliability of the BST thin films and to prevent the problem of shorting of majority of the varactors tested. Additionally interface issues in the fabricated MIM structures affected the performance of the devices measured. These interface issues will be further discussed in Chapter 4.

Table 3.1: The deposition conditions used for sputtering BST thin films in [91].

Deposition Parameters	Values
Substrate Temperature	650°C
RF power	150 W
Total pressure	25 mTorr
Ar/O_2 ratio	90/10 sccm
BST thickness	75 nm
Deposition time	4 hours
Growth rate	17-19 nm/hour

The deposition conditions were optimized to prevent the shorting problem of the varactors. The aim was to increase the thickness of the BST layer without affecting the quality of the films that were deposited earlier. The increase in thickness would prevent the shorting of the devices due to the hillocking problem associated with Pt electrodes. Further discussion on the hillocking is provided in Chapter 4.

Since high temperature depositions in oxidizing conditions adversely affect the stability of the interfaces between the substrate, bottom electrode and BST it is important to keep the temperature as low as possible. Therefore the substrate temperature was reduced from 650ºC to 600ºC below which crystalline BST films could not be obtained [91].

The thickness of the deposited BST thin films were increased from 75 nm to around 100 nm by increasing the RF power from 150 W to 200 W and reducing the deposition pressure from 25 mTorr to 20 mTorr. The reason for increasing the growth rate by increasing the RF power and decreasing the deposition pressure is that growth rate affects the quality factor of the films deposited. It has been found that the losses in the deposited film reduce with increased growth rates [15]. But too much increase in RF power could lead to formation of defective crystals in the film during growth due to heavy bombardment [59]. The new deposition conditions are tabulated in Table 3.2.

Table 3.2: The optimized deposition conditions used for sputtering BST thin films.

Deposition Parameters	Values
Substrate Temperature	600°C
RF power	200 W
Total pressure	20 mTorr
Ar/O_2 ratio	90/10 sccm
Deposition time	4 hours
Growth rate	23-25 nm/hour

BST thin films deposited on a platinum thin film are polycrystalline in nature [87]. The characteristic X-Ray diffraction pattern obtained for BST thin films deposited on platinum in this research work is shown in Figure 3.6. Typically BST thin films deposited on platinum display highest intensity in the (110) direction [84]. The BST (100) peak is preferable as that would mean an epitaxial BST thin film growth. The change in deposition conditions did not cause any discernable change in the structural properties of the deposited BST thin films.

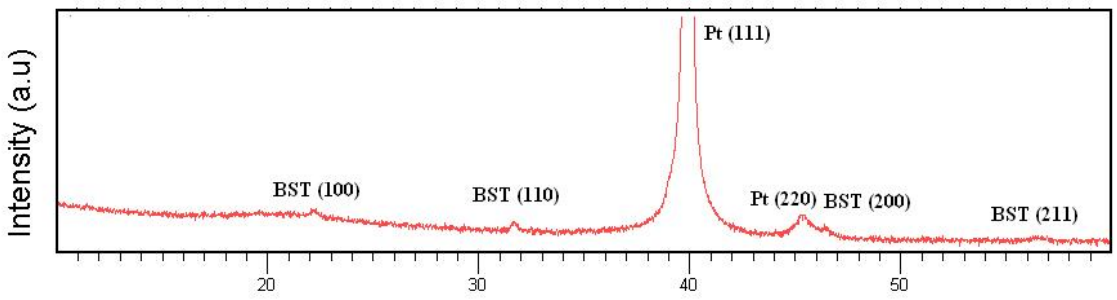

Figure 3.6: Characteristic X-ray diffraction pattern of BST thin films deposited on platinum thin film.

The deposited BST films displayed a dense microstructure with a large distribution of small grains as shown in Atomic Force Microscope (AFM) image shown in Figure 3.7. The grain sizes of the deposited BST films varied from 30-50 nm (calculated using Scherer's formula). The presence of small grains can lower the dielectric permittivity of the film because it means there is a huge distribution of grain boundaries. The high density of grains has its advantages too in that it ensures better cell-to-cell reproducibility. Large distribution of small grains is attractive in other ways too: fine-grained ceramic perovskite oxides have lower electrical conductivities than do single crystals of the same substances, due to the inter-grain depletion regions. Low electrical conductivities mean low leakage currents and high breakdown voltages [69, 96]. The inverse relation that exists between dielectric

constant and dielectric strength of many dielectrics including BST is shown in Figure 3.8 [56]. The electrical characterization of BST thin films is discussed in Chapter 5.

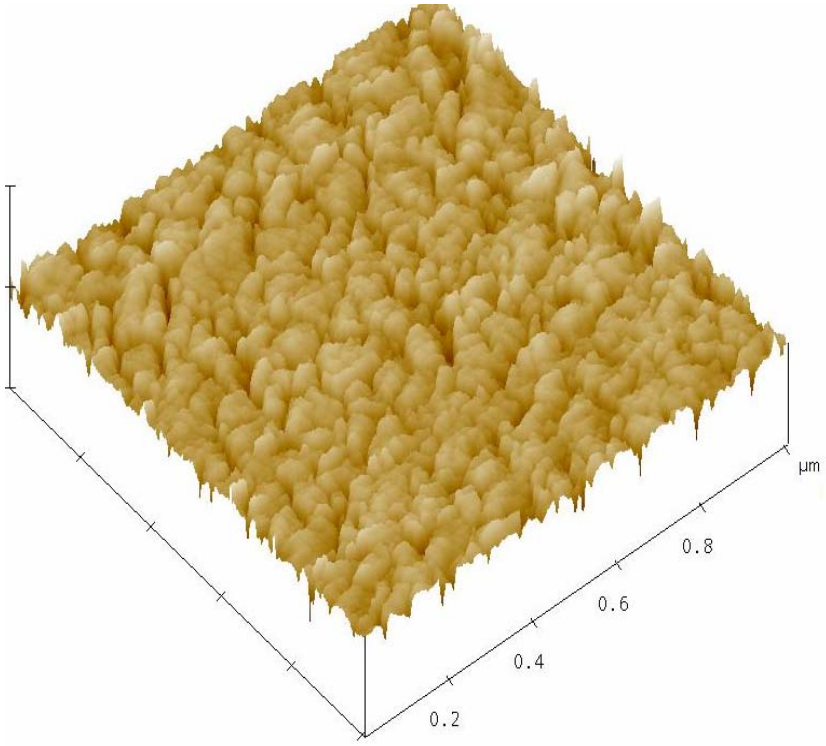

Figure 3.7: Characteristic microstructure of BST films deposited on platinum thin film.

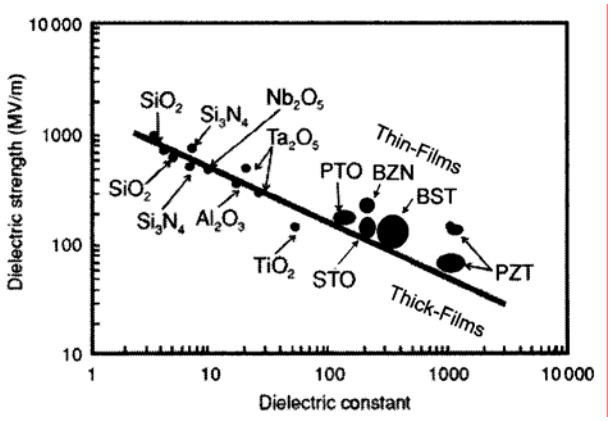

Figure 3.8: Dielectric strength versus dielectric constant for dielectrics [56].

3.4 Deposition of Nanocrystalline Diamond (NCD) Films

The Nanocrystalline Diamond (NCD) films were grown on high-resistive silicon (100) wafers in the *Cyrannus I Iplas* Microwave Plasma Enhanced Chemical Vapor Deposition (MPECVD) reactor using methane, hydrogen and argon as precursor gases. Prior to the growth, the substrates were ultrasonically seeded in a nano-diamond suspension followed by ultrasonic rinse and clean process. The surface roughness of the deposited diamond films was 10-12 nm and the grain size was found to be in the range 10-15 nm. The deposited diamond films provided a relatively smooth defect- free surface for the fabrication of devices whose active areas were much larger than the roughness and grain size values indicated above. The *Cyrannus I Iplas* reactor is shown in Figure 3.9.

Figure 3.9: The *Cyrannus I Iplas* system used for deposition of NCD films.

The deposition conditions and the percentage of precursor gases used for the CVD process are summarized in Table 3.3. Prior to the deposition, the substrates were ultrasonically seeded in a nano-diamond suspension followed by ultrasonic rinse and clean process. The nanocrystlline nature of the deposited diamond films was conformed by employing Micro-Raman spectroscopy.

Table 3.3: Deposition parameters for NCD films.

Deposition Parameters	Values
CH_4(% volume)	0.5
H_2(%volume)	1
Ar (%volume)	98.5
Microwave Power(kW)	1.8
Pressure(Torr)	135
Substrate Temperature(°C)	725

BST films were then deposited on platinized silicon (Pt/Ti/SiO_2/Si) and platinized NCD (Pt/NCD/Si) wafers at the same time to compare the structural and electrical properties of the MIM structures fabricated on SiO_2 and NCD films. The XRD and AFM results are shown in Figures 3.10 and 3.11. The XRD plots are shown from 10º to 37º and from 43º to 60º to avoid the Pt (111) peak.

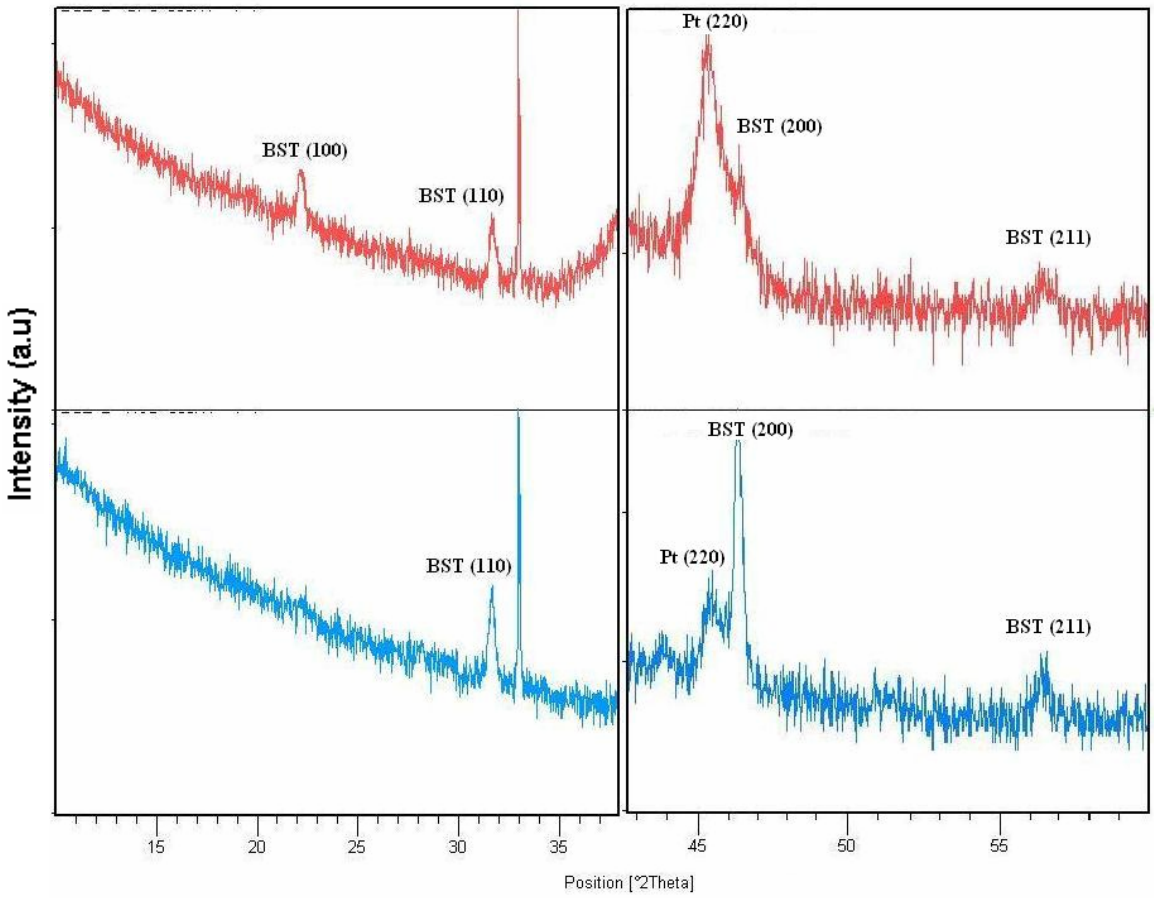

Figure 3.10: Comparison of X-ray diffraction patterns for BST films deposited on (a) platinized silicon and, (b) platinized NCD.

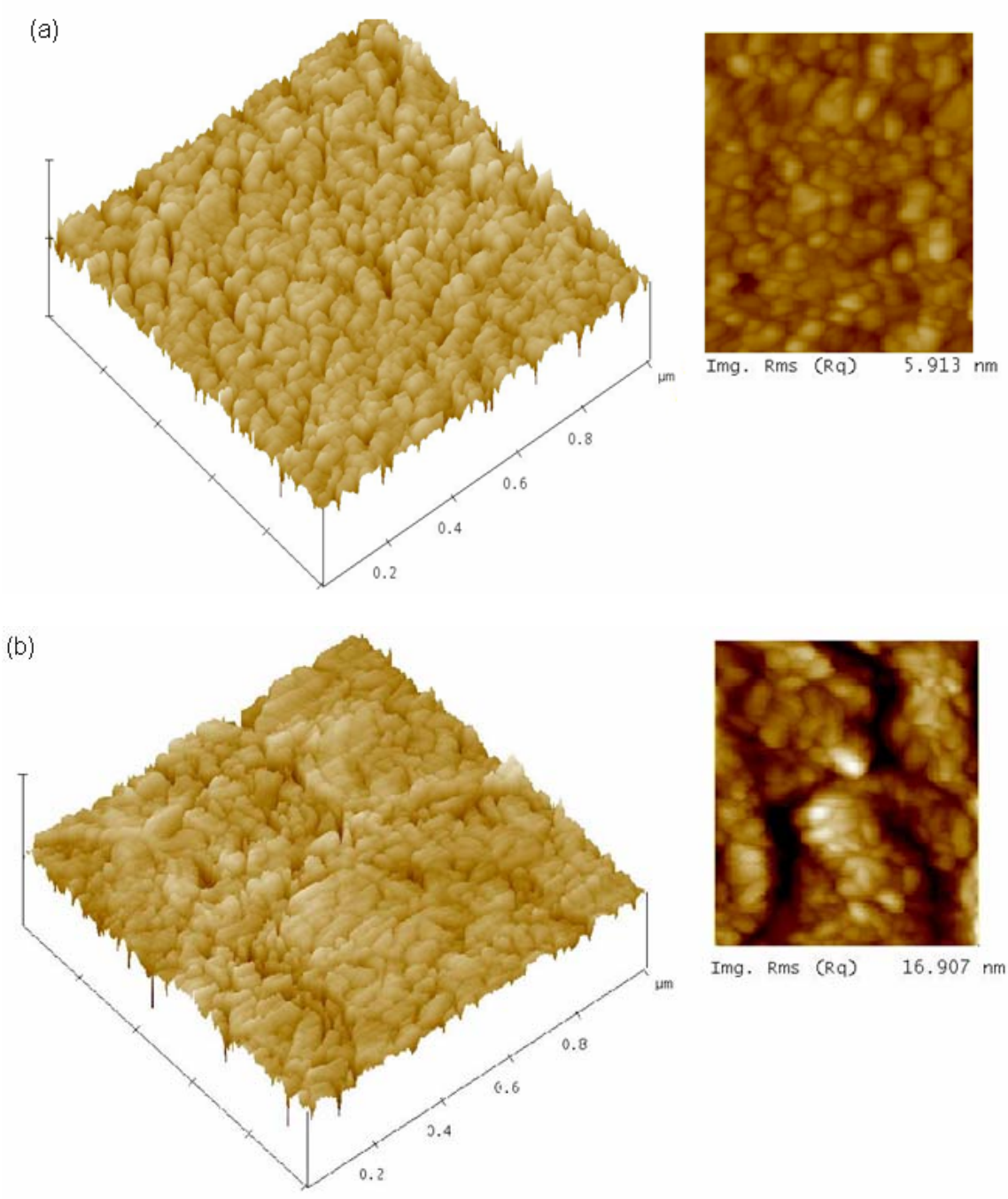

Figure 3.11: Comparison of microstructure and surface roughness for BST films deposited on (a) platinized silicon and, (b) platinized NCD.

The BST (100) peak that appeared for the film deposited on platinized silicon did not appear for the film deposited on platinized diamond. Otherwise the films on both the wafers were of polycrystalline nature. There was a large difference in the surface roughness of the deposited films due to the relatively high surface roughness of the NCD layer. The microstructure of the BST film deposited on platinized diamond was not as consistent as the BST film on platinized silicon. Huge defects were seen on some areas of the sample as seen in Figure 3.11 (b).

3.5 Fabrication of BST Metal Insulator Metal Structures

MIM structures are used in this research work to evaluate the dielectric properties of BST at frequencies ranging from 40 MHz to 1.5GHz. The tuning capacity of the structure is directly proportional to the tuning capacity of the BST thin film as the electric fields are effectively confined between the top and bottom electrode. The direct relation between relative dielectric permittivity and the measured capacitance from MIM structures makes analysis simpler. The active device areas of the devices used vary from 2500 μm^2 to 30000 μm^2 and hence large capacitance values obtained from these devices (>45pF). Fabrication of the MIM structure is a two step process with the use of a blanket bottom electrode layer. The first step involves etching the BST layer and the second step is the top metal deposition and lift-off. The measurements obtained from these devices enabled an accurate analysis of the dependence of electrical properties of BST on the deposition parameters and device interfaces. Modeling and analysis of the performance of these devices also provided important information about the important issues to be kept in mind while developing advanced BST based device architectures. The quality factors of the devices measured decrease sharply with increase in frequency due to resistive losses. For obtaining good

quality factors at higher frequencies an optimal device architecture design and fabrication process is necessary.

Prior to deposition of platinum bottom electrode, a SiO_2 layer was thermally grown on the silicon substrate followed by deposition of the Ti adhesion layer by sputtering at room temperature. For the NCD based MIM structure, a diamond film with thickness identical to the SiO_2 layer is deposited on silicon using the MPECVD method. 150 nm of platinum is then sputtered on both wafers at room temperature.

BST was then deposited on the wafers at the same time using the deposition conditions described previously. The BST layer was then etched using Buffered Oxide Etchant (BOE) 10:1 after patterning the BST layer using conventional optical lithography techniques. The etching process must be carefully timed to ensure the platinum layer does not get affected by the etchant. Over-etching creates "spots" on the platinum layer. The etch rate of BST on BOE is 16 nm/min.

After etching the BST layer, the wafer is patterned for top metal lift-off. The top metal (gold) is then deposited using thermal evaporation after depositing a thin layer of chromium adhesion layer. Acetone is used to lift-off the top metal to get the final device structures in CPW configuration for high frequency measurements. The schematic of the mask used in the second step of the fabrication is shown in Figure 3.12 with device numbers and the corresponding active areas. The device fabrication process flow after BST deposition is summarized in Figure 3.13 (a). A schematic of the top view of the final device structure along with a fabricated device is shown in Figure 3.13 (b). The cross-sectional view of the final devices in CPW configuration is shown in Figure 3.14.

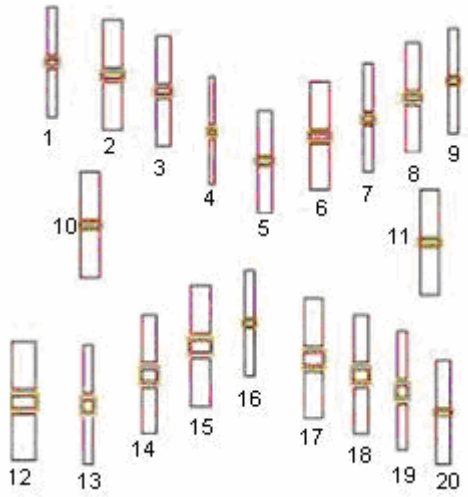

Device#	Active area (μm^2)
1, 7, 9, 13, 16, 19	5000
2, 6, 10, 11	10000
3, 5, 8, 20	7500
4	2500
12	30000
14	18000
15, 17	24000
18	6000

Figure 3.12: Mask pattern and active device areas used for used for fabrication of BST MIM structures.

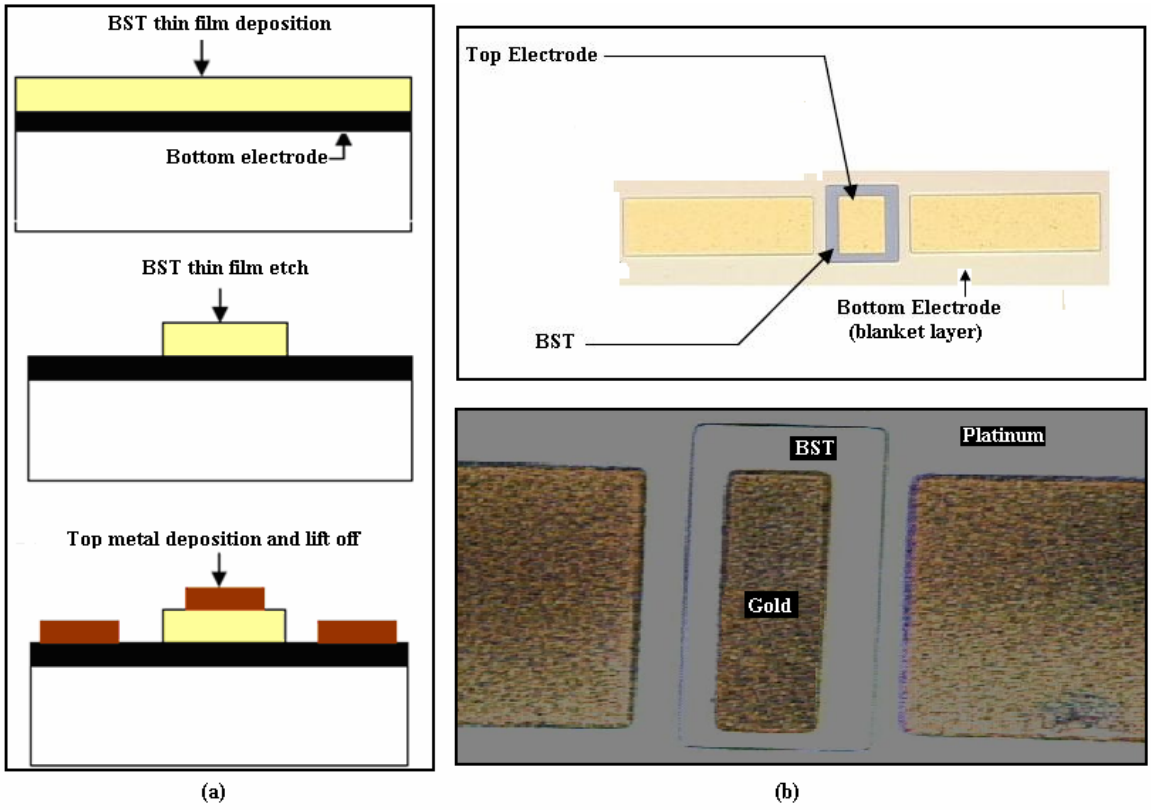

Figure 3.13: (a) Fabrication process flow of BST MIM structure. (b) Schematic of the top view of the device and photograph of a fabricated device.

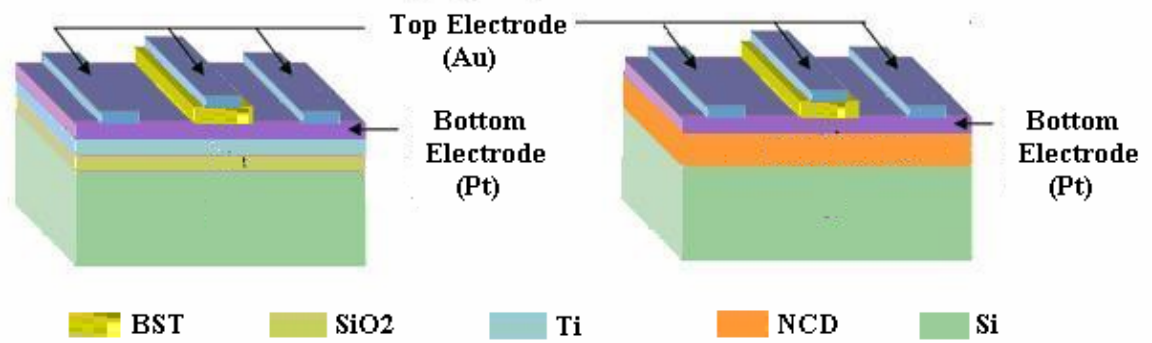

Figure 3.14: Cross-sectional view of the SiO_2 and NCD based MIM structures in CPW configuration (not to scale).

CHAPTER 4:

INTERDIFFUSION

4.1 Interdiffusion in Thin Films

Mass-transport phenomena have a distinct influence on thin film formation, properties and performance. It leads to instabilities in the functioning of components and devices due to effects like decrease in conductivity, short or open circuiting of conductors, lack of adhesion and generation of stress. Such problems frequently surface when two adjacent layers of materials are chemically reactive. The mass-transport phenomena are aided largely by lattice sites that are unoccupied, interstitial or on the surfaces which result from marginal properties of materials. In polycrystalline thin films, a large proportion of atomic-defect combinations are associated with non-lattice sites like grain boundaries, dislocations, surfaces and interfaces relative to lattice sites. This is because the loosely bound atoms at these non-lattice sites attract different point-defect populations and are more mobile than lattice atoms. A more important reason for high diffusivity through non-lattice sites is their low activation energies. Therefore they act as diffusion paths that short circuit the lattice. Grain boundary diffusion is believed to account for major amount of mass transportation. In thin films with small grains the high density of boundaries allows rapid and widespread diffusion leading to serious reliability problems.

Another important mass-transport phenomenon to be considered is electromigration which is the migration of metal atoms along metals carrying large current densities. In thin films the heat generated due to high current densities are conducted away to an extent by the

substrate which acts as a massive heat sink. In thin films electromigration manifests itself by void and hillock formation, cracked dielectric film overlayers and grain boundary grooving. This leads to film damage either due to accumulation or depletion of atoms.

Film damage is caused by either accumulation or depletion of atoms which depends on whether the major mass transport is structurally induced or induced by a temperature gradient. If more atoms enter a region such a junction of grains than leave it, a mass pileup or formation of hillocks is expected. Voids are formed when mass depletion occurs. To prevent these defects a uniform grain distribution is desired.

In device structures electromigration frequently occurs in the presence of a temperature gradient that develops at locations of poor film adhesion, in regions of different thermal conductivity such as metal-dielectric contacts. Figure 4.1 shows how hillocks and voids occur in thin films due to mass transport that in turn arises due to the grain structure and temperature variations[27].

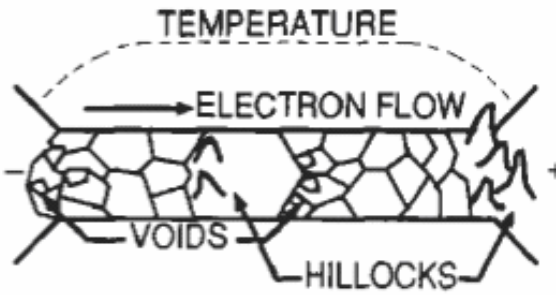

Figure 4.1: Model showing electromigration related mass-transport arising due to non-uniform grain structure and temperature gradients [27].

4.2 Interdiffusion Effects in Pt/Ti/SiO_2/Si Structure

Since BST depositions are usually done at high temperatures in the presence of oxygen both the structural defects in the different layers and the temperature gradients that exist at different locations contribute to interdiffusions between different layers which lead to formation of defects in the Pt/Ti/SiO_2 layers which are extremely detrimental to the performance of the devices.

The Si/SiO_2 layer undergoes decomposition at high temperatures in the presence of oxygen due to contamination from metals like Ti and Pt. The surface defects in the Si/SiO_2 act as nucleation sites for void formation when the deposited metals getter at these defects leading to decomposition of the oxide layer. Metals can form precipitates, generate dislocations, or enhance the roughness of the Si/SiO_2 interface [17, 97].

The Ti layer is deposited to act as an adhesion layer and also to prevent the formation of platinum silicide at high temperatures[98]. A cross-sectional image of SiO_2, Ti and Pt layers on a Si wafer used in this research work is shown in Figure 4.2. The layer marked '1' is the

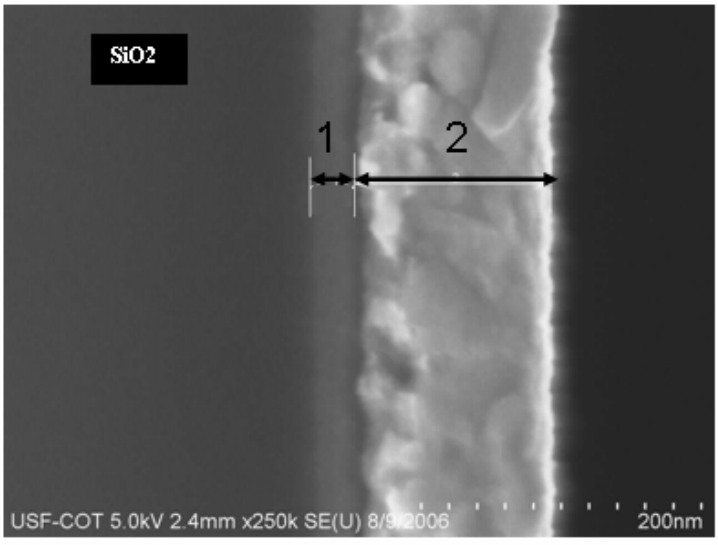

Figure 4.2: Silicon dioxide, titanium and platinum layers on Si (100) wafer.

Ti layer and the layer marked '2' is the Pt layer. Both the layers were sputtered at room temperature and hence show no defects due to interdiffusion.

At high temperatures in oxygen ambient, Ti diffuses and oxidizes in the Pt layer which leads to hillock formation in the platinum layer which degrades the performance of ferroelectric devices and increases the probability of device shorting. The formation of hillocks in Pt-Ti electrodes has been widely reported[18-22]. Hillocks are believed to result from the volume expansion in the Pt layer due to the formation of TiO_2 in the Pt layer. This volume expansion gives rise to the compressive stress of the Pt layer, which is believed to be the cause for the formation of the hillocks. It is also important to note that the shorting of capacitors is more due to the size of the hillocks than the distribution of hillocks. The size and distribution of the hillocks depend on the thicknesses of Ti and Pt layers and the amount of oxygen used during the deposition of BST [20]. The use of TiO_2 as the adhesion layer instead of Ti also poses adhesion issues which leads to process-induced delamination of the Pt layer [18, 99].

In this research work, 150 nm of Pt and 40 nm of Ti are used and 100 nm of BST is deposited with a very low oxygen flow of 2.5 sccm to make sure the hillocks formed do not result in shorting of the capacitors. The electrical shorting probability of the resulting MIM structures decreased dramatically. The decrease in shorting probability can be attributed to the thicknesses of the Ti, Pt and BST layers used in these devices and the low oxygen flow during deposition which considerably reduced the effect of hillocks in the device performance. A cross-sectional SEM image of the SiO_2/Ti/Pt/BST layers is shown in Figure 4.3. The interdiffusion of Ti into Pt layer and the resulting volume expansion related defects can be seen. The voids that are observed could trap the charged carriers that flow from the

platinum electrode when bias is applied across the dielectric. These trapped charges could increase the relaxation time of BST when the bias is reduced abruptly which could distort the Capacitance-Voltage (CV) behavior of the varactors. The CV behavior of varactors fabricated on Pt/Ti/SiO_2/Si wafers is discussed in Chapter 5.

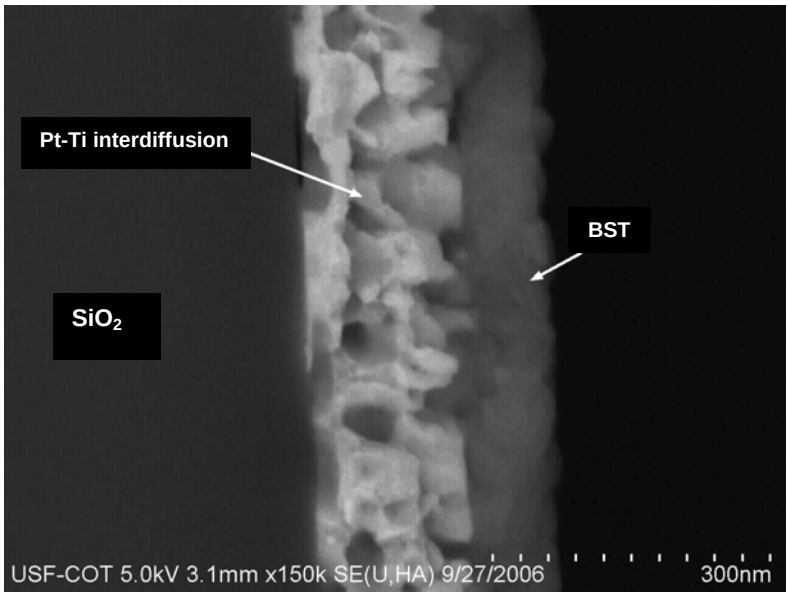

Figure 4.3: Interdiffusion between the platinum and titanium layers after BST deposition.

Thus SiO_2/Ti/Pt/BST and SiO_2/TiO_2/Pt/BST based MIM structures suffer from severe interdiffusion and delamination problems which affects the reliability and yield of the resulting devices. Ali Tombak et al. [23] have reported that above 300MHz electrode losses play a principal role in degrading the quality factor of BST thin film capacitors. Therefore it is very important to obtain a stable defect free platinum bottom electrode layer to achieve superior device performance. Platinum deposited on Sapphire substrate at high temperatures has been employed for BST based varactor fabrication [15].

In this research work the performance of MIM structures using Nanocrystalline Diamond (NCD) films deposited on silicon as the diffusion barrier layer were investigated. In these structures no adhesion layers were used between the NCD layer and the platinum layer.

4.3 NCD/Pt/BST Structure

Chemical Vapor Deposited (CVD) diamond would make an excellent material for high frequency applications and prior research work has shown that diamond films deposited on high-resistive silicon substrate displayed very low RF losses comparable with the performance of thermally grown SiO_2 on high-resistive silicon substrate from DC-65GHz [24]. Very stable electrodes can be obtained by depositing metals on diamond films as they are chemically inert and highly corrosion resistant [26]. Diamond also has the highest thermal conductivity among all materials which means that it can act as an effective heat sink that can reduce the detrimental effects that the electromigration phenomenon has on the metal layers [25]. Thus it exhibits excellent properties for application as a stable diffusion barrier layer for ferroelectric thin film-based MIM devices.

A cross-sectional SEM image of the NCD/Pt/BST layers deposited on Si (100) is shown in Figure 4.4. As seen from the image clear and stable interfaces exist between all the layers. The one disadvantage with using diamond films is that the surface roughness of the diamond films is relatively higher than SiO_2. But for initial performance analysis, devices with large active areas were used to circumvent the roughness effects.

To further ascertain the quality of the interfaces in the NCD/Pt/BST X-Ray Mapping (XRM) was done. X-ray mapping of elemental distributions, first demonstrated by Cosslett and Duncumb in 1956, has become one of the most popular modes of operation for exploring chemically heterogeneous microstructures with electron beam microanalysis. XRM is a slow technique taking many hours of SEM time [100]. Therefore the sample was analyzed overnight to obtain high resolution x-ray maps with good statistics at low levels of concentration.

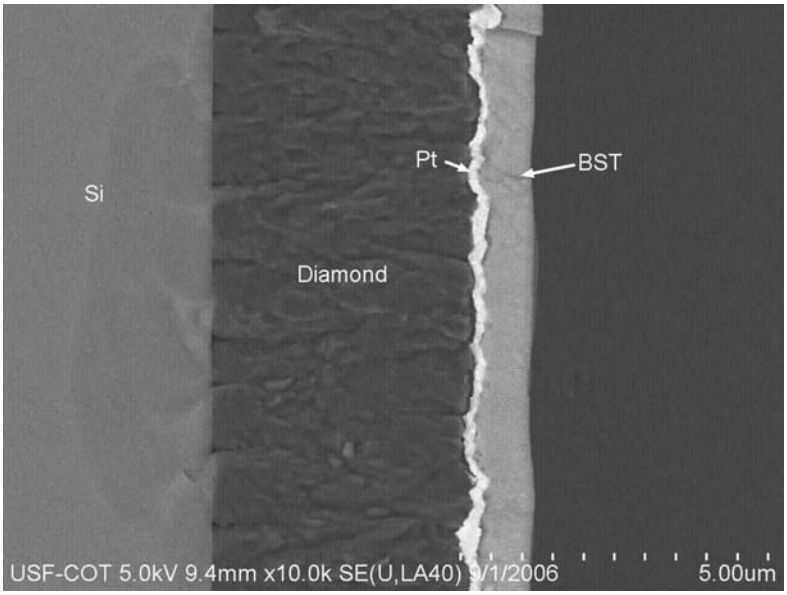

Figure 4.4: Nanocrystalline diamond, platinum and BST layers on Si (100) wafer.

Area of the sample used for analysis is shown in Figure 4.5. The X-Ray maps obtained for NCD, Pt, Ti (in the BST layer) and Si layers are shown in Figures 4.6-4.9.

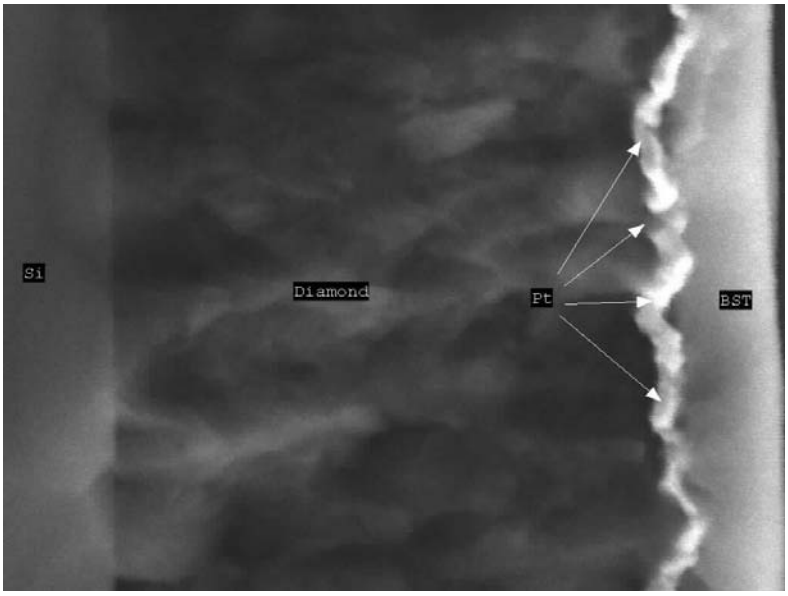

Figure 4.5: Area of the sample used for X-ray mapping.

Figure 4.6: Silicon X-Ray Map.

Figure 4.7: NCD X-Ray Map.

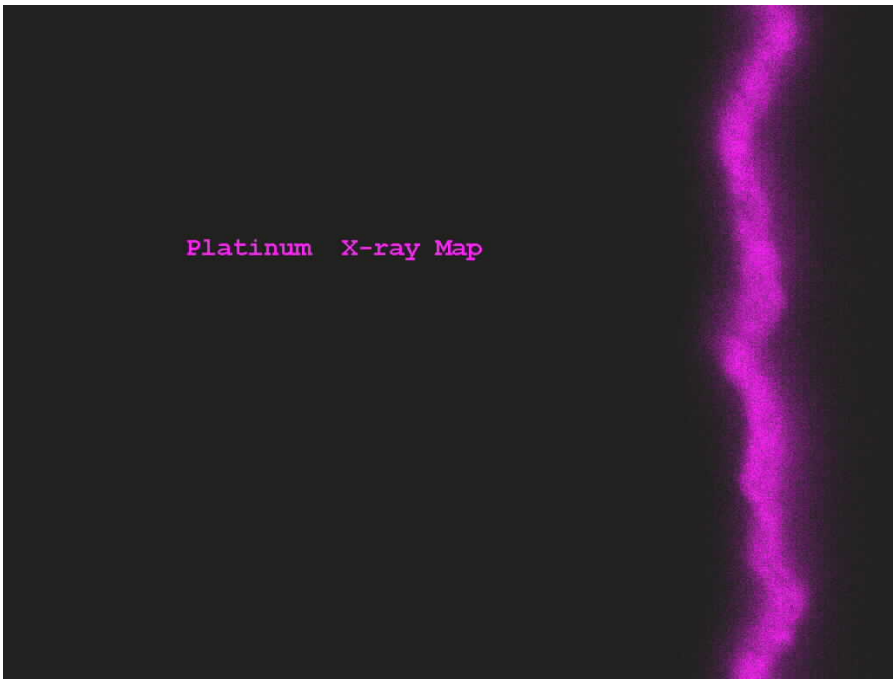

Figure 4.8: Platinum X-Ray Map.

Figure 4.9: Titanium X-Ray Map.

From the X-Ray Maps obtained it can be seen that there is no interdiffusion between any of the layers. There are no signs of the platinum layer diffusing into either the NCD, silicon or BST layers. There are also no signs of out-diffusion of titanium in the BST layer into the platinum layer. Therefore it can be concluded that using NCD as the diffusion barrier layer provides stable interfaces for BST based MIM structures. The CV behavior of the varactors fabricated on NCD is discussed in Chapter 5.

S-parameter measurements were done to measure the variation of resistance of the platinum film on NCD and SiO_2 layers from 40 MHz to 1.2 GHz. It was found that the platinum film on NCD displayed less resistive losses than the one on SiO_2 which indicates lesser mass transport along the platinum layer and a reduced contribution to device losses [27]. Figure 4.10 shows the variation of real part of impedance (resistance) with frequency for the Pt film on NCD and SiO_2 diffusion barrier layers respectively.

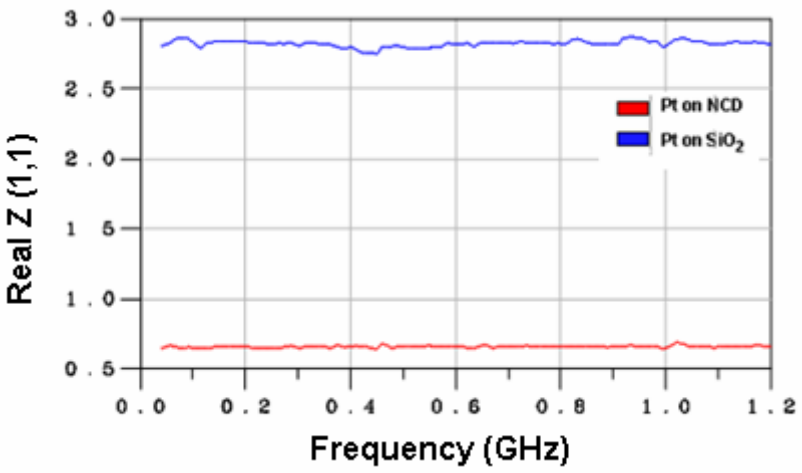

Figure 4.10: Variation of resistance with frequency for platinum film on NCD and SiO_2 diffusion barrier layers.

CHAPTER 5

VARACTOR MEASUREMENTS

5.1 Measurement Setup and Equivalent Circuit Model

One port S-parameter measurements were conducted on the fabricated BST varactors using the Anritsu 39397C Lightning Vector Network Analyzer (VNA) and the DC biasing was done using Agilent E3620A DC bias supply. Short-Open-Load calibration was done using the CS-5 calibration substrate. The measured device data was extracted and modeled using Agilent Advanced Design System 2004A (ADS). Varactor performance analysis was done using the model prescribed for BST based shunt varactors [23].The equivalent circuit used to model the device performance is shown in Figure 5.1.

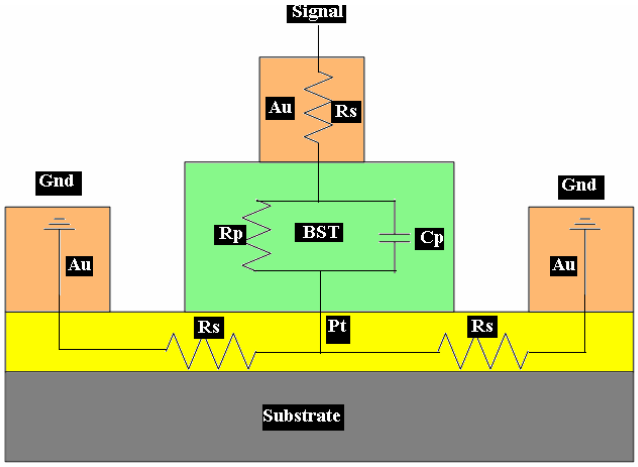

Figure 5.1: Equivalent circuit model used to characterize varactor performance [23].

In the device model used the series resistance R_s represents the electrode losses, R_p accounts for the dielectric losses and C_p is the shunt capacitance measured from the devices. The variation of capacitance with temperature for the BST varactors were measured using the semi-automatic Cascade probe station equipped with a cryogenic temperature controlled chuck.

The equivalent circuit models elemental values were optimized such that the measured and modeled S11 values fit over a frequencies ranging from 100 MHz to 1 GHz. The relative permittivity (ε_r), the loss tangent of BST (tanδ) and the quality factors of the device were extracted from the model using the relations given below-

$$\varepsilon_r = \frac{C_p.d}{\varepsilon_0.A} \tag{5.1}$$

$$\tan\delta = \frac{1}{\omega R_p C_p} \tag{5.2}$$

$$Q_{BST} = \omega R_p C_p = \frac{1}{\tan\delta} \tag{5.3}$$

$$Q_{electrode} = \frac{1}{\omega R_s C_p} \tag{5.4}$$

$$Q_{total} = \frac{1}{Q_{BST}} + \frac{1}{Q_{electrode}} \tag{5.5}$$

, where d is the thickness of the deposited BST and A is the active area of the fabricated devices. Q_{BST}, $Q_{electrode}$ and Q_{total} are the quality factors of BST, the electrodes and the total quality factor of the measured varactor respectively.

5.2 Variation of Capacitance with Electric Field

The variation of capacitance with external bias was studied for varactors fabricated on SiO_2 and NCD. The bias voltage was increased to 5V (0.5MV/cm) and the capacitance value was calculated at 100MHz for every 0.5V interval. Then the voltage was brought down to zero abruptly and subsequently increased in the reverse bias region in 0.5V increments up to -5V. Figure 5.2 shows the CV curve obtained for Device#6 (Active area -10000μm^2) fabricated on SiO_2 (For device number and device list refer to Figure 3.12 in page 61).

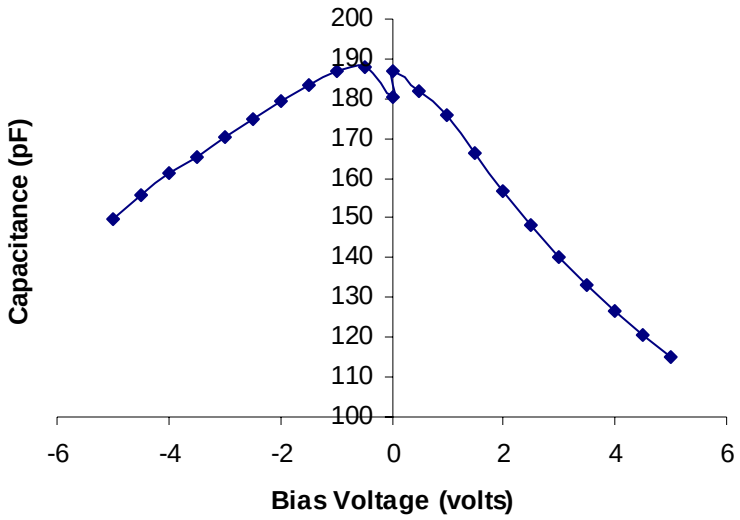

Figure 5.2: Capacitance-voltage behavior of varactor fabricated on SiO_2.

From the calculated capacitance values it was found that there was a striking variation in the zero-bias capacitance values before and after the application of forward bias. A distinct asymmetry was observed in the CV curve obtained. The distorted CV behavior indicates a high density of charge build-up in the BST-platinum interface and in the grain boundaries of BST. The grain boundaries of BST usually have charged oxygen vacancies and excess titanium which results in a characteristic dielectric relaxation behavior depending on the density of these charges but the distinct asymmetry observed here suggests the presence of

ionic species injected from the bottom electrode layer which get trapped in the BST-Pt interface during the forward bias operation and affect the dielectric performance in the reverse bias causing an asymmetry in varactor operation [59, 87, 101].

This was confirmed by conducting CV measurements on Device#6 again by steadily decreasing the bias voltage to 0V from 5V and -5V in 0.5V intervals instead of following the normal measurement mode of abruptly bringing down the voltage to zero. The measurements were first conducted from 5V to -5V and then from -5V to 5V. The resulting CV curves are shown in Figure 5.3.

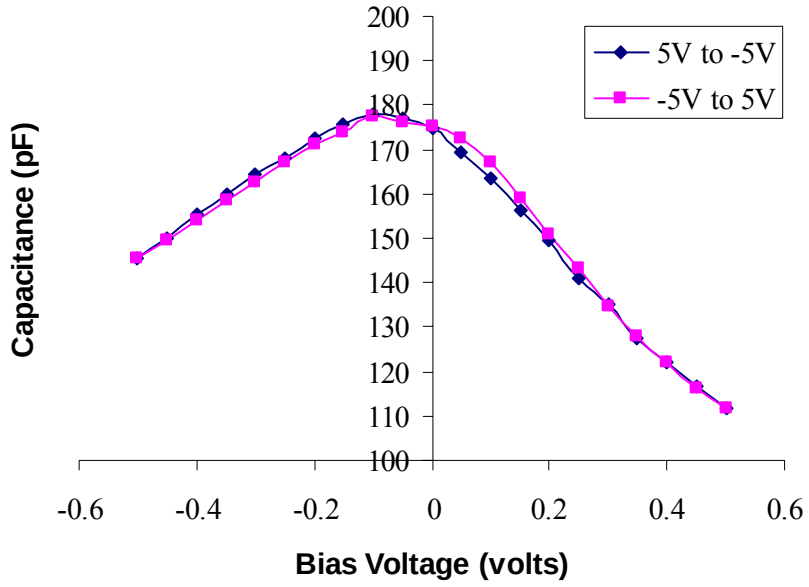

Figure 5.3: Dielectric relaxation behavior of BST films.

It can be seen that with steady decrease in bias voltage to zero reduced the variations in the zero bias capacitance values to negligible levels probably because the relaxation times of the ionic species have been accounted for due to the slow variation in bias voltage but the curves were still asymmetrical due to the detrimental effects of mass transport from the bottom electrode trapped in the voids present in the dielectric-electrode interface. The reduced tunability of capacitance in the reverse bias region compared to the forward bias

region suggests that more ionic species are getting transported and trapped in the BST-Pt interface than in the BST-Cr/Au interface.

Next, the CV behavior of varactors fabricated on NCD and SiO_2 were compared at 100 MHz. Device#3 (Active area -7500μm^2) was used for these measurements. The normal measurement mode of increasing the bias voltages in the forward region and then abruptly decreasing the voltage to zero and increasing it again in the reverse region was followed for these devices. The resulting CV curves are shown in Figure 5.4.

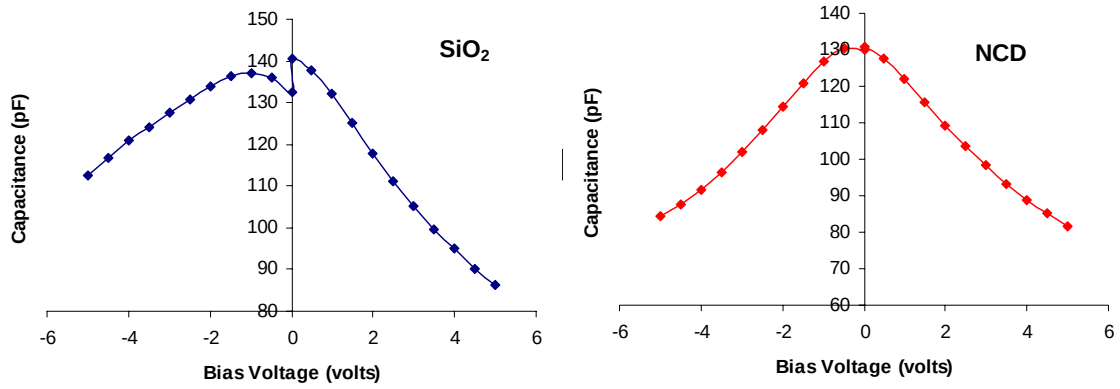

Figure 5.4: Variation of permittivity with applied bias for varactors fabricated on SiO_2 and NCD films.

It can be seen that the CV curves obtained from varactors fabricated on NCD are very symmetric. Only negligible variations in zero bias capacitance values were observed before and after bias application which are probably due to the charges present in the BST grain boundaries. This suggests that the interfaces in the NCD based MIM structures are very stable and defect free due to reduced interdiffusion between the different layers.

The reduced capacitance of the NCD varactors is due to the increased roughness of the BST surface on NCD which marginally reduces the cross-sectional area of the device. The tunability of the NCD varactor (60.4%) in the forward bias region was also marginally lower than the tunability of the SiO_2 varactor (61.9%) for the measured bias voltages. The NCD

varactors also needed an initial drive-in voltage of around 0.5V to 2V probably to evaporate the resist residues on the rough BST surface. Figure 5.5 shows the NCD varactor response before and after drive-in voltage.

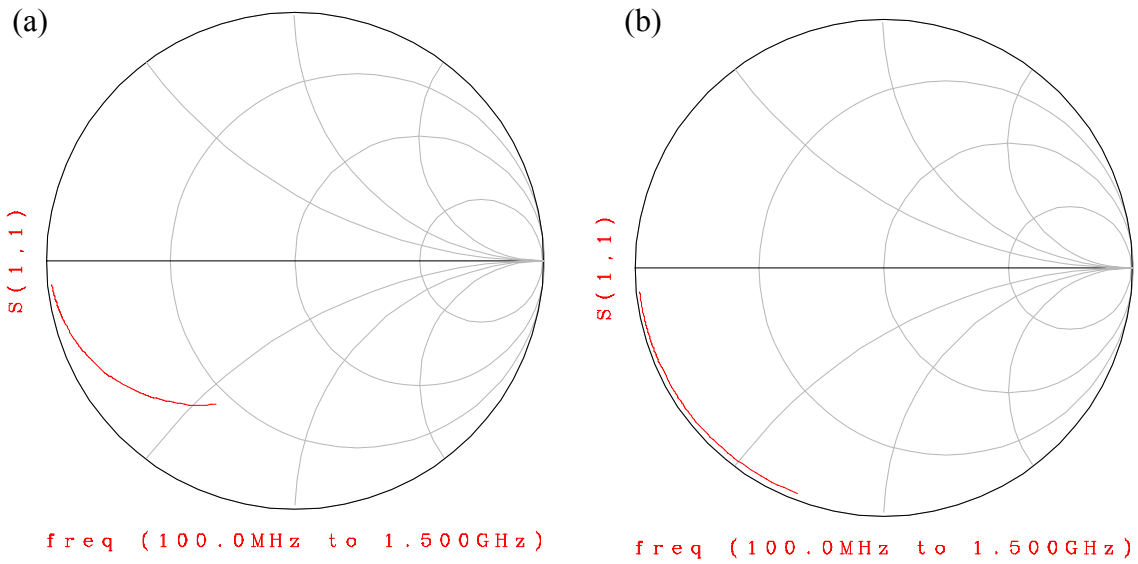

Figure 5.5: Response of NCD varactor (a) before and (b) after drive-in voltage.

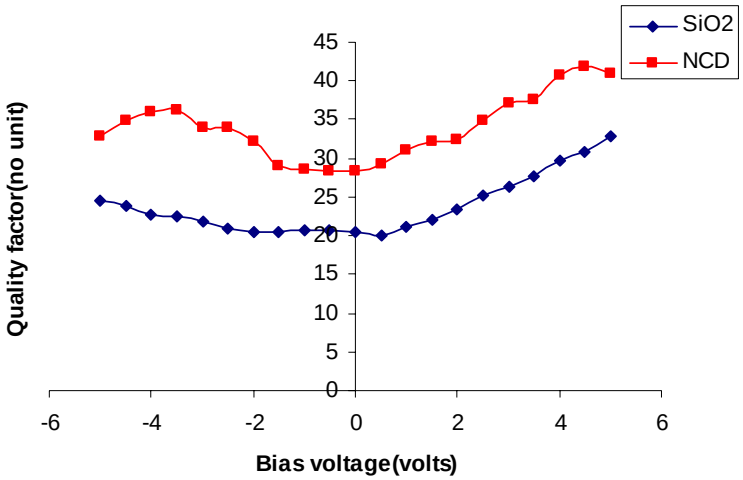

Figure 5.6: Variation of quality factors with applied bias for varactors fabricated on SiO_2 and NCD films.

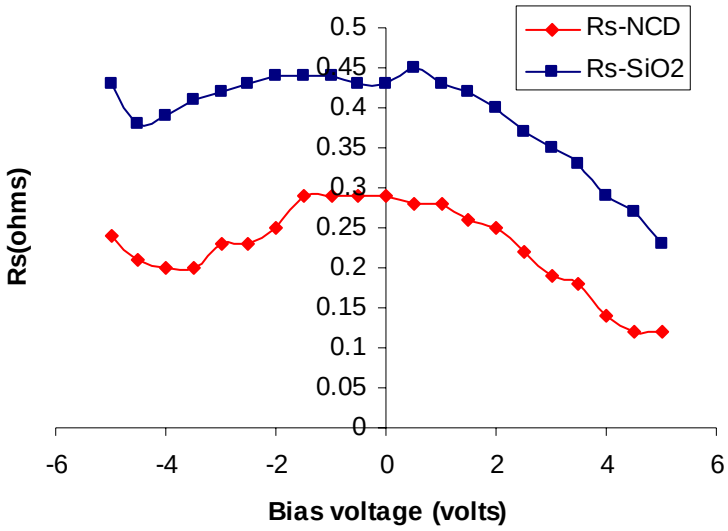

Figure 5.7: Variation of R_s with applied bias for varactors fabricated on SiO_2 and NCD films.

Next the quality factors of the NCD and SiO_2 varactors were compared. At 100MHz the quality factor of the varactors are entirely dominated by the bottom electrode losses as a dielectric relaxation behavior is observed and the dielectric losses are static at 0.01. Since the NCD varactors exhibit lower bottom electrode losses than SiO_2 varactors, the quality factors are correspondingly higher. The inverse relation that exists between the quality factor and the electrode losses (Rs) is shown in Figures 5.6 and 5.7. The performance of all the NCD and SiO_2 varactors displayed similar performance trends when measured and characterized

5.3 Variation of Capacitance with Frequency

The variation of capacitance with at frequencies ranging from 100 MHz to 1GHz for varactors fabricated on SiO_2 and NCD were calculated at different forward bias voltages (Figure 5.8). Device#3 was used for this analysis.

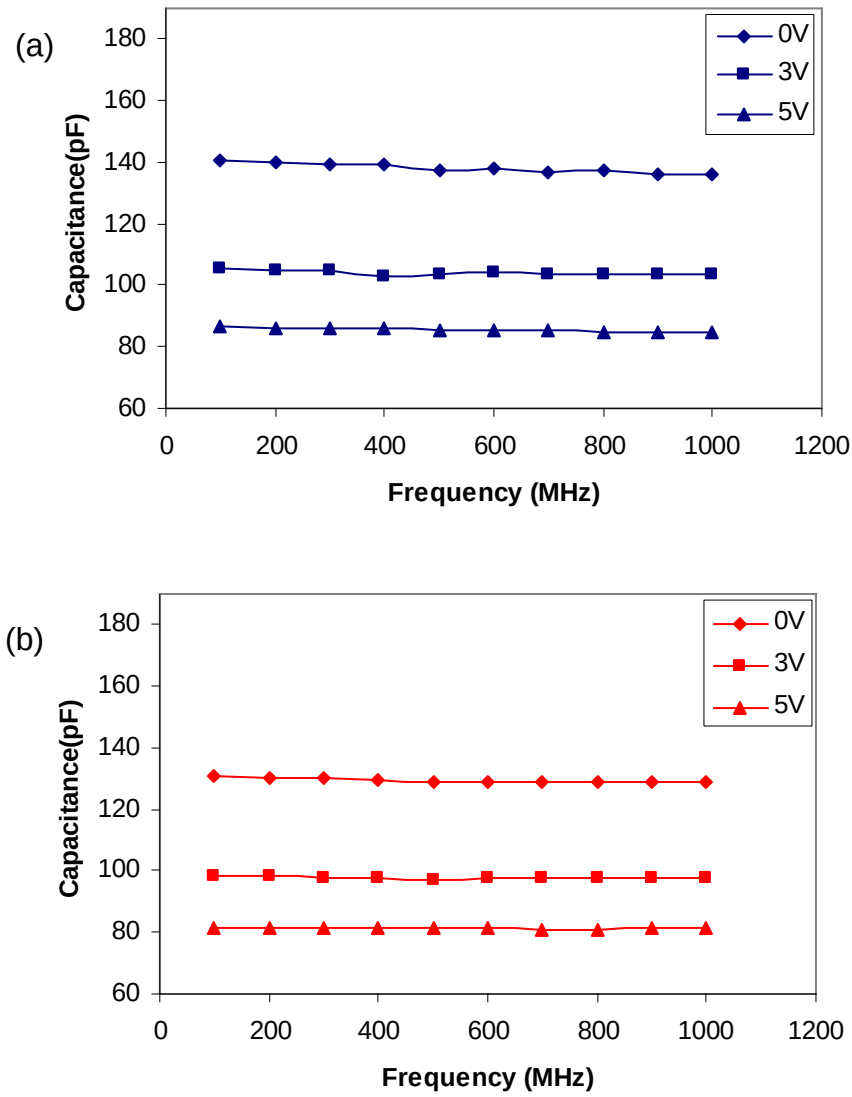

Figure 5.8: Variation of capacitance with frequency for (a) SiO_2 varactor and (b) NCD varactor at different bias voltages.

As frequency increases, the contributions from the different polarization mechanisms operating in the dielectric gets reduced and a relaxation behavior is observed in the dielectric[41]. In BST the dielectric relaxation behavior is defined by the Curie-von Schweidler power law dependence of t^{-n} (where $n<1$)[99]. The capacitance values therefore stay constant right through the measured frequency range and there is a monotonic decrease in capacitance with increase in forward bias voltage.

The quality factor and the loss tangent decrease linearly with increase in frequency. The frequency dependant loss tangent is indistinguishable from the series resistance due to the metal electrodes[56]. Therefore the electrode losses play a dominant role in determining the quality factor of the devices in the high frequency range. Again since the NCD varactors have lower electrode losses, their quality factors are better than those of SiO_2 varactors. The R_S values stay relatively constant over the entire measurement frequency range. The variation of quality factor, loss tangent and R_S with frequency is shown in Figure 5.9. Similar measurements were conducted on four other devices with different active areas and on different samples and in each case the varactors fabricated on diamond showed better performances with about 20% percent better tunability than the SiO_2 based varactors.

When the varactors were under bias, it was observed that resonant curves appear at high frequencies. This resonance behavior was observed in all the varactors measured. The depth of these resonance curves increased with applied bias. These resonance curves occur due to the electrostrictive property of BST and are detrimental to varactor operation at high frequencies [56].

Device#3 (Active area -7500 μm^2) and Device#4 (Active area -2500μm^2) were used for comparing the resonance behavior in NCD and SiO_2 varactors up to 5GHz. It was found that the resonance behavior started occurring at 3V applied bias. These curves occurred at around 1.5 GHz and 3.3 GHz for the NCD varactors irrespective of active area of the device measured. For the SiO_2 varactors the resonance behavior occurred at 2 GHz and 4GHz. This observed variation in frequencies could be due to the slight variation in cross-sectional area of the SiO_2 and NCD varactors measured due to the increased roughness in the BST layer on the NCD varactors or it could be due to the presence of the NCD layer.

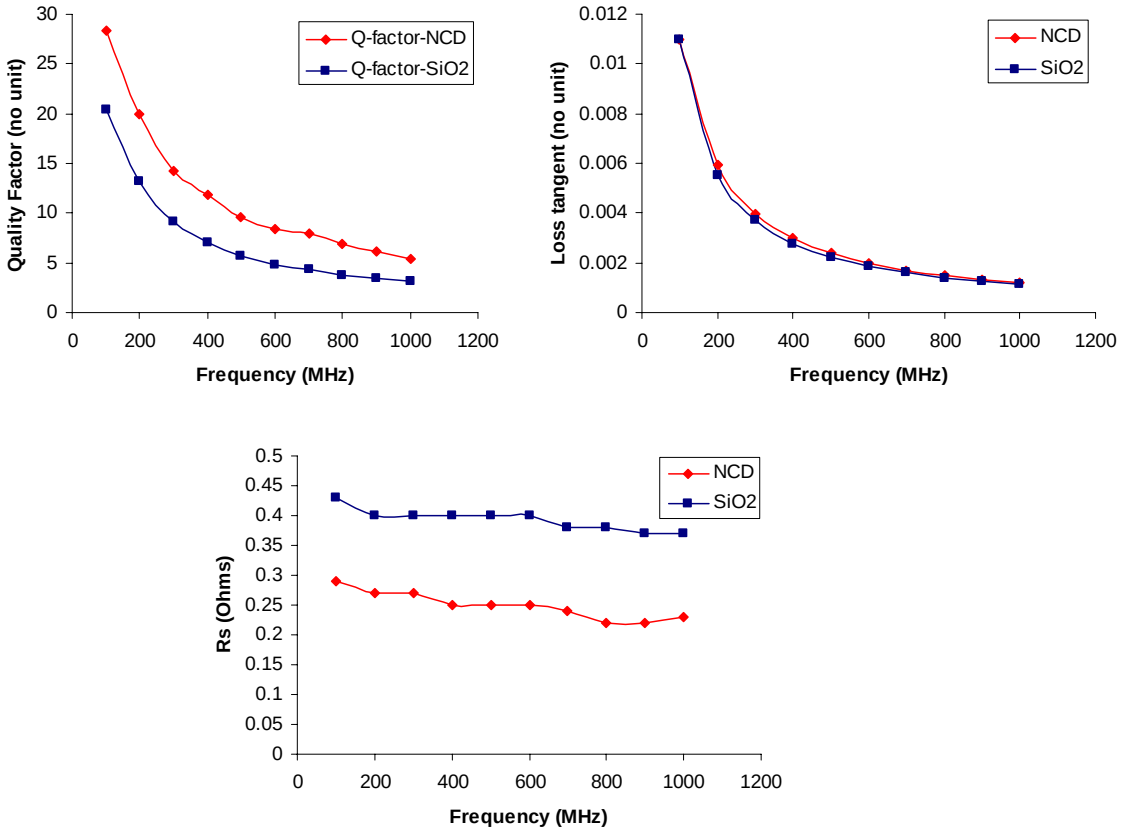

Figure 5.9: Variation of quality factor, loss tangent and R_s with frequency.

The depth of the curves decreased in Device#3 in both SiO_2 and NCD varactors when compared with the depth in Device#4 which means that the depth of the curves have a strong

dependence on the active area of the varactors. Further study is required to understand and characterize this resonance behavior. The increase in the depth of these curves with applied bias for both SiO_2 and NCD varactors is shown in Figure 5.10. The variation of the depths of these curves with device active area for both SiO_2 and NCD varactors is shown in Figure 5.11.

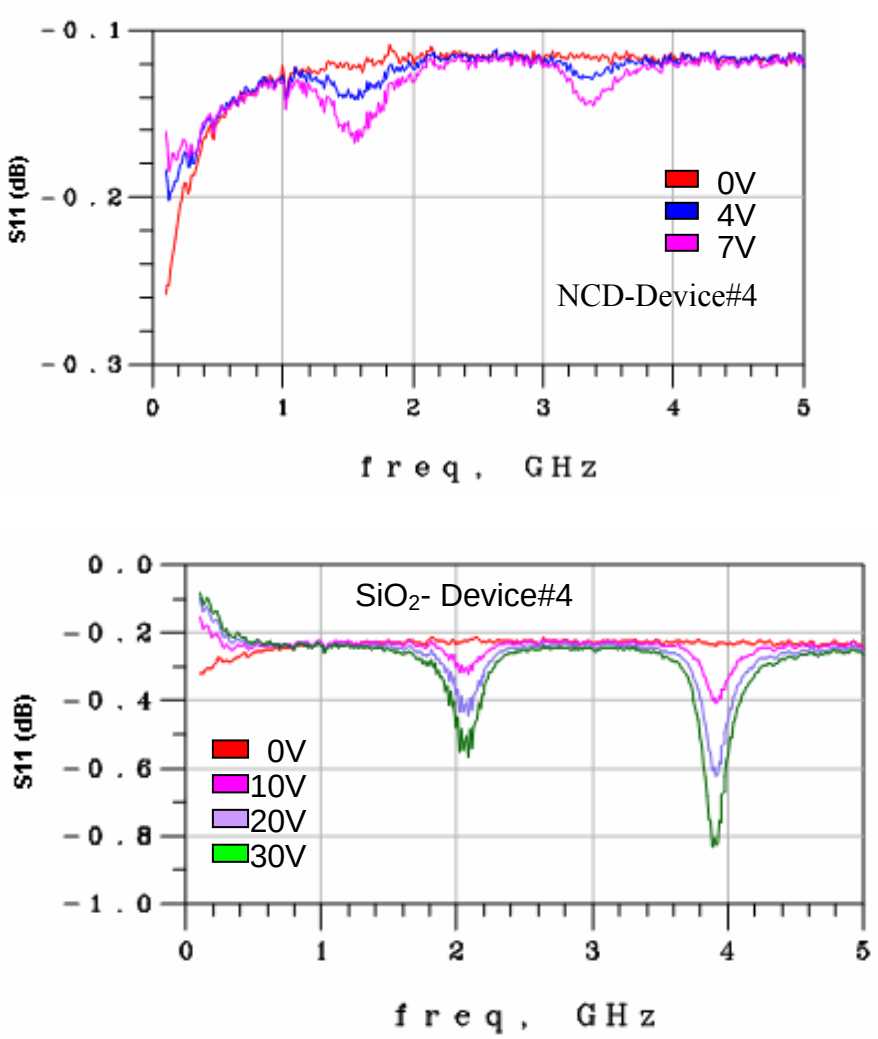

Figure 5.10: The increase in the depth of resonant curves with applied bias for SiO_2 and NCD varactors.

This electrostriction property observed in BST can potentially be used for development high-Q resonators. The resonance behavior in BST varactors has been modeled to resemble a thickness mode Bulk Acoustic Wave (BAW) device [56].

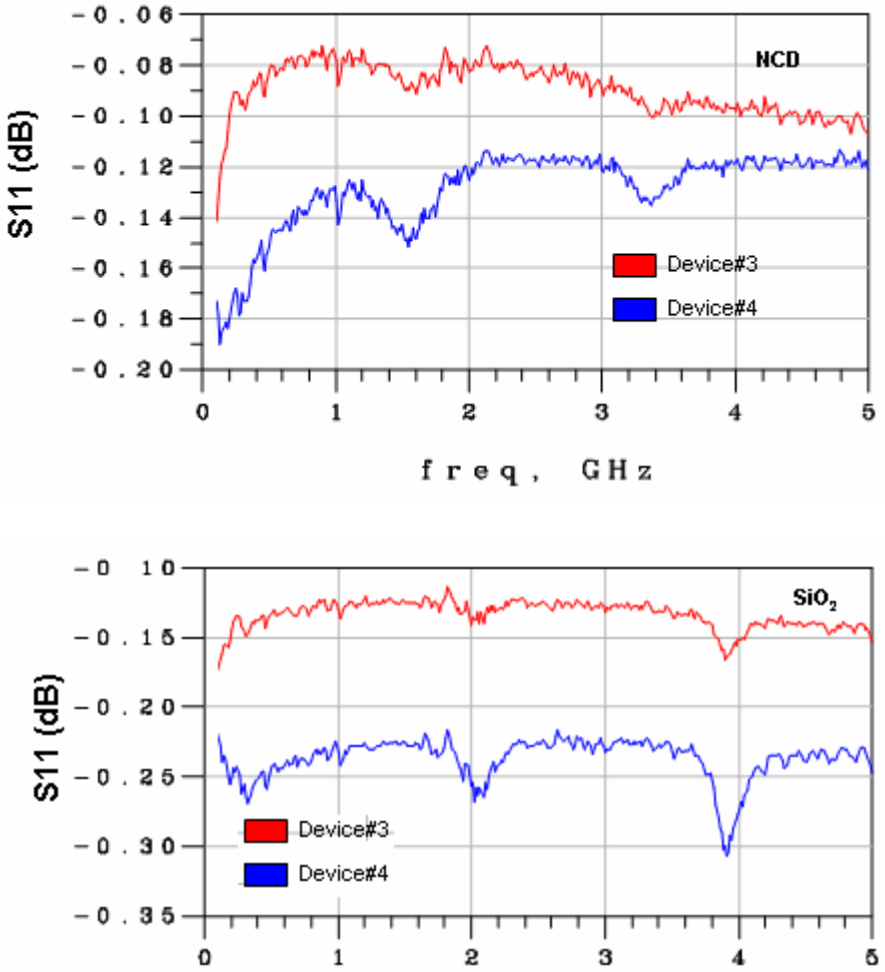

Figure 5.11: The variation of the depths of resonant curves with device active area for SiO_2 and NCD varactors.

5.4 Varactor Breakdown and Tunability

Dielectric breakdown occurs due to either one of four mechanisms namely thermal (due to ionic conduction with increase in temperature), avalanche (at high electric fields accelerated free electrons strike atoms of the material and free more electrons who in turn create more free electrons and the process continues till the material breaks down), discharge (large electric field arc across pores of the material leading to erosion and more arcing until the material breaks down) and electrolytic (conduction paths created over time due to ionic and/or environmental conditions). The breakdown mechanism in ferroelectrics is avalanche breakdown [102]. The breakdown strength of a dielectric is not related to its dielectric properties [103]. The breakdown fields are the same above and below the Curie temperature, in the ferroelectric and paraelectric phases, and have nothing to do with domains. The breakdown field depends mainly upon thickness of the dielectric layer, type of electrodes used and temperature [96]. The devices on SiO_2 broke down catastrophically as shown in Figure 5.12.

For the BST varactors fabricated on SiO_2, thicker films give higher tunabilities (at the expense of increased bias voltages) and display higher breakdown fields as indicated by Baki Acikel[15]. The performance of varactors in Sample-1 and Sample-2 was considered. The BST thickness on Sample-1 was 100 nm and the BST thickness in Sample-2 was 150 nm. A forward bias CV curve for Device#14 in Sample-2 which had a breakdown voltage >55V (>3.6MV/cm) is shown in Figure 5.13.

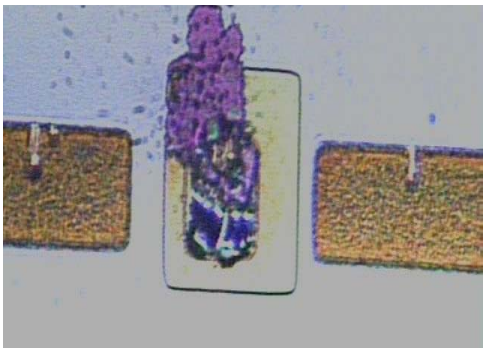

Figure 5.12: Photograph of Device#4 after breakdown.

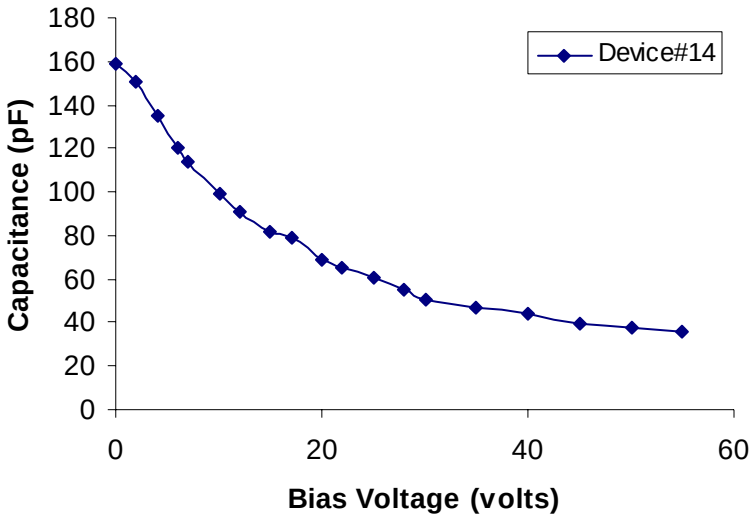

Figure 5.13: Forward bias CV curve of varactor fabricated on SiO_2 with a BST thickness of 150 nm.

As can be seen in Figure 5.13 the maximum variation in capacitance with bias is between the (0-20)V region after which there are very negligible changes in the capacitance values with applied bias. The overall tunability of this varactor was 4.5:1.

It has been suggested that both tunability and breakdown fields of BST varactors are thickness dependant and that geometry effects can be ignored for large-area MIM varactors as tunability of the varactor is directly proportional to BST's tunability[56].

Hence when the performance of varactors measured was analyzed depending on the thickness of the BST layer a clear relation between BST thickness, tunability, breakdown fields and effect of interdiffusion-induced shorting emerges which is summarized in Table 5.1. Here comparison is made between varactors measured at different thicknesses. The performance analysis of the varactor with 75 nm BST thickness was done by Sriraj Manavalan [91]. Device#4's performance in Sample-1 and Device#14's performance in Sample-2 was considered for this summary.

Table 5.1: Performance summary of varactors fabricated on SiO_2.

BST thickness (nm)	Tunability in (0-6)V range (no unit)	Breakdown voltage (volts)	Breakdown field (MV/cm)	Overall tunability (no unit)	Device shorting issues?
75*	2.8:1	6	2.1	2.8:1	Yes
100	1.75:1	>30V	>3	3.9:1	No
150	1.32:1	>55V	>3.6	4.5:1	No

*Measurement done by Sriraj Manavalan [91].

The conclusion drawn from this performance analysis is that the harmful effects of interdiffusion and delaminations prevent the tailoring of BST thickness over a wide range to suit various applications. Conversely, existence of stable interfaces would enhance the performance of the varactors and also allows the variation of BST thickness over a wide range depending upon varactor performance requirements.

The breakdown voltages for the varactors fabricated on NCD were 7-8 volts maximum irrespective of the thickness of the BST layer. The NCD varactors did not break down catastrophically and their breakdown was characterized by a sudden increase in current across the electrodes. This suggests that the breakdown in NCD varactors is induced by the

high surface roughness values of the BST layer in the NCD varactor which resulted in the creation of a breakdown path across the varactor at low bias voltages. Most of the NCD varactors also got shorted due to the inconsistency of the BST layer. The surface roughness values varied widely across the sample. However improvements were seen in the output (more devices worked) with smoother BST layers. Therefore it is extremely important to further optimize the NCD deposition process to get smoother films which consequently convert to smooth platinum and BST films.

5.5 Temperature Versus Capacitance Measurements

One of the major disadvantages of the RF magnetron sputtering process is that the deposited films are not stoichiometric. Since BST films phase transition behavior depends on its chemical composition it is important to check whether the deposited films are in paraelectric phase by conducting temperature versus capacitance measurements. This is done by measuring the variation of capacitance (or relative dielectric permittivity) of the BST based varactors with temperature. If the films are in paraelectric phase the variations in capacitance with temperature would be negligible. Large variations in capacitance values with temperature would be a cause for concern as it would affect the overall performance of the varactors with temperature variations.

For this measurement SiO_2 varactor was used. The temperature was varied from room temperature (25ºC) to 120ºC (Curie temperature of barium titanate) and capacitance values were extracted by using the equivalent circuit model at 100MHz. The variation of capacitance with temperature for the measured varactor is shown in Figure 5.14.

As seen from the figure, the capacitance steadily decreases with increase in temperature and the percentage variation in capacitance from room temperature to 120ºC is around

9%-10%. This indicates that the deposited BST film underwent diffuse phase transition i.e. the phase transitions occurs over a wide range of temperature[68]. This is one of the thickness effects observed in ferroelectric thin films. Therefore there is a possibility of the film exhibiting ferroelectric behavior at room temperature. It is also possible that the strontium present induces some quantum ferroelectric behavior in the film [65]. The XRD pattern of the deposited BST films (discussed in Chapter Three) showed BST peaks occurring at positions slightly shifted away from their ideal positions. These shifts in peak positions indicate a possible increase in Barium content in the deposited film which could be responsible for the increased variations in temperature due to increase in the Curie temperature of the deposited film. Since ferroelectric behavior is undesirable for the intended application area of these varactors further study must be conducted to understand the phase transition behavior of the deposited BST thin films.

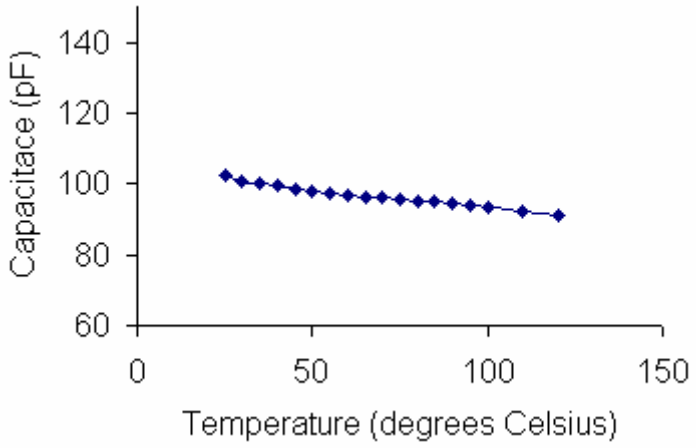

Figure 5.14: Variation of capacitance with temperature for the measured varactor at 100MHz.

CHAPTER 6:

SURFACE ACOUSTIC WAVE DEVICES

6.1 Surface Acoustic Wave (SAW) Devices

Surface acoustic waves (SAW) is the general name for the elastic waves that propagate at the surface of solids, whose displacement amplitudes undergo exponential decay beneath this surface, similar to the ones that propagate on the water surface. Typically almost all of the energy is localized within a depth of two wavelengths. There are many different types of SAW waves. The SAW industry uses mainly Rayleigh waves, which are named after Lord Rayleigh.

The most common processing techniques involve either the time delay of the signal, which depends on the geometry of the device and the acoustic velocity, or the amplitude of the signal which can be varied or "weighted" by controlling the efficiency of the piezoelectric transduction [104, 105].

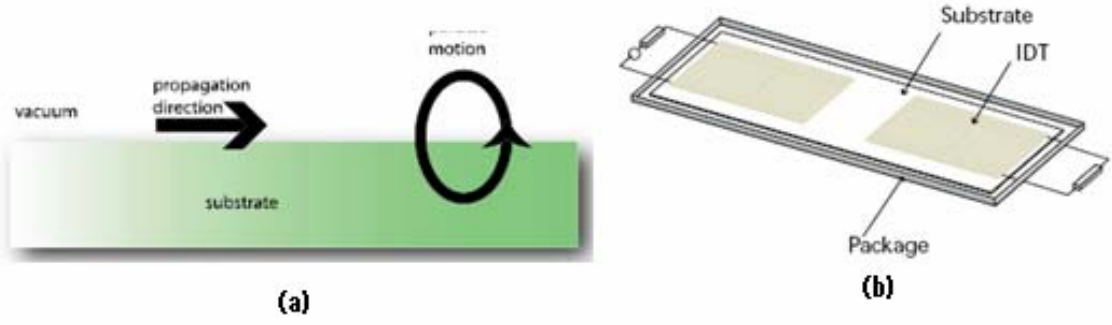

Figure 6.1: Schematic of (a) surface acoustic wave propagation on a piezoelectric surface, (b) a basic SAW device [105].

6.2 Types of SAW Devices

The device in Fig 6.1(a) is a schematic representation of the propagation of a SAW wave on a piezoelectric surface and 6.1 (b) is a schematic of a basic SAW delay line. As the wave takes some time to travel between the Interdigital Transducers (IDT's) - typically 1 μs for 3 mm of path length. This is very compact compared with EM waves which, in free space, need 300 m of path for 1 μs delay. The device can also be used as a bandpass filter, because the transducers operate most effectively when the SAW wavelength equals the transducer pitch - at other frequencies the waves generated by individual gaps are not in phase, so the wave amplitude falls off as the frequency is changed.

Another basic device is the SAW resonator. This uses arrays of metal strips, with pitch $\lambda/2$, as reflectors of the waves. These arrays can give strong SAW reflections, and two arrays can be used to form a SAW resonator with high Q, up to 10^5. Such resonators are often used for high-stability oscillators. The above mentioned devices are just some basic types. Many unique variations are possible for SAW devices, and their applications range from piezoelectric strain gauges to pulse compression radar, to cellular handsets.

The most common group is bandpass filters, which are in very widespread use in radio systems (including mobile phone handsets and base stations) and in domestic TV. There are many types with differing advantages, such as low shape factor, low insertion loss, small size, or high-frequency operation. The wide variety of types is possible because almost arbitrary shapes can be defined on the surface with very high precision, using lithography techniques similar to those for semiconductor processing. A typical SAW Bandpass characteristic is shown if Fig 6.2 [104, 105].

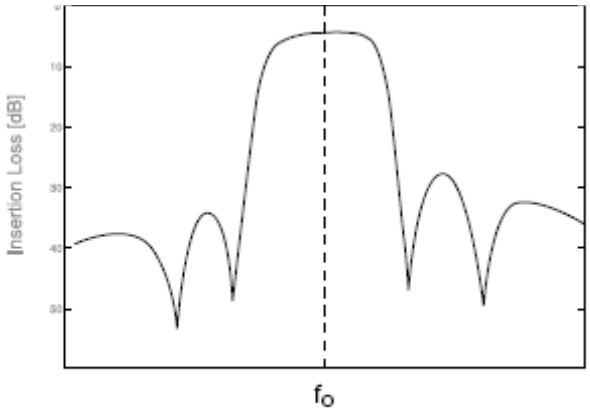

Figure 6.2: Typical SAW bandpass filter response [105].

As mentioned earlier, application of CVD diamond to layered surface acoustic wave (SAW) device is attractive because it has the highest acoustic velocity among all materials, and thus, when combined with a piezoelectric layer, it will be of good use to high frequency SAW devices providing great advantages in the manufacturing of the devices. In this research work a layered SAW device with $Ba_{0.8}Sr_{0.2}TiO_3$ as the piezoelectric layer is investigated. SAW bandpass filters and resonators are going to be the devices used for characterizing the SAW properties of this layered SAW device. Figure 6.3 shows the general schematic of a SAW bandpass filter and resonator. Table 6.1 [28, 106, 107] shows the acoustic velocities of materials used for SAW applications. From the table it can be seen that a layered SAW device using CVD diamond would provide much better performance than a SAW device based on conventional piezoelectric substrates like quartz and lithium niobate.

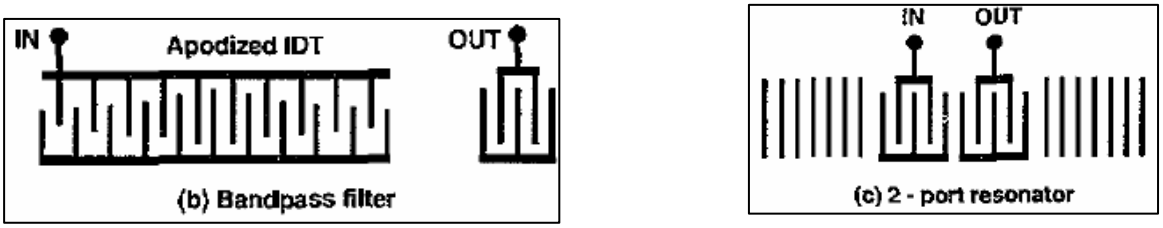

Figure 6.3: General schematic of a SAW bandpass filter and resonator [108].

Table 6.1: Comparison of acoustic velocities of prospective materials [28, 106, 107].

Material	Acoustic Velocity (m/s)
YZ Lithium Niobate	3488
ST-X Quartz	3158
Single Crystal Silicon	8024
CVD Diamond	16200

6.3 Basic SAW Device Performance Parameters

- Phase velocity ($v_{ø}$)

It is governed by the wavelength of the SAW device (periodicity of IDT'S) and the centre frequency of the SAW filter [104].

$V\text{ø} = f_0 * \lambda$

- Electromechanical Coupling Coefficient (K^2)

It determines the strength of coupling between electrical and mechanical fields. It is the efficiency with which EM waves are converted to acoustic waves by the IDT's and vice versa [109].

$K^2 = (\pi/4N).(R_0/X_0)$ where,

R_0 is the radiation resistance of the transducer

X_0 is the static reactance of the transducer

N is the number of interdigital finger pairs

6.4 Challenges in Development of Layered SAW Devices

BST has a very high coupling coefficient value (0.70) and thus it improves the efficiency with which conversion is done by the IDC's. The high relative permittivity of BST ensures good impedance matching to external components. Since the permittivity of BST can be tuned with applied bias, it offers an extra tool of being able to tune the sensitivity of the SAW device for sensor applications [110].

One big disadvantage of using BST is the low Curie temperature which restricts its use to underwater applications. The other disadvantage is the thickness effects in BST which results in its properties changing with thickness. This makes device characterization and performance optimization complex and difficult. A completely defect free surface is required for efficient SAW propagation. To actually obtain a defect free BST layer on CVD diamond is a big challenge due to the defects and structural non-uniformities in the CVD diamond layer.

Finally, a layered SAW device performance is thickness-dependent. The analysis of thicknesses of the CVD diamond layer and the piezoelectric layer is required to restrict the propagating SAW waves to the diamond layer and to obviate the necessity to incorporate IDT with finger widths in the sub-micron range. H. Nakahati et al have provided a detailed theoretical analysis of characteristics of layered diamond based SAW structures [28, 111]. In general, CVD diamond thicknesses in the range of 20 μm and piezoelectric layer thicknesses in the range of 1.2 μm is required for layered SAW devices with IDT finger widths > 4 μm [109]. Getting such thick layers and maintaining a homogeneous surface presents challenges in optimization of the deposition process and structural characterization of the CVD diamond and BST layers.

6.5 Design of SAW Bandpass Filters and Resonators

The IDT usually comprises two sets of interpenetrating metallic electrodes fabricated photolithographically on the surface of a piezoelectric layer. A typical SAW device contains two such IDTS, one as input transducer, the other as output transducer to convert the SAW back to the electrical domain. During this process some useful signal processing function is performed, e.g. delay or filtering. In the simplest case each period of the IDT comprises two fingers and two gaps each of width *p/4* where '*p'* is the period of the IDT.

Considering the input IDT, the wavelets generated by the individual periods add constructively when the SAW wavelength equals the period *p* (Refer to Figure 6.4). The electric fields between adjacent IDT electrodes of opposite polarity penetrate the substrate to a depth of order *p/4*, and so have a strong overlap with the strain field of the surface acoustic wave i.e. the IDT provides efficient piezoelectric coupling to SAW. Similarly, the output IDT is coupled to the incoming SAW, as can be shown by dual reciprocity [108].

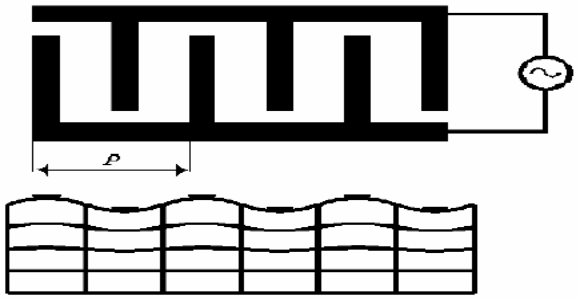

Figure 6.4: Relation between SAW wavelength and period of interdigital transducer.

There are infinite possibilities for variation of IDT device geometry [112]. The device geometry has a strong influence on the type of wave that is getting propagated. In this research work the basic aim of the designing process is to characterize the performance of CVD diamond based SAW devices with a ferroelectric layer on top. Therefore wide

variations have been done on the device geometry to make a comprehensive study of device properties versus SAW performance. The variations in device geometry that have been incorporated in the mask are summarized in Table 6.2. The mask design has been done using CoventorWare and variations in device geometry have been summarized below. The device layouts are shown in Figure 6.5.

Table 6.2: Variation of various parameters in SAW device geometry.

Parameter varied	Variation
Thickness of piezoelectric layer	600 nm-1200 nm
Thickness of NCD	8 μm-20 μm
Number of IDT finger pairs	10-50
Periodicity	8 μm-24 μm
Distance between IDT's	20 λ-200 λ

The IDC geometries can be varied in the future based on the conclusions drawn from the devices in this mask for optimal device performance. The Interdigital Capacitors (IDC's) were used for Curie temperature measurements.

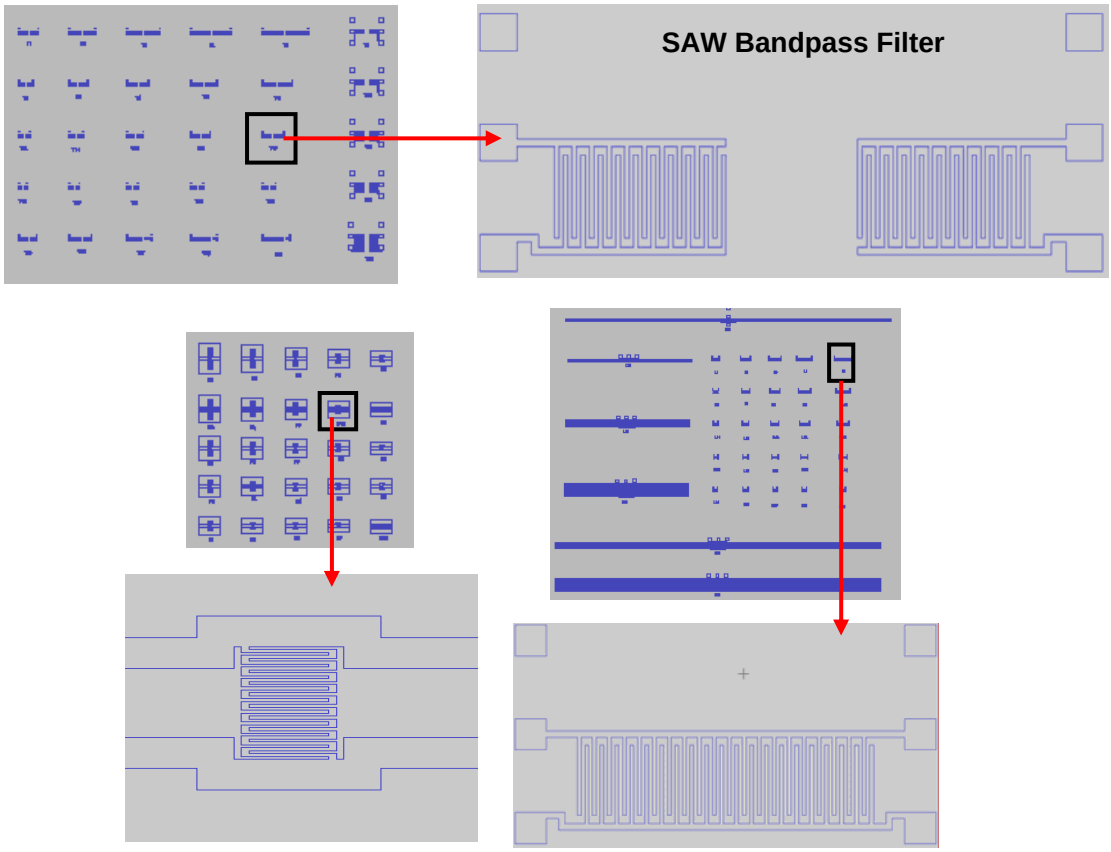

Figure 6.5: Layouts of different device structures.

6.6 Deposition of BST on Chemical Vapor Deposited Diamond

BST films were deposited on CVD diamond using the RF magnetron sputtering method. The deposition parameters were varied in order to get the highest possible thickness of the BST layer. It was found that at 200 W RF power there was a good growth rate (23-25 nm/hour) beyond which the RF power started affecting the target. Therefore depositions were done with the standard deposition conditions described in Table3.2 (page number 51) and the time of deposition was increased up to 12 hours to get the desired BST thickness. Since there were two deposited layers on Si substrate (CVD diamond and sputtered BST), θ-2θ XRD studies were inconclusive due to their relatively low thickness compared to the Si substrate. As mentioned before, the surface roughness of the BST layer was dependent on the diamond layer. Cross-sectional SEM studies showed that there were no adhesion issues with BST on CVD diamond (Figure 6.6).

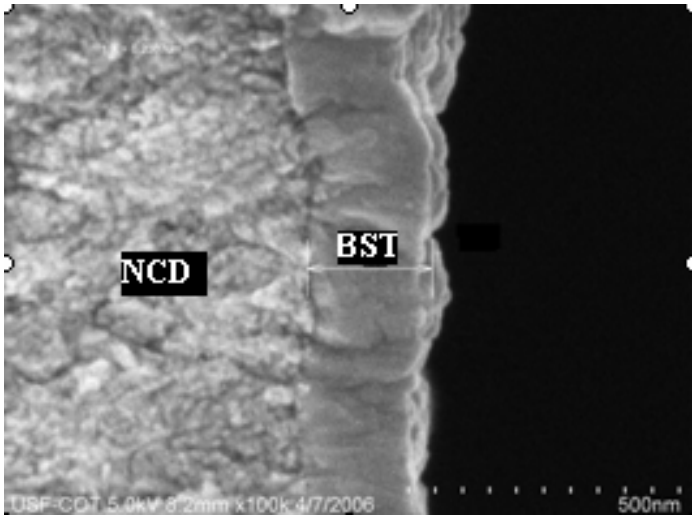

Figure 6.6: Cross-sectional SEM image of BST on CVD diamond.

6.7 Fabrication of Interdigital Structures

The traditional metal lift-off method did not work for the fabrication of the IDT's as particles of the top electrode layer was getting stuck in between the finger gaps in the 2 micron and 3 micron interdigital structures. Therefore a modified fabrication process was followed in which the metal layer was deposited and patterned first and then the gold metal was etched off instead of being lifted-off.

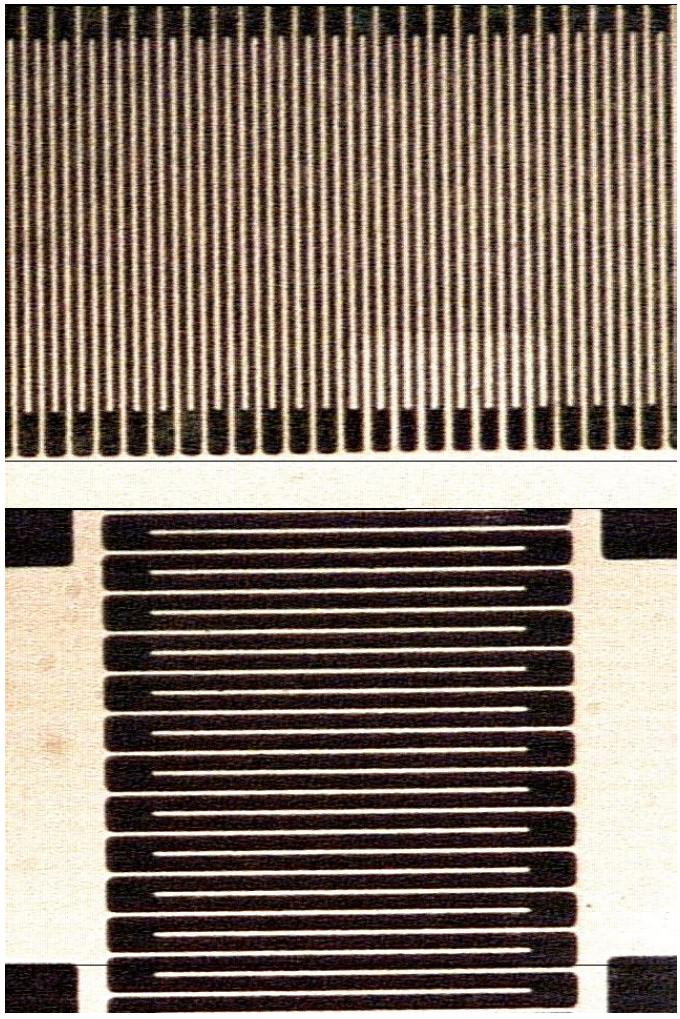

Figure 6.7: Photographs of fabricated IDT's with 2 μm and 3 μm finger widths.

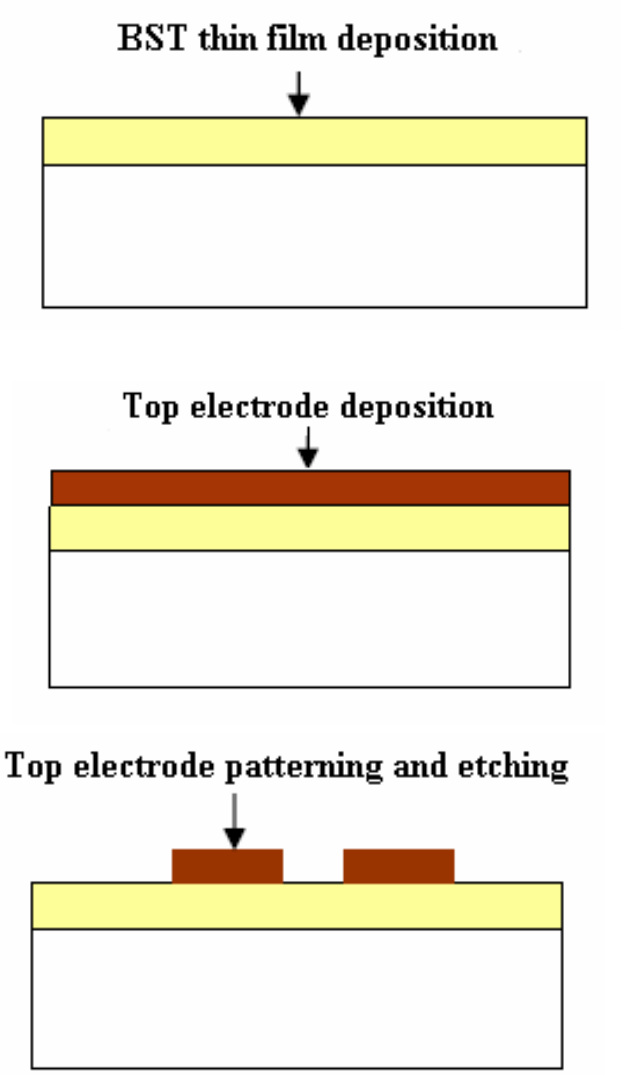

Figure 6.8: Fabrication process flow of Interdigital structures.

The fabrication process was started by first sputtering Titanium (Ti) and Gold (Au) (where Ti is the adhesion layer) on the deposited BST layer. The thicknesses of Ti and Au were 40Å and 3000Å respectively. The wafer was then patterned using conventional lithography techniques using a positive resist in order to pattern the interdigital structures. Finally the Au and the Ti layers were etched off using the respective wet etchants. The etch times for Au and Ti were 3min30sec and 10 seconds respectively.

The resulting 2 micron and 3 micron interdigital structures were very well-defined. Photographs of fabricated devices are also provided in Figure 6.7. The process flow of the IDT fabrication is summarized in Figure 6.8. Further study needs to be done by conducting the SEM analysis of the fabricated interdigital structures to conform the absence of top electrode particles in between the electrode fingers.

6.8 Curie Temperature Measurements on $Ba_{0.8}Sr_{0.2}TiO_3$

Curie temperature measurements were done in order to determine the temperature range up to which the deposited BST films exhibit ferroelectricity. The measurements were done on Interdigital Capacitor (IDC) structures. 25 IDC structures with geometry variations identical to the SAW bandpass structures were designed specifically for these measurements. The schematic of the IDC structures are shown in Figure 6.9.

BST films were deposited on 4-inch high resistivity silicon samples using the RF magnetron sputtering process using standardized deposition conditions except for the deposition time which was increased from the usual 4 hours to 8hrs, 10hrs and 12 hrs respectively. It was observed that with increase in the deposition time, the uniformity of the BST film got affected. For a 4hour deposition the variation in thickness from centers to edge of the sample was around 30nm. For an 8 hour deposition the variation in thickness from centre to edge was around 135nm. The variation in thicknesses from the edges to the centre of the sample is provided in Table 6.3. In general, an area of about one inch in the sample showed uniform thickness with increase in deposition time and the devices of interest were fabricated in this area. A schematic of the appearance of the 4-inch sample after a 12 hour BST deposition is shown in Figure 6.10.

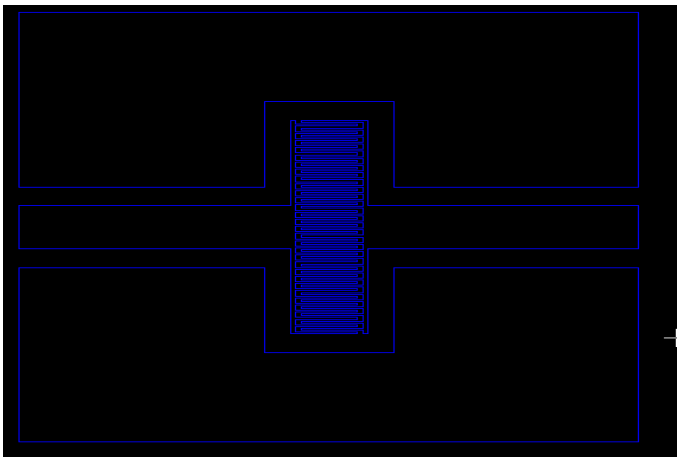

Figure 6.9: Schematic of Interdigital capacitor structure used for Curie temperature measurements.

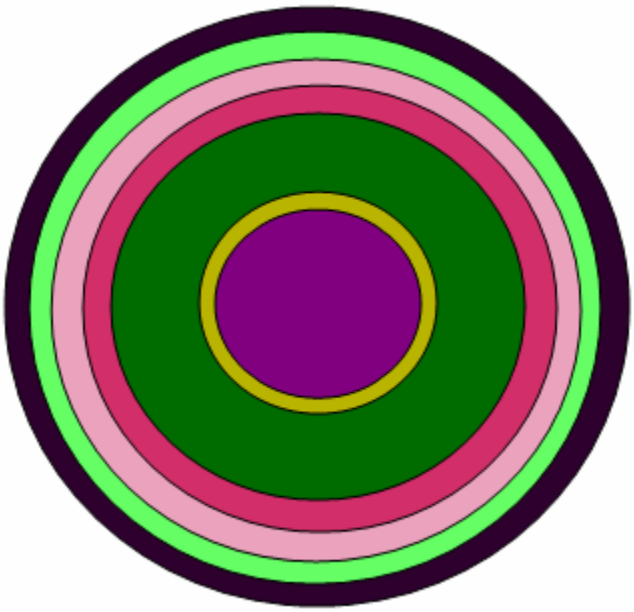

Figure 6.10: Schematic of appearance of the 4-inch sample after deposition of BST for 12 hours with different colors representing different thicknesses.

Table 6.3: Variation in thickness of BST layer with different deposition times.

Deposition time	Range of thicknesses obtained (nm) (from edge to center of the sample)
4 hours	100-130
8 hours	205-336
10 hours	235-428
12 hours	295-513

Cascade Microtech system with Cryogenic temperature control was used for the measurements. The capacitance was calculated with change in temperature to determine the Curie temperature [113]. Two-port S-parameter measurements were performed on the fabricated IDC structures. The calibration was done from 1GHz to 7 GHz using the TRL calibration technique. The temperature was varied from -15ºC to 120ºC (Curie temperature of Barium Titanate). The capacitance was calculated at different temperatures was used to plot the capacitance vs. temperature graph for determining the transition region. The equivalent circuit diagram used for extracting the capacitance values is shown in Figure 6.11.

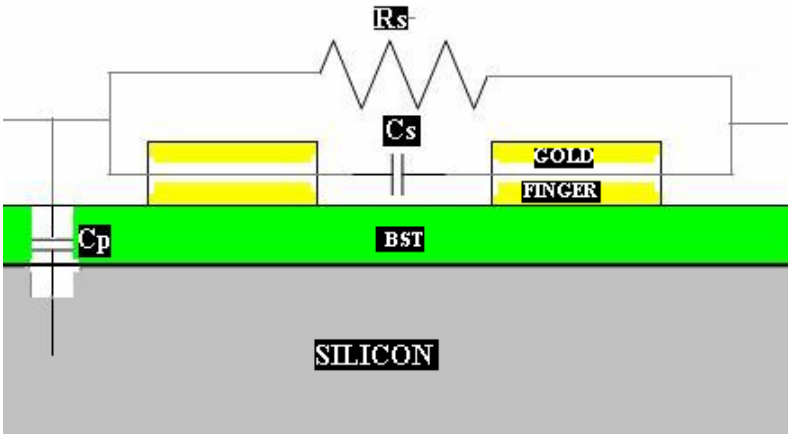

Figure 6.11: Equivalent circuit diagram used for characterizing IDC performance.

The temperature vs. capacitance measurements obtained for the interdigital capacitor is shown in Figure 6.12. The measured IDC had 30 finger pairs with a finger width of 5 μm. The aperture of the IDC was 137.5 microns and IDT length was 125 microns. The device was fabricated on the area of the wafer where the deposited BST thickness was 400 nm (deposition time-10 hours). The measurements (refer to Figure 6.12) indicated that the Curie temperature of the deposited BST films occurred around the 20 degrees Celsius mark which is well below the theoretical Curie temperature of $Ba_{0.8}Sr_{0.2}TiO_3$ (77ºC) [64]. This could be due to the shift in apparent Curie temperature due to thickness effects. Further research work is necessary to determine the various factors that affect the Curie temperature of BST in order to obtain films that are ferroelectric (and hence piezoelectric) for underwater SAW applications.

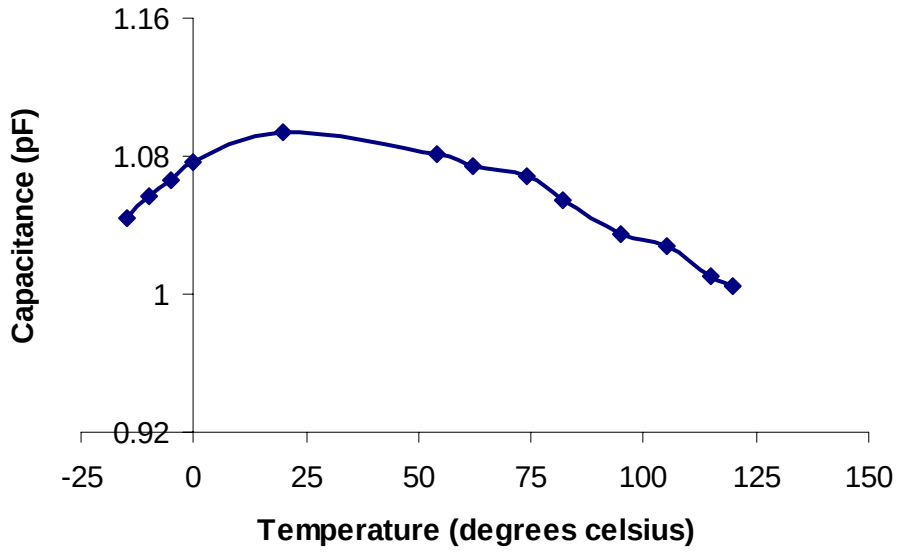

Figure 6.12: Temperature versus capacitance measurements obtained from the measured Interdigital capacitor.

CHAPTER 7:

CONCLUSIONS AND FUTURE WORK

7.1 BST Deposition and Structural Characterization

- RF magnetron sputtering method was employed to deposit $Ba_{0.5}Sr_{0.5}TiO_3$ thin films on $Pt/Ti/SiO_2/Si$ bottom electrode stack and the deposition conditions were optimized to obviate the shorting problems in BST varactors and improve the dielectric strength of the deposited BST films.
- XRD and AFM were used for structural characterization of the deposited BST films. The change in deposition conditions did not cause any discernible change in the structural properties of the deposited films.
- BST films were then deposited on Pt/NCD/Si electrode stack and the structural characteristics of the deposited films were then compared with those deposited on $Pt/Ti/SiO_2/Si$ wafer. NCD was deposited on Si wafer by the MPECVD technique. The BST films deposited on Pt/NCD/Si displayed more defects and much higher surface roughness due to the comparatively high roughness of the diamond layer.
- The stoichiometry of the deposited BST thin films need to studied by using Rutherford Back Scattering (RBS) technique to further optimize the deposition process by compensating for the stoichiometric mismatch between the BST target used for deposition and the sputtered BST film.

- The deposition process can be modified by reducing the RF power in order to get larger grains and reduce the density of grain boundaries especially for nanoscale devices to reduce the statistical variations in properties of devices fabricated on the BST layer.
- Substrates like MgO and $LaAlO_3$ can be used to obtain mono-crystalline, epitaxial and textured BST thin films which will translate into better performance of fabricated devices.
- Bismuth Zinc Niobate (BZN) is currently being researched as an alternative material for varactor applications at high frequencies [38]. Future research work can be conducted on this material and comparisons can be done between BZN varactors and BST varactors.

7.2 Interdiffusion

- Cross-sectional SEM analysis was done on Pt/Ti/SiO_2/Si and Pt/NCD/Si electrode stacks after BST deposition. It was observed that the Pt/Ti/SiO_2/Si displayed heavy interdiffusion between the Ti and Pt layers.
- The Pt/NCD/Si stack, in comparison displayed stable interfaces between the different layers. This was further conformed by conducting X-ray mapping of the stack. The XRM results also indicated the existence of stable interfaces.
- The interface analysis of the bottom electrode stack can be further done by using RBS and Transmission Electron Microscopy.

7.3 BST Varactor Fabrication and Measurements

- BST MIM structures were fabricated using conventional optical lithography and etching techniques. The devices fabricated had large active areas varying from 2500 μm^2 to 30000 μm^2. Hence the devices had high capacitance values and lower quality factor values at higher frequencies.

- The performance of the fabricated varactors was characterized from 100 MHz to 1 GHz and measurements revealed that the BST varactors fabricated on Pt/NCD/Si displayed better quality factors and good symmetry in CV characteristics due to the existence of stable interfaces.
- The varactors fabricated on $Pt/Ti/SiO_2/Si$ were demonstrated much better reliability and higher breakdown fields. The high surface roughness and inconsistency of BST films on Pt/NCD/Si contributed to the relatively poor reliability and breakdown fields.
- Based on the results obtained a relation was derived linking the interface quality to the tunability and breakdown voltage in varactors. It was found that thetunability and breakdown of varactors have a direct relation with the BST film thickness. The lower the BST film thickness, the faster the tunability. However bad interfaces restrict the thickness of BST that can be deposited and thereby affect the tuning speed of the varactor.
- It was concluded that with a good interface and a stable bottom electrode it is possible to tailor the performance of the varactors to suit various applications. Thus with the realization of a robust NCD based MIM structure, a good all-round varactor performance can be obtained.
- Further work needs to be done to improve the structural properties of the BST films deposited on MPECVD diamond based electrode stack.
- BST nano-scale varactors that operate efficiently at frequencies >1 GHz have been fabricated by employing the Focused Ion Beam (FIB) milling technique [114]. A schematic of the fabricated series-gap capacitor structure is shown in Figure 7.1.

- Future work in this area will be on investigating the non-linear properties of nano-scale active regions of BST thin films for developing Non-Linear Transmission Lines (NLTL's) for pulse shaping and pulse modulation, frequency multipliers and non-linear antennas.

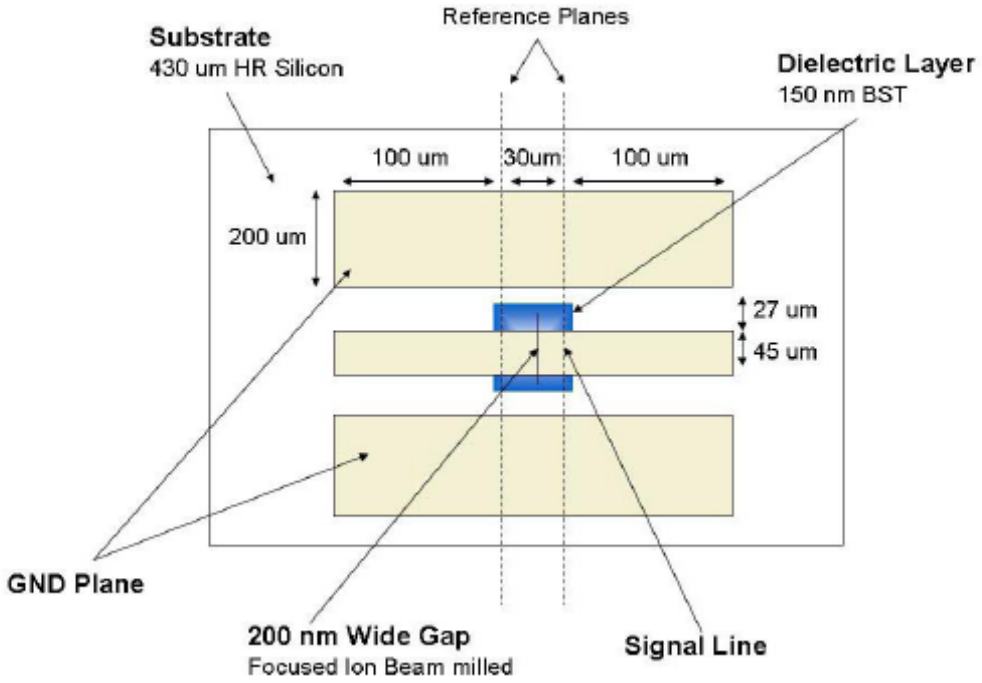

Figure 7.1: FIB milled BST series gap capacitor configuration.

7.4 Diamond Based Layered SAW Devices

- Initial structural characterization of $Ba_{0.8}Sr_{0.2}TiO_3$ films deposited on MPECVD diamond was done. Thicker BST films were deposited by increasing the deposition time.
- SAW bandpass filters and resonators were designed with variations in the device geometry in order to characterize the effect of device geometry on the performance of layered diamond-BST based SAW devices.
- Temperature versus capacitance measurements were conducted on the deposited BST films to ascertain the temperature at which phase transition occurs for the deposited BST films. The phase transition was found to occur at a much lower temperature compared to the theoretical phase transition temperatures.
- Grazing incidence XRD needs to be done to properly characterize the structural properties of the deposited BST films. It is also critical to maintain stoichiometry in the deposited BST films to improve the phase transition behavior. RBS analysis and further optimization of the deposition process is necessary to study stoichiometry of the BST films and obtain thicker films.
- Piezoelectric characterization of the $Ba_{0.8}Sr_{0.2}TiO_3$ films needs to be done to predict the performance of the diamond-BST based SAW devices. A measurement setup and technique for accurately calculating the phase velocity and electromechanical coupling coefficient needs to be developed.

REFERENCES

[1] B. Noren, "Thin Film Barium Strontium Titanate (BST) for a new class of tunable RF components," in *Microwave Journal*, vol. 47, 2004, pp. 210-220.

[2] S.J. Fiedziusko, I.C.Hunter, T.Itoh, Y.Kobayashi, T.Nishikawa, S.N.Stitzer, K.Wakino, "Dielectric Materials, Devices and Circuits," *IEEE Transactions Microwave Theory and Techniques*, vol. 50, pp. 706-720, 2002.

[3] W.J.Germula, R.D.Hall, "Ferroelectrics at microwave frequencies," in *Microwave Journal*, June 1960.

[4] A.K.Tagantsev, V.O.Sherman,K.F.Astafev,J.Venkatesh,N.Setter, "Ferroelectric Materials for Microwave Tunable Applications," *Journal of Electroceramics*, vol. 11, pp. 5-66, 2003.

[5] C.Basceri, S.K.Streiffer, A.I.Kingon, R.Waser "The dielectric response as a function of temperature and film thickness of fiber-textured (Ba,Sr)TiO_3 thin films grown by chemical vapor deposition," *Journal of Applied Physics*, vol. 82, pp. 2497-2504, 1997.

[6] K.R.Carroll, J.M.Pond, D.B.Chrisey, J.S.Horwitz, R.E.Leuchtner, K.S. Grabowski, "Microwave measurements of the dielectric constant of $Sr_{0.5}Ba_{0.5}TiO_3$ ferroelectric thin films," *Applied Physics Letters*, vol. 62, pp. 1845-1847, 1993.

[7] A.T.Findigoklu, Q.X.Jia, D.W.Reagor, X.D.Wu, "Electrical characteristics of Coplanar Waveguide Devices Incorporating Nonlinear Dielectric Thin Films of $SrTiO_3$ and $Sr_{0.5}Ba_{0.5}TiO_3$ " *Microwave and Optical Technology Letters*, vol. 9, pp. 306, 1995.

[8] B.Acikel, T.R.Taylor, P.J.Hansen, J.S.Speck, R.A.York, "A New High Performance Phase Shifter using (Ba,Sr)TiO_3 Thin Films," *IEEE Microwave and Wireless Components Letters*, vol. 12, pp. 237-239, 2002.

[9] M.Jain, S.B.Majumder, R.S.Katiyar, A.S.Bhalla, D.C. Agarwal, F.W. Van Keuls, F.A.Miranda, R.R.Romanovsky, C.H.Mueller, "Improved dielectric performance of heterostructured $Ba_{0.5}Sr_{0.5}TiO_3$ thin film composites for microwave dielectric devices," *Material Research Society Symposium Proceedings*, vol. 748, pp. 483-488, 2003.

[10] Q. J. Bae Ho Park, "Enhanced dielectric properties of (Ba, Sr)TiO_3 thin films applicable to tunable microwave devices," *Japanese Journal of Applied Physics*, vol. 41, pp. 7222-7225, 2002.

[11] F. T. A. J.P.Maria, A.I. Kingon, A.Tombak, A.Mortazawi, G.Stauf, C.Ragaglia, J.Roeder, M.Brand, "(Ba,Sr)TiO_3 capacitors for tunable high frequency applications," *Material Research Society Meeting*, 2000.

[12] J.Belotti, E.K.Akdogan, A.Safari, Wontae Chang, J.Pond, "Frequency agile BST thin films for RF/Microwave applications," *Ferroelectrics*, vol. 271, pp. 131-136, 2002.

[13] D.Ueda, "Implementation of GaAs monolithic microwave integrated circuits with on-chip BST capacitors," *Journal of Electroceramics*, vol. 3, pp. 105-113, 1999.

[14] B.Acikel, L.Yu, A.S.Nagra, T.R.Taylor, P.J.Hansen, J.S.Speck, R.A.York, "Phase shifters using (Ba,Sr)TiO/sub3/ thin films on sapphire and glass substrates," *presented at IEEE MTT-S International Microwave Symposium* 2001.

[15] B. Acikel, "High Performance Barium Strontium Titanate Varactor Technology for Low Cost Circuit Applications," University of California, Santa Barbara, 2002.

[16] D.M.Bubb, J.S.Horwitz,S.B.Qadri,S.W.Kirchoefer,C.Hubert,J.Levy, "(Ba,Sr)TiO_3 thin films grown by pulsed laser deposition with low dielectric loss at microwave frequencies," *Applied Physics A*, vol. 79, pp. 99-101, 2004.

[17] H.Boubekeur, T.Mikolajick,W.Palmer,J.Hopfner,L.Frey,H.Ryssel, "Platinum contamination issues in ferroelectric memories," *Journal of Applied Physics*, vol. 92, pp. 3257-3265, 2002.

[18] R.York, A.Nagra, E.Erker, T. Taylor, P. Periaswamy, J.Speck, S. Streiffer, O. Auciello, "Microwave integrated circuits using thin-film BST," *IEEE International Symposium on Applied Ferroelectrics*, vol. 1, pp. 195-200, 2000.

[19] K. Wang, K. Yao, S.J. Chua, "Titanium diffusion and residual stress of platinum thin films on Ti/SiO_2/Si substrate," *Journal of Applied Physics*, vol. 98, pp. 013538-1 - 013538-5, 2005.

[20] H-J. Nam, D-K. Choi, W-J. Lee, "Formation of hillocks in Pt Ti electrodes and their effects on short phenomena of PZT films deposited by reactive sputtering," *Thin Solid Films*, vol. 371, pp. 264-271, 2000.

[21] H.N. Al-Shareef, D. Dimos, B.A. Tuttle, M.V. Raymond "Metallization schemes for dielectric thin film capacitors," *Journal of Materials Research*, vol. 12, pp. 347-354, 1997.

[22] Y. Matsui, M. Hiratani, Y. Kumagai, H. Miura, Y. Fujisaki, "Thermal Stability of Pt Bottom Electrodes for Ferroelectric Capacitors " *Japanese Journal of Applied Physics*, vol. 37, pp. L465-L467, 1998.

[23] A.Tombak, J.P.Maria, F.Ayguavives, Z.Jin, G.T.Stauf, A.I.Kingon, A.Mortazawi, "Tunable Barium Strontium Titanate thin film capacitors for RF and microwave applications, " *IEEE Microwave and Wireless Components Letters*, vol. 12, pp. 3-5, 2002.

[24] J.Chee, R.Karru,T.S.Fisher,D.Peroulis, "DC-65GHz characterization of nanocrystalline diamond leaky film for reliable RF MEMS switches," *IEEE EGAAS 2005*, pp. 581-584, 2005.

[25] C. Beuille, E.Dutarde,H.Schneider,MC.Castex,E.Lefeuvre,J.Achard,F.Silva, "Characterization of metal-diamond-silicon associations for active power electronics applications," *IEEE 33rd Annual Power Electronics Specialists Conference*, vol. 4, pp. 1764-1768, 2002.

[26] M.Awada, J.W.Strojek,G.M.Swain, "Electrodeposition of Metal Adlayers on Boron-Doped Thin Film Electrodes," *Journal of Electrochemical Society*, vol. 142, pp. L42-L45, 1995.

[27] M. Ohring, *The Material Science of Thin Films*. San Diego: Academic Press, 1992.

[28] H. Nakahata, K. Higaki, S. Fujii, A, Hachigo, H. Kitabayashi, K. Tanabe, Y. Seki, S. Shikata, "Surface Acoustic Wave Devices on Diamond," *IEEE Ultrasonics Symposium*, vol. 1, pp. 361-370, 1995.

[29] B. Jaffe, W. R. Cook, Jr. and H. Jaffe, *Piezoelectric ceramics*. New York: Academic Press, 1971.

[30] J.A.Gallego-Juarez, "Piezoelectric ceramics and ultrasonic transducers," *Journal of Physics E*, vol. 22, pp. 804-816, 1989.

[31] T.L.Jordan, Z.Ounaies, "Piezoelectric Ceramics Characterization," NASA Langley Research Center 2001.

[32] APC International Ltd, "Piezoelectric Ceramics: Principles and Applications ", vol. 90-1015.

[33] "http://www.rci.rutgers.edu/~ecerg/projects/ferroelectric.html."

[34] F.S. Gallaso, *Perovskite and high T_c superconductors*: Gordon and Breach, 1990.

[35] R.Blinc, B.Zeks, *Soft Modes in Ferroelectrics and Antiferroelectrics*. Amsterdam: Elsevier, 1974.

[36] M.E.Lines, A.M.Glass, *Principles and Applications of Ferroelectrics and Related Materials*. Oxford: Clarendon, 1977.

[37] Ulrich Bottger, "Dielectric Properties of Polar Oxides," in *Polar Oxides: Properties, Characterization, and Imaging*: Wiley, 2005.

[38] S.Stemmer, "Tutorial Overview of Tunable Dielectrics," presented at IEEE MTT-S International Microwave Symposium, Long Beach, CA, 2005.

[39] F. Jona, G. Shirane, *Ferroelectric Crystals*. New York: Dover, 1993.

[40] U. Bottger, "Dielectric Properties of Polar Oxides," in *Polar Oxides: Properties, Characterization, and Imaging*: Wiley, 2005.

[41] E.Y.Tsymbal, "Dielectric Properties of Insulators," in *Introduction to Solid State Physics*. University of Nebraska, Lincoln.

[42] M.Uludogan, T.Cagin, "First Principles Approach to $BaTiO_3$," *Turkish Journal of Physics*, vol. 30, pp. 277-285, 2006.

[43] S. Trolier-McKinstry, "Ferroelectrics Tutorial," presented at Material Research Society, Boston, MA, 2007.

[44] O.Hudak, "Landau theory of 180^o domain walls in $BaTiO_3$ type ferroelectric particles : microcomposite materials," *Condensed Matter*, vol. 2, pp. 1-10, 2005.

[45] R.P.Feynman, "Mainly Electromagnetism and Matter," in *The Feynman Lectures on Physics*. Redwood City, CA: Addison-Wesley, 1989.

[46] A.C.Goodge, "Lens Focused Microwave Reflectometry Concepts for Ceramic Coating Characterization." Charlottesville: University of Virginia, 1997.

[47] R. Botsco, R. McMaster, *Electromagnetic Testing*, vol. 4: The American Society for Nondestructive Testing, 1986.

[48] Emerson, & Cuming Microwave Products, "Dielectric Material Chart."

[49] A.J. Moulson, J.M. Herbert, *Electroceramics:Materials, Properties, Applications*. New York: Chapman and Hall, 1997.

[50] D. Damajanovic, "Ferroelectric, dielectric, and piezoelectric properties of ferroelectric thin films and ceramics," *Rep. Prog. Phys.*, vol. 61, pp. 1267-1324, 1998.

[51] R. Waser, *Nanoelectronics and Information Technology*. Germany: Wiley-VCH, 2003.

[52] M.D. Losego, "The Chemical Solution Deposition of Lead Zirconium Titanate (PZT) Thin Films directly on copper surfaces," vol. M.S.: North Carolina State University, 2005.

[53] D. Ghosh, "Tunable Microwave Devices using BST and Base Metal Electrodes," vol. Ph.D.: North Carolina State University, 2005.

[54] K. Morito, Y. Iwazaki, T. Suzuki, M. Fujimoto, "Electric field induced piezoelectric resonance in the micrometer to millimeter waveband in a thin film $SrTiO_3$ capacitor," *Journal of Applied Physics*, vol. 94, pp. 5199-5205, 2003.

[55] J. Im, O. Auciello, P.K. Baumann, K. Streiffer, D.Y. Kaufman, A.R. Krauss, "Composition-control of magnetron-sputter-deposited $(Ba_xSr_{1-x})Ti_{1+y}O_{3+z}$ thin films for voltage tunable devices," *Applied Physics Letters*, vol. 76, pp. 625-627, 2000.

[56] B. York, "Tunable Dielectrics for RF circuits," in *Multifunctional Adaptive Microwave Circuits and Systems* 2006.

[57] R. Yimnirun, V. Sundar, R.E. Newnham, "Electrostriction," in *Electrical Engineering Handbook* 3ed: CRC, 2006.

[58] W.P. Mason, "Electrostrictive Effect in Barium Titanate Ceramics," *Physical Review*, vol. 74, pp. 1134-1147, 1948.

[59] T.M.Shaw, S.Trolier-McKinstry, P.C. McIntyre, "The Properties of Ferroelectric Films At Small Dimensions," *Annual Review in Material Science*, vol. 30, pp. 263-298, 2000.

[60] C.Basceri, S.E. Lash, C.B. Parker, S.K. Streiffer, A.I. Kingon, M.Grossmann, S.Hoffmann, L. Schumacher, R. Waser, S. Bilodeau, R. Carl, P.C. van Buskirk, S.R. Summerfelt, "An Important Failure Mechanism in MOCVD $(Ba,Sr)TiO_3$ Thin Films: Resistance Degradation," presented at Materials Research Society, 1998.

[61] K. Numata, Y. Fukuda, K. Aoki, A. Nishimura "Analysis of the Resistance Degradation of $SrTiO_3$ and $Ba_xSr_{(1-x)}TiO_3$ Thin Films," *Japanese Journal of Applied Physics*, vol. 34, pp. 5245-5249, 1995.

[62] R. Waser, T.Baiatu, K-H. Hardtl, "DC Electrical Degradation of Perovskite-Type Titanates," *Journal of American Ceramic Society*, vol. 73, pp. 1645-1653, 1990.

[63] M. Grossmann, S. Hoffmann, S. Gusowski, R. Waser, S.K. Streiffer, C. Basceri, C.B. Parker, S.E. Lash, A.I. Kingon., "Resistance Degradation Behavior of $Ba_{0.7}Sr_{0.3}TiO_3$ Thin Films Compared to Mechanisms Found in Titanate Ceramics and Single Crystals " *Integrated Ferroelectrics*, vol. 22, pp. 83-94, 1998.

[64] P.M. Suherman, T.J. Jackson, M.J. Lancaster, "Broadband Microwave Characterization of Ferroelectric Thin Films," University of Birmingham 2004.

[65] K.A. Muller, H. Burkard, "$SrTiO_3$ an intrinsic quantum paraelectric below 4K," *Physical Review B*, vol. 19, pp. 3593, 1979.

[66] G.A. Smolenskii, V.A. Isupov, *Zhurnal Tekhnicheskoi Fiziki*, vol. 24, pp. 1375, 1954.

[67] T. M. Shaw, Z. Suo, M. Huang, E. Liniger, R. B. Laibowitz, J. D. Baniecki,, "The effect of stress on the dielectric properties of barium strontium titanate thin films," *Applied Physics Letters*, vol. 75, pp. 2129-2131, 1999.

[68] C. B. Parker, J.-P. Maria, A. I. Kingon, "Temperature and thickness dependent permittivity of (Ba, Sr)TiO_3 thin films," *Applied Physics Letters*, vol. 81, pp. 340-342, 2002.

[69] A. Lookman, R.M. Bowman, J.M. Gregg, J.F. Scott, M. Dawber, A. Reudiger, "Understanding thickness effects of thin film capacitors," *Integrated Ferroelectrics*, vol. 61, pp. 51-58, 2004.

[70] Z.-G. Ban, S. P. Alpay, "Phase diagrams and dielectric response of epitaxial barium strontium titanate films: A theoretical analysis," *Journal of Applied Physics*, vol. 91, 2002.

[71] S.U. Adikary, H.L.W. Chan, "Ferroelectric and dielectric properties of sol–gel derived $Ba_xSr_{1-x}TiO_3$ thin films," *Thin Solid Films*, vol. 424, pp. 70-74, 2002.

[72] R. Kretschmer, K. Binder, "Surface effects on phase transitions in ferroelectrics and dipolar magnets " *Physical Review B*, vol. 30, pp. 1065-1076.

[73] C. Zhou, D. M. Newns "Intrinsic dead layer effect and the performance of ferroelectric thin film capacitors," *Journal of Applied Physics*, vol. 82, pp. 3081-3088, 1997.

[74] B.A.Tuttle, T.J. Garino, J.A. Voight, T.J. Headley, D. Dimos, M.O. Eatough, in *Science and Technology of Electroceramic Thin Films* R. W. O. Auciello, Ed., 1995, pp. 117-132.

[75] A.L. Kholkin, M.L. Calzada, P. Ramos, J. Mendiola, N. Setter, "Piezoelectric properties of Ca modified $PbTiO_3$ thin films," *Applied Physics Letters*, vol. 69, pp. 3602-3604, 1996.

[76] S. Trolier-McKinstry, J. F. Shepard, Jr., J. L. Lacey, T. Su, G. Zavala, J. Fendler "Piezoelectricity in Ferroelectric Thin Films. Domains and Stress Issues," *Ferroelectrics*, vol. 206, pp. 381-392, 1998.

[77] M. Schumacher, G.W. Deitz, R. Waser., "Dielectric relaxation of perovskite - type oxide thin films," *Integrated Ferroelectrics*, vol. 10, pp. 231-245, 1995.

[78] S.K. Streiffer, C. Basceri, A.I. Kingon, S. Lipa, S. Bilodeau, R. Carl, and P.C. Van Buskirk, "Dielectric Behavior of CVD (Ba,Sr)TiO3 Thin Films on Pt/Si," presented at Materials Research Society Symposium, 1996.

[79] J.D. Baniecki, R.B. Laibowitz, T.M. Shaw, P.R. Duncombe, D.A. Neumayer, D.E. Kotecki, H. Shen, Q.Y. Ma, "Dielectric relaxation of Ba[sub 0.7]Sr[sub 0.3]TiO[sub 3] thin films from 1 mHz to 20 GHz.," *Applied Physics Letters*, vol. 72, pp. 498-500.

[80] Y. Fukuda, K. Numata, K. Aoki and A. Nishimura "Origin of Dielectric Relaxation Observed for $Ba_{0.5}Sr_{0.5}TiO_3$ Thin-Film Capacitor " *Japanese Journal of Applied Physics*, vol. 35, pp. 5178-5180, 1996.

[81] Y. Fukuda, Y. Haneda, H. Sakaguchi, K. Numata, K. Aoki, A. Nishimura, "Dielectric Properties of (Ba, Sr)TiO_3 Thin Films and their Correlation with Oxygen Vacancy Density " *Japanese Journal of Applied Physics*, vol. 36, pp. L1514-L1516.

[82] M. Schumacher, R. Waser., "Curie - Von Schweidler behaviour observed in ferroelectric thin films and comparison to superparaelectric thin film materials," *Integrated Ferroelectrics*, vol. 22, pp. 109-121.

[83] J.D. Baniecki, R.B. Laibowitz, T.M. Shaw, P.R. Duncombe, D.A. Neumayer, "Low temperature hydrogen induced degradation of (Ba, Sr) TiO3 thin film capacitors," *Integrated Ferroelectrics*, vol. 22, 2000.

[84] T. Delage, C. Champeaux, A. Catherinot, J. F. Seaux, V. Madrangeas, D. Cros "High-K BST films deposited on MgO by PLD with and without buffer-layer ", vol. 453, pp. 279-284, 2004.

[85] P. Padmini, T.R. Taylor, M.R. Lefervre, A.S. Nagra, R.A. York, J.S. Speck, "Realization of high tunability barium strontium titanate thin films by RF magnetron sputtering," *Applied Physics Letters*, vol. 75, pp. 3186-3188, 1999.

[86] W. Chang, J.S. Horwitz, A.C. Carter, J.M. Pond, S.W. Kirchoefer, C.M. Gilmore, D.B. Chrisey, "The effect of annealing on the microwave properties of $Ba_{0.5}Sr_{0.5}TiO_3$ thin films," *Applied Physics Letters*, vol. 74, 1999.

[87] S. Stemmer, S.K. Streiffer, N.D. Browning, C. Basceri, A.I. Kingon, "Grain Boundaries in Barium Strontium Titanate Thin Films: Structure, Chemistry and Influence on Electronic Properties," *Interface Science*, vol. 8, pp. 209-221, 2000.

[88] S. Stemmer, S. K. Streiffer, N.D. Browning, A.I. Kingon "Accommodation of nonstoichiometry in (100) fiber-textured $(Ba_xSr_{1-x})Ti_{1+y}O_{3+z}$ thin films grown by chemical vapor deposition," *Applied Physics Letters*, vol. 74, pp. 2432-2434, 1999.

[89] X. G. W. Pompe, Z. Suo, J. S. Speck "Elastic energy release due to domain formation in the strained epitaxy of ferroelectric and ferroelastic films," *Journal of Applied Physics*, vol. 74, pp. 6012-6019, 1993.

[90] R. York, A. Nagra, E. Erker, T. Taylor, P. Periaswamy, J. Speck, S. Streiffer, O. Auciello, "Microwave integrated circuits using thin-film BST," presented at International Society of Applied Ferroelectrics (ISAF), Hawaii, 2000.

[91] S.G. Manavalan, "Structural and Electrical Properties of Barium Strontium Titanate Thin Films for Tunable Microwave Applications," University of South Florida, Tampa, 2004.

[92] L.F. Chen, C.K. Ong, C.P. Neo, V.V. Varadhan, V.K. Varadhan, *Microwave Electronics : Measurement and Material Characterization*: Wiley, 2004.

[93] C.P. Wen, "Coplanar Waveguide: A Surface Strip Transmission Line Suitable for Nonreciprocal Gyromagnetic Device Applications," *IEEE Transactions Microwave Theory and Techniques*, vol. 17, pp. 1087-1090, 1969.

[94] J. Böhlmark, "Fundamentals of High Power Impulse Magnetron Sputtering," Linkoping University, Sweden, 2005.

[95] A. Kumar, S. G. Manavalan, V. Gurumurthy, S. Jeedigunta, T. Weller "Dielectric and structural properties of pulsed laser deposited and sputtered barium strontium titanate thin films," *Material Science & Engineering B*, vol. 139, pp. 177-185, 2007.

[96] J.F. Scott, "Overview," Cambridge University.

[97] M.Liehr, H.Dallaporta,J.E.Lewis, "Defect formation in SiO_2/Si(100) by metal diffusion and reaction," *Applied Physics Letters*, vol. 53, pp. 589-591, 1988.

[98] G.S.Narayana, N.K.Misra, "X-ray studies on growth, thermal vibrations and internal stress in thin condensed films of indium," *Indian Journal of Physics Part A*, vol. 64A, pp. 151-155, 1990.

[99] T.R. Taylor, "Stoichiometry and thermal mismatch effects on sputtered barium strontium titanate thin films." Santa Barbara: University of California, 2003.

[100] D. E. Newbury, "X-ray Mapping Is 50 Years Young; the Best Is Yet to Come; the Future Is Now!," *Microscopy&Microanalysis Journal*, vol. 12(supp 2), pp. 818-819, 2006.

[101] J.J. O'Dwyer, *The Theory of Electrical Conduction and Breakdown in Solid Dielectrics*. London: Oxford University Press, 1973.

[102] J.F. Scott, "Device Physics of Ferroelectric Thin Film Memories," *Japanese Journal of Applied Physics*, vol. 38, pp. 2272-2274, 1999.

[103] S.P. Alpay, "Dielectrics and Ferroelectrics," in *Introduction to Structure, Properties, and Processing of Materials II*, 2007.

[104] C.K. Campbell, *Surface Acoustic Wave Devices for Mobile and Wireless Communications* San Diego: Academic Press.

[105] COM DEV SAW Products, "What is a SAW filter?."

[106] Boston Piezo-Optics Inc., "Surface Acoustic Wave Substrates."

[107] J. Wang, J.E. Butler, T. Feygelson, C. Nguyen, "1.51-GHz nanocrystalline diamond micromechanical disk resonator with material-mismatched isolating support," presented at IEEE International Conference on MEMS, 2004.

[108] M. F. Lewis, "Rayleigh waves- a progress report," *European Journal of Physics*, vol. 16, pp. 1-7, 1995.

[109] M. Benetti, D. Cannata, F.D. Pietrantonio, E. Verona, "Growth of AlN Piezoelectric Film on Diamond for High-Frequency Surface Acoustic Wave Devices," *IEEE transactions on Ultrasonics, Ferroelectrics and Frequency Control*, vol. 52, pp. 1806-1811, 2004.

[110] A. Amin, B.M. Kulwicki, "Electromechanical Properties of BST for Acoustic Imaging Arrays," *IEEE Intenational Symposium on Applied Ferroelectrics*, vol. 1, pp. 491-493, 2000.

[111] H Nakahata, A. Hachigo, K. Higaki, S. Fujii, Member, S-I. Shikata, N. Fujimori, "Theoretical Study on SAW Characteristics of Layered Structures Including a Diamond Layer," *IEEE transactions on Ultrasonics, Ferroelectrics and Frequency Control*, vol. 42, pp. 362-375, 1995.

[112] C.K. Campbell, "Applications of Surface Acoustic and Shallow Bulk Acoustic Wave Devices," *IEEE Proceedings*, vol. 77, pp. 1453-1484, 1989.

[113] J. Nath, W.M. Fathelbab, P.G. Lam, D. Ghosh, S. Aygun, K.G. Gard, J.-P. Maria, A.I. Kingon, M.B. Steer, "Discrete Barium Strontium Titanate (BST) Thin-Film Interdigital Varactors on Alumina: Design, Fabrication, Characterization, and Applications," presented at IEEE Microwave Theories and Techniques International Microwave Symposium Digest, 2006.

[114] S. Baylis, "Tunable Patch Antenna Using Semiconductor and Nano-Scale Barium Strontium Titanate Varactors," MS Thesis, University of South Florida, 2007.